ON ASSIMILATING SEA SURFACE TEMPERATURE DATA INTO AN OCEAN GENERAL CIRCULATION MODEL

By

Anthony T. Weaver

B. Sc. (Physics) University of Victoria

A THESIS SUBMITTED IN PARTIAL FULFILLMENT OF

THE REQUIREMENTS FOR THE DEGREE OF

MASTER OF SCIENCE

in

THE FACULTY OF GRADUATE STUDIES

DEPARTMENT OF OCEANOGRAPHY

INSTITUTE OF APPLIED MATHEMATICS

We accept this thesis as conforming

to the required standard

THE UNIVERSITY OF BRITISH COLUMBIA

September 1990

In presenting this thesis in partial fulfilment of the requirements for an advanced degree at the University of British Columbia, I agree that the Library shall make it freely available for reference and study. I further agree that permission for extensive copying of this thesis for scholarly purposes may be granted by the head of my department or by his or her representatives. It is understood that copying or publication of this thesis for financial gain shall not be allowed without my written permission.

Department of Oceanography & Institute of Applied Mathematics.

The University of British Columbia
Vancouver, Canada

Date Sept 15, 1990

DE-6 (2/88)

Abstract

The feasibility of sea surface temperature (SST) data improving the performance of an ocean general circulation model (OGCM) is investigated through a series of idealized numerical experiments. The GFDL Bryan-Cox-Semtner primitive equation model is set-up as an eddy resolving, unforced, flat bottomed channel of uniform depth. 'Observed' SST data taken from a reference ocean established in a control run are continuously assimilated into an 'imperfect' model using a simple 'nudging' scheme based on a surface relaxation condition of the form $Q = C(\mathrm{SST} - T_1)$ where Q is the heat flux and T_1 is the temperature at the top level of the model. The rate of assimilation is controlled by adjusting the constant inverse relaxation time parameter C.

Numerical experiments indicate that the greatest improvement in the model fields is achieved in the extreme case of infinite assimilation (i.e., $C = \infty$) in which the 'observed' SST is directly inserted into the model. This improvement is quantified by monitoring the reduction in the root mean square (RMS) errors relative to the simulated reference ocean. Assimilation with longer relaxation time-scales (i.e., smaller C's) proves quite ineffective in reducing the RMS errors. The improvement in the direct insertion numerical experiment stems from the model's ability to transfer assimilated SST into subsurface information through strong advective processes. The assimilation of cool surface data induces convective overturning which transfers the 'cool' information downward rapidly but adversely affects the vertical thermal structure by an unrealistic deepening of the mixed layer. By contrast, warm surface data do not penetrate downward readily. Thus, the systematically biased downward flux of coolness gradually produces unrealistically cool subsurface waters.

Table of Contents

List of Tables

List of Figures

Acknowledgement

I would like to thank Dr. W.W. Hsieh for his support and encouragement as my research supervisor and Dr. D.G. Steyn for his useful comments and criticisms which lead to improvements in the final form of the thesis. Many helpful and informative discussions with Dr. A.J. Weaver regarding the numerical model are very much appreciated.

Financial support from the Natural Sciences and Engineering Research Council of Canada in the form of a postgraduate scholarship is also gratefully acknowledged.

Chapter 1

Introduction

The ability to make accurate climate predictions over time scales of months to years has become the most pressing issue confronting oceanographers and meteorologists alike. Central to the climate prediction problem is the need to develop coupled general circulation models (CGCM) comprising an atmospheric GCM component and an ocean GCM component. Yet, providing a perfect numerical model would be only half the answer for we must also contend with the problem of determining complete and accurate initial data fields. Since the atmosphere has a relatively short term memory (it is essentially unpredictable over time scales longer than a few weeks), accurate initialization of its component is not critical for climate prediction. The ocean on the other hand, evolves on much slower time scales and since it forms most of the bottom boundary for the atmosphere, it is generally believed that best climate forecasts are to be achieved through an accurate initialization of the ocean component.

The task of constructing a set of complete and accurate initial data for a numerical prediction model from available observational data is the object of what is commonly referred to as initialization and four-dimensional data assimilation. This crucial aspect of forecast modelling has been a topic of particular interest to meteorologists over the last two decades with regard to numerical weather prediction. Classically, the procedure for initiating a weather forecast at time $t = t_0$, say, consists of blending or assimilating new observational data with currently modelled meteorolgical fields computed on the basis of earlier observations collected at times $t \leq t_0$. Thus by updating the model

in a preforecast integration (e.g., 24 hrs or 48 hrs preceding the initial forecast time) with the best synoptic and asynoptic data, we can estimate the initial data much more accurately than by simply interpolating over the model domain using only sparse data available at or close to $t = t_0$.

The 'data-set' generated by the assimilation procedure just described, although complete, is still not in optimal form for the purpose of initializing a forecast. Initial imbalances between the mass and velocity fields will result in the generation of high frequency inertia-gravity waves or 'shocks' in the ensuing quasi-geostrophic adjustment. These imbalances exist because both observational fields and numerical models contain errors. Since freely propagating inertia-gravity wave 'noise' can severely contaminate the model solution, it is important to minimize their effects. In addition, these spurious waves can prolong the adjustment time of the model after each update and hence severely restrict the frequency of data assimilation. To overcome this problem and more importantly to avoid updating a model which is in a perpetual state of imbalance, an effective damping mechanism is required. The filtering process through which a relatively 'noise-free' start is sought, is usually referred to as initialization.

Several assimilation and initialization techniques have been developed by the meteorological community and many of them are used operationally with numerical weather prediction models (see Ghil et al. (1978), Bengtsson (1975) and Bengtsson et al. (1981) for comprehensive reviews). In contrast, however, procedures for assimilating real ocean data into numerical ocean models is far from well-developed. The main reason for the slow development of data assimilation in oceanography stemmed from the fact that up until the last decade there had been minimal oceanographic data available. However, with the development of new observational techniques, especially those associated with satellite remote-sensing (altimetry, scatterometry, radiometry), numerous oceanographic data are being provided and ocean data assimilation has become feasible.

The differences between the atmosphere and ocean, both dynamically and in the availability of observational data, make the ocean data assimilation problem quite distinct from its atmospheric counterpart. For example, in the ocean the Rossby radius of deformation is on the order of 10-100 km as compared to 1000 km in the atmosphere. Consequently, a higher spatial resolution of observations is required for the ocean. On the other hand, the time scales in the ocean are characteristically much longer thus enabling for the most part, a much larger time window for observational measurements. Even with the advent of satellite data and the increasing number of XBT, CTD and other hydrographic measurements, oceanographers are, and will in the future, be faced with far fewer observations than meteorologists. In addition, the distribution of these data is extremely uneven in both time and space; satellite measurements provide global coverage with varying spatial and temporal resolution of ocean surface features, while hydrographic measurements provide a sparse network of subsurface information. Ghil (1989) provides a more detailed discussion of the data availability differences between the ocean and the atmosphere.

For these reasons, oceanographic research in data assimilation is not a simple extension of meteorological data assimilation. Nevertheless, the experience gained by meteorologists in the field does provide a firm foundation from which oceanographers can develop their own assimilation procedures. To date, research has been primarily aimed at understanding some of the more fundamental aspects of ocean data assimilation through idealized experimentation using a variety of numerical models and data assimilation techniques.

In practice, certain ocean measurements are much easier to make than others, so it is important to determine the relative information content of each data-type. For example, the effects of updating different models with (simulated) velocity and temperature (i.e., density) data was investigated by Moore et al. (1987) in their study of tropical

ocean data assimilation. They adopted an 'identical twin' strategy in which the model itself is used to simulate a reference ocean in a control integration (the reference ocean, thus, providing the 'observations' used in the assimilation experiments). They showed that the usefulness of either data-type is sensitive to the partitioning of energy in the region of interest – velocity (temperature) measurements being better when the energy in the region is primarily kinetic (potential). These results suggest that an accurate parameterization of mixing and diffusion processes is important, otherwise, the model's energy partition which is likely to be very sensitive to these processes, may be altered, thus affecting the relative usefulness of these data-types. Through similar idealized experimentation, Malanotte-Rizzoli et al. (1989) compared the assimilation of baroclinic information, such as density data, with barotropic information, that is, measurements of the depth-integrated mass transport obtained from tomography for example. Their study revealed that knowledge of the baroclinic component of the flow was much more effective in improving the model, particularly when the horizontal resolution of the measurements was decreased.

In reality, the available measurements of subsurface oceanographic variables constitute very localized data-sets. Malanotte-Rizzoli and Holland (1986,1988) assimilated vertical (density) data sections into a quasi-geostrophic (QG) model with the primary focus of their study aimed at understanding if information provided by a single hydrographic section is sufficient to drive an 'imperfect' model toward reality. Their results indicated that these data-sets might be useful in correcting the climatological trend of the model but are relatively ineffective over shorter time scales (in the order of 100 days) comparable with the time scale of the model's predictability loss. The assimilation of simulated XBT temperature data along sparse tracks was considered by Moore et al. (1987). Employing a simple linear-reduced gravity model of the tropical Pacific Ocean, Moore (1989) and Moore and Anderson (1989) later extended their

study to include real XBT data collected as a part of the TOGA ship-of-opportunity program.

The most extensive research in ocean data assimilation to date has been concerned with assimilating satellite altimeter (sea-surface height) data through techniques of blending, projection and extrapolation. (Hurlburt, 1986; De Mey and Robinson, 1987; Webb and Moore, (1986); Berry and Marshall, 1989; Holland and Malanotte-Rizzoli, 1989; White et al., 1990(a) and (b); Miller, 1989; Verron, 1990). These studies have been conducted using simple models (e.g., QG) with only a few vertical modes but have yet to be extended to more complex multi-level primitive equation (PE) models.

Together with the numerical model and observational data, an analysis or assimilation technique is required to complete any data assimilation system. Several of the techniques developed in meteorology for numerical weather prediction have been borrowed by oceanographers in their assimilation studies.

Statistical interpolation methods such as optimal interpolation (Gandin, 1963) and successive corrections (Cressman, 1959) are the analysis techniques most widely used by meteorologists to combine irregularly distributed observations with corresponding model predicted fields. More recently, they have been applied in several ocean assimilation studies (Moore et al., 1987; Moore and Anderson, 1989, Leetma and Ji, 1990; Derber and Rosati, 1989). The basic procedure involves modifying the first guess (i.e., the model's estimate of a particular variable) at any given time by adding to it the weighted mean value of observations surrounding the grid point;

$$\hat{q}_i = q_i^m + \frac{\sum_k p_k (q_k^o - q_k^m)}{\sum_k p_k}, \tag{1.1}$$

where $\hat{q}_i$ is the analyzed value of the variable q at the grid point i, q_i^m is the first guess or model estimate of q at the point i, q_k^o is the observation of q at station k, and p_k are

the weights.

In the method of optimal interpolation the weights are determined by minimizing the mean square error between the true state and the analyzed state. This procedure leads to a linear system of equations for p_k involving model and observational error covariance matrices, so that past knowledge of the statistical behaviour of the fields is required for this method. In the successive correction method, however, the weights are based on empirical correlation functions which determine the distances over which the observations are allowed to influence the analysis. Equation (1.1) is then applied in an iterative manner, with the analyzed value replacing the model value after each successive 'scan'. A more complicated and computationally more expensive version of (1.1) is the Kalman filter in which the error covariance matrices are computed by the model at each time step rather than modelled as in optimal interpolation. Applications of the Kalman filter to ocean models has been considered by Miller (1986,1989) and Bennett and Budgell (1987,1989).

Recently, an alternative assimilation scheme to the sequential assimilation approach of the statistical methods (i.e., blending new observations with currently modelled fields) has been developed based on the principles of variational calculus and optimal control (Lewis and Derber, 1985; LeDimet and Talagrand, 1986; Derber, 1985). In this powerful method, a cost function measuring the distance, or misfit, between model and data, is minimized subject to the constraint that the model variables must satisfy the equations of motion. This procedure leads to the so-called adjoint equations which can be solved together with the original set of equations using an optimization routine (e.g., the conjugate gradient method) to determine an initial state which represents a 'best-fit' between the model dynamics and available observational data. An advantage of this method is its ability to incorporate naturally large asynoptic data-sets (e.g., from satellites) and to extract the maximum amount of information from them. However,

the computational requirements involved in its implementation have meant that its application so far has been restricted to very simple ocean models (Long and Thacker, 1989(a) and (b); Sheinbaum and Anderson, 1990(a) and (b); Tziperman and Thacker, 1989), thus, suggesting that the method might be impractical for much more complex models (certain GCMs for example).

The initialization process (i.e., filtering of unbalanced data to eliminate 'shocks') which is crucial for atmospheric models, has been examined in the oceanographic context by Malanotte-Rizzoli et al. (1989). They showed in a mid-latitude study using an unforced, rigid lid, PE model that gravity wave 'shocks' are significant only if the initial fields are severely unbalanced. This is because (1) the rigid lid approximation filters out fast-propagating surface gravity waves which would constitute a major part of the noise, and (2) the dissipative mechanisms in the model are effective in damping out the less energetic internal/inertial gravity wave 'shocks'. Sophisticated initialization schemes used in meteorology such as normal mode initialization (Leith, 1980; Daley, 1981) are, therefore, deemed unnecessary for many ocean modelling studies, particularly those using rigid lid models.

The situation is quite different in the tropics, however, where unbalanced data can excite 'shocks' in the form of large amplitude equatorially trapped waves which, if left unchecked, can severely degrade the model solution (Moore, 1989). The technique of normal mode initialization was shown by Moore (1990) to be successful in suppressing these gravity 'shocks'.

In this study, the feasibility of sea surface temperature (SST) data improving the performance of a primitive equation ocean general circulation model is investigated through a series of idealized numerical experiments using simulated observations. The assimilation of SST, however, is not a new venture. Robinson et al. (1988) used SST

observations with their method of 'feature-model initialization' for a Gulf Stream forecast system. This technique involves first locating major features (e.g., well-defined rings and meanders) from remotely sensed SST and then analytically inferring a subsurface structure to them based on previous subsurface measurements. Following this initialization[1] procedure, the features are allowed to adjust dynamically and evolve as the model is integrated forward in time. Later Robinson et al. (1989) extended their study to include a limited number of XBT observations as well.

Leetma and Ji (1989) and Derber and Rosati (1989) have also considered the assimilation of SST. In both cases though, additional information in the subsurface thermal field were provided through XBT measurements which in turn, were assimilated along with the SST data using a statistical interpolation method. There are many regions however, for which hydrographic and/or XBT measurements do not exist and hence no knowledge of the vertical density structure are available. Measurements of ocean surface features, on the other hand, are becoming increasingly more available on a periodic basis from satellite remote sensing systems. Indeed, the wide-availability of SST and its advantage over other remotely sensed data in terms of higher space-time resolution make it a particularly attractive data-set.

The purpose of this study, therefore, is to determine if the assimilation of SST observations alone provides enough information to guide an ocean model toward reality. No prior knowledge of the subsurface thermal fields are assumed, nor is any attempt made to extrapolate the information provided by SST to infer a subsurface structure. The SST is simply assimilated by Newtonian relaxation ('nudging') or inserted directly into the upper-level temperature field of the model, from which point the dynamics of the model are then responsible for spreading the information to the subsurface.

[1]initialization in this context refers to establishing an initial condition, not to the elimination of 'shocks' as in the atmospheric sense.

The thesis is organized as follows. In Chapter 2, a full description of the primitive equation model is given. The basic methodology and particular assimilation technique employed are outlined in Chapter 3. In Chapter 4, a description of the flow field characteristics of the baseline experiment is given, followed by a comparison of the results from the different assimilation experiments. The summary and conclusions are presented in Chapter 5.

Chapter 2

Description of the Model

The numerical model used in this study is the widely used GFDL Bryan-Cox-Semtner OGCM as described in Cox (1984). Since the original development of this 3-dimensional, primitive equation (PE) model by Bryan and Cox (1967), the model has evolved through a series of additions and improvements so that to date it is the most comprehensive and complete model available for studying features of the large-scale ocean circulation.

In §2.1 and §2.2 the governing set of equations and boundary conditions of the model are described respectively. In §2.3 an outline is given of the approach used to solve the equations, followed by a brief description in §2.4 of the discretization method implemented. A more comprehensive discussion of the model physics and numerical method is given in Bryan (1969).

For the idealized data assimilation experiments in this study, the GFDL model has been set-up as an east-west periodic flat bottomed channel of uniform depth. A fine horizontal grid spacing has been employed so that the model is capable of resolving mesoscale features. The details of the experimental model set-up and initial conditions are given in §2.4 and §2.5 respectively.

2.1 Governing Equations

The governing set of equations consists of the momentum (Navier-Stokes) equations for a fluid in a rotating frame of reference, mass, temperature and salinity conservation equations, and an equation of state. The equations are formulated in spherical

coordinates (λ, ϕ, z) , where λ is longtitude, ϕ is latitude, and z is height (measured positive upwards) relative to the earth's mean radius, a. Corresponding to the zonal, meridional and vertical directions are the velocity components (u, v, w) respectively.

Two fundamental approximations are made which are valid for large-scale ocean circulation studies. First, the hydrostatic approximation is assumed whereby the acceleration, Coriolis and viscous terms are neglected in the vertical momentum equation. The second basic assumption adopted is that the ocean may be treated as a Boussinesq fluid so that the effect of density variations is retained only in the buoyancy term and density is thus taken to be constant in all other terms. A consequence of introducing the Boussinesq approximation is to filter out all sound waves. Finally, the effects of Reynolds stresses and fluxes are parameterized by introducing the eddy viscosity and diffusion closure scheme. In this approach, turbulent quantities arising from the nonlinearity in the horizontal momentum and tracer conservation equations are represented by coefficients (horizontal/vertical) of eddy viscosity and diffusion respectively.

The horizontal momentum equations are given by,

$$\begin{aligned} u_t + \mathcal{L}(u) - (f + ua^{-1}\tan\phi)v &= -(a\cos\phi)^{-1}(p/\rho_0)_\lambda + F^\lambda, \\ v_t + \mathcal{L}(v) + (f + ua^{-1}\tan\phi)u &= -a^{-1}(p/\rho_0)_\phi + F^\phi, \end{aligned} \tag{2.1}$$

where

$$f = 2\Omega\sin\phi, \tag{2.2}$$

is the Coriolis parameter, Ω is the angular velocity of rotation of the earth, p is the pressure, and ρ_0 is the mean density (taken to be unity in cgs units). $\mathcal{L}$ denotes the advection operator defined by,

$$\mathcal{L}(\mu) = (a\cos\phi)^{-1}((u\mu)_\lambda + (u\mu\cos\phi)_\phi) + (w\mu)_z, \tag{2.3}$$

where subscripts correspond to differentiation with respect to that variable. F^λ and

F^ϕ are the eddy stresses given by,

$$F^\lambda = A_{MV}u_{zz} + A_{MH}[\nabla^2 u + (1-\tan^2\phi)a^{-2}u - (2\tan\phi)(a^2\cos\phi)^{-1}v_\lambda],$$
$$F^\phi = A_{MV}v_{zz} + A_{MH}[\nabla^2 v + (1-\tan^2\phi)a^{-2}v + (2\tan\phi)(a^2\cos\phi)^{-1}u_\lambda], \tag{2.4}$$

where A_{MH} and A_{MV} are the coefficients of horizontal and vertical eddy viscosity respectively and ∇^2 is the horizontal Laplacian defined as,

$$\nabla^2\mu = (a^2\cos\phi)^{-1}(\mu_{\lambda\lambda}(\cos\phi)^{-1} + (\mu_\phi\cos\phi)_\phi). \tag{2.5}$$

The vertical momentum equation under the assumptions already mentioned reduces to the hydrostatic relation,

$$p_z = -\rho g, \tag{2.6}$$

where ρ is the density and g is the acceleration due to gravity. Using the definition (2.3) we can write the mass conservation equation (or continuity equation) as simply,

$$\mathcal{L}(1) = 0. \tag{2.7}$$

The conservation equations for heat and salt are,

$$T_t + \mathcal{L}(T) = A_{HV}T_{zz} + A_{HH}\nabla^2 T + \delta_c(T), \tag{2.8}$$

$$S_t + \mathcal{L}(S) = A_{HV}S_{zz} + A_{HH}\nabla^2 S + \delta_c(S), \tag{2.9}$$

where T is temperature and S is salinity. Lateral and vertical eddy diffusivities are given by A_{HH} and A_{HV} respectively. The term δ_c represents a convective adjustment to keep the density field convectively stable. In the model this adjustment is handled through an implicit convection scheme, so that when a gravitational instability is encountered, the water column is mixed vertically until stability is restored.

The equation of state for sea water is a complicated function of pressure, temperature and salinity and can be written symbolically in the form,

$$\rho = \rho(T, S, p). \tag{2.10}$$

In practice, (2.10) is usually expressed by an approximate formula based on empirical observations. In this model, a polynomial fit to the Knudsen formula (Bryan and Cox, 1972) is used.

2.2 Boundary Conditions

The north and south walls of the channel are insulating, no-slip and impermeable,

$$T_\phi = S_\phi = 0, \tag{2.11}$$

$$u = v = 0. \tag{2.12}$$

At the east and west ends of the channel a cyclic condition is imposed on all variables. The bottom boundary at $z = -H$ is insulating, free-slip and impermeable,

$$T_z = S_z = 0, \tag{2.13}$$

$$u_z = v_z = w = 0. \tag{2.14}$$

At the upper boundary, $z = 0$,

$$T_z = S_z = 0, \tag{2.15}$$

$$u_z = v_z = 0, \tag{2.16}$$

$$w = 0. \tag{2.17}$$

By (2.15) and (2.16) we are excluding surface forcing through heat/salt fluxes and wind respectively. As will be discussed in §3.1, the eddy circulation in the channel is caused by perturbing an initial mean flow. The exclusion of any external forcing, therefore, means that the eddies cannot be sustained and will eventually die out through dissipative and viscous effects. In other words, the model will be used in a 'spin-down' mode.

The effect of the rigid lid approximation (2.17) is to filter out fast-propagating external gravity waves. Although this condition prevents any movement of the sea surface, the model does allow for a surface pressure (the pressure provided by the rigid lid) from which we can infer a sea surface height (relative to $z = 0$) through the hydrostatic relation (2.6).

2.3 Method of Solution

The method used to solve the equations involves separating the velocity into a baroclinic and barotropic mode and solving prognostic equations for each separately (Bryan, 1969). This mode separation technique which allows for a more efficient calculation of the velocity fields, also has the added advantage of enabling the elimination of the surface pressure from the equations altogether.

The velocity is defined by,

$$\begin{aligned} u &= \bar{u} + \hat{u}, \\ v &= \bar{v} + \hat{v}. \end{aligned} \tag{2.18}$$

where $\bar{(\,)} = H^{-1}\int_{-H}^{0}(\,)dz$, is the barotropic component, and $\hat{(\,)}$ denotes the baroclinic component. First, consider the evaluation of the barotropic component of the flow field. Integrating (2.7) vertically over the total depth of the ocean and applying boundary conditions (2.14) and (2.17) on w gives,

$$\left(\int_{-H}^{0} u dz\right)_{\lambda} + \left(\int_{-H}^{0} v\cos\phi dz\right)_{\phi} = 0. \tag{2.19}$$

From this nondivergence condition for the vertically integrated transport, a barotropic streamfunction, ψ, can be defined such that

$$\begin{aligned} \bar{u} &= \int_{-H}^{0} u dz = -(Ha)^{-1}\psi_{\phi}, \\ \bar{v} &= \int_{-H}^{0} v dz = -(Ha\cos\phi)^{-1}\psi_{\lambda}. \end{aligned} \tag{2.20}$$

Integrating the hydrostatic relation (2.6) from a depth z to the surface gives,

$$p(z) = p^s + \int_z^0 \rho g dz', \tag{2.21}$$

where p^s is the pressure at the ocean surface. A predictive equation for the barotropic streamfunction is determined by averaging (2.1) vertically and using (2.21) to yield,

$$\begin{aligned} \bar{u}_t - f\bar{v} &= -(\rho_0 a \cos\phi)^{-1}\left[p^s_\lambda + gH^{-1}\int_{-H}^0 \left(\int_z^0 \rho_\lambda dz'\right) dz\right] + \bar{G}^\lambda, \\ \bar{v}_t + f\bar{u} &= -(\rho_0 a)^{-1}\left[p^s_\phi + gH^{-1}\int_{-H}^0 \left(\int_z^0 \rho_\phi dz'\right) dz\right] + \bar{G}^\phi, \end{aligned} \tag{2.22}$$

where $\bar{G}^\lambda$ and $\bar{G}^\phi$ are given by,

$$\begin{aligned} \bar{G}^\lambda &= H^{-1}\int_{-H}^0 (a^{-1}uv\tan\phi - \mathcal{L}(u) + F^\lambda)dz, \\ \bar{G}^\phi &= H^{-1}\int_{-H}^0 (-a^{-1}u^2\tan\phi - \mathcal{L}(v) + F^\phi)dz. \end{aligned} \tag{2.23}$$

The surface pressure term in (2.22) can be eliminated by applying the curl_z operator defined as,

$$\mathrm{curl}_z(\alpha_1, \alpha_2) = (a\cos\phi)^{-1}(\alpha_{2\lambda} - (\alpha_1\cos\phi)_\phi). \tag{2.24}$$

This procedure leads to the barotropic vorticity equation from which ψ can be determined;

$$\nabla^2\psi_t + \beta\psi_\lambda = H\,\mathrm{curl}_z(\bar{G}^\lambda, \bar{G}^\phi), \tag{2.25}$$

where $\beta = df/d\phi$. The appropriate boundary conditions on ψ at the side walls are, according to (2.12),

$$\psi_\lambda = \psi_\phi = 0. \tag{2.26}$$

This condition requires that ψ be constant at the wall and hence without loss of generality can be set to zero there. (2.25) and (2.26) together with (2.20) provide the prognostic equations for the determination of the barotropic component of the velocity.

The baroclinic component of the velocity is predicted by first introducing a temporary velocity (u', v') defined simply as the velocity calculated from the horizontal momentum equations (2.1) without the surface pressure term from (2.21);

$$\begin{aligned} u'_t &= -\mathcal{L}(u) + (f + a^{-1}u\tan\phi)v - g(\rho_0 a\cos\phi)^{-1}\int_z^0 \rho_\lambda dz' + F^\lambda, \\ v'_t &= -\mathcal{L}(v) - (f + a^{-1}u\tan\phi)u - g(\rho_0 a)^{-1}\int_z^0 \rho_\phi dz' + F^\phi. \end{aligned} \tag{2.27}$$

Now noting that the surface pressure, p^s, is not a function of depth, the baroclinic velocity components can be written simply as,

$$\begin{aligned} \hat{u} &= u' - \bar{u'}, \\ \hat{v} &= v' - \bar{v'}. \end{aligned} \tag{2.28}$$

Hence the baroclinic component is calculated by solving (2.27) (since the right hand sides of these equations are known) together with (2.28).

To summarize, the solution is determined by solving prognostic equations (2.25) with (2.26) and (2.20) for the barotropic velocity, (2.27) with (2.28) for the baroclinic velocity, and (2.8) and (2.9) for temperature and salinity. Diagnostic calculations are then made to determine the vertical velocity from (2.7), the density from (2.10) and the baroclinic pressure from (2.6).

2.4 Numerical Procedure

The system of equations described in the previous section are solved numerically using finite difference methods. The formulation is based on the differencing scheme of Arakawa (1966) and Arakawa and Lamb (1977) in which the equations are solved on a B-grid subject to certain integral constraints. Details may be found in Bryan (1969) but will not be described in this thesis.

Figures 2.1(a) and (b) illustrate the arrangement of the variables on the B-grid for an arbitrary configuration (i.e., the topography and variable grid spacing shown are not

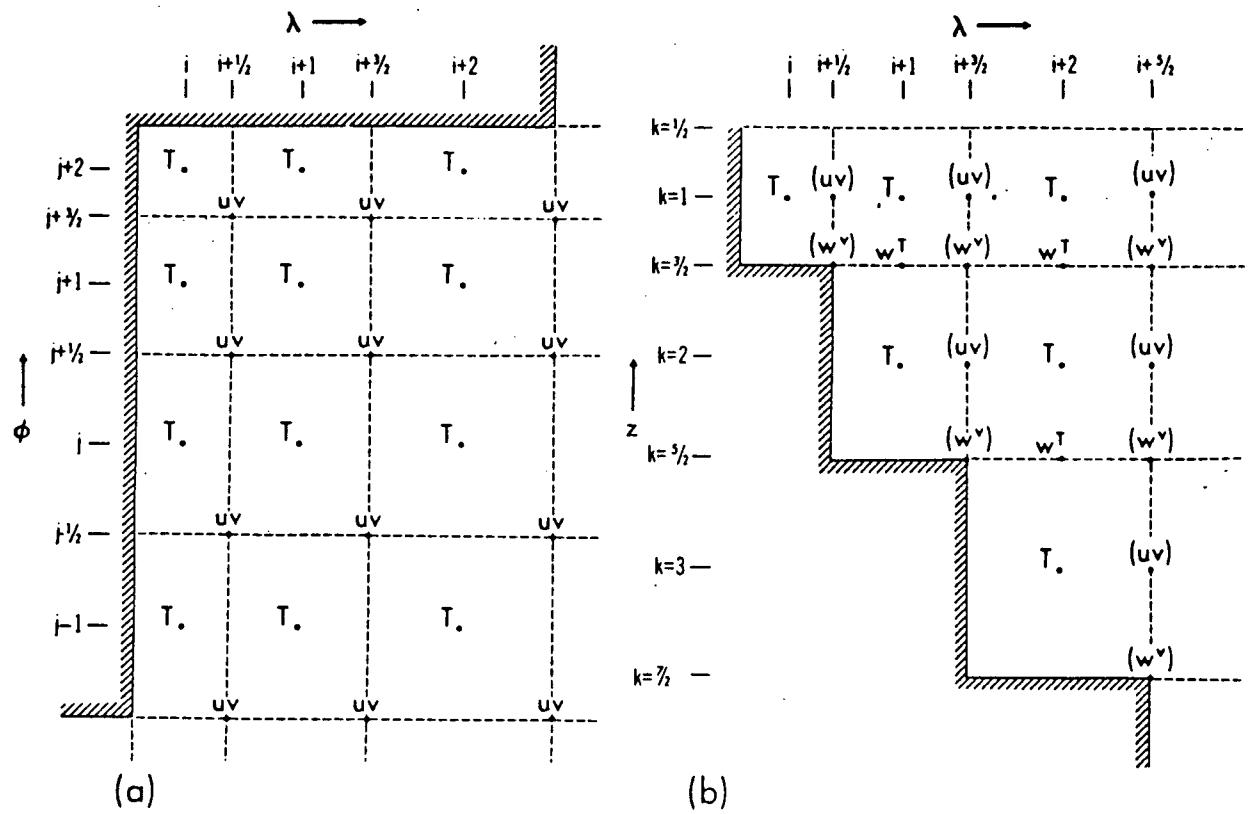

Figure 2.1: Variable arrangement on the B-grid (Arakawa, 1966) for an arbitrary configuration in (a) the horizontal plane and (b) the vertical plane (taken from Cox (1984)).

specific to the model application in this study). The horizontal grid (Figure 2.1(a)) is arranged in such a way that the horizontal velocity components are evaluated at points half a grid point away in each direction from those of the tracers and the streamfunction. In the vertical plane (Figure 2.1(b)) these variables are defined halfway between the vertical grid spaces. The vertical velocities w^T and w^v are defined at the level dividing each vertical grid space. They are located directly below their associated temperature and velocity variables and are used accordingly in the advection term for the temperature conservation equation and horizontal momentum equation.

Table 2.1: Vertical grid spacing (in metres).

level	depth (m)	
	(u, v, T, S) grid	w grid
		0
1	10	
		20
2	35	
		50
3	70	
		90
4	120	
		150
5	200	
		250
6	325	
		400
7	525	
		650
8	850	
		1050
9	1350	
		1650
10	2100	
		2550

The channel model in this study covers a 450 km (east-west) by 300 km (north-south) area and has uniform horizontal resolution of 15 km in both directions. The southern wall of the channel is located at 35° N. There are 10 variably spaced vertical levels ranging from 20 m in the uppermost level to 750 m in the bottom level. The total depth of the channel is 2550 m. Table 2.1 indicates the grid spacing between levels for the (u, v, T, S) variables and w variable.

The model uses leap-frog differencing in time substituted periodically with a forward time step in order to suppress the splitting of the solution between adjacent time levels.

The time step, Δt, must be chosen to satisfy the CFL stability criterion,

$$\Delta t \leq \Delta x / c_{\max}, \tag{2.29}$$

where Δx is the horizontal grid spacing and $c_{\max}$ is the maximum wave phase speed in the model. A time step of 15 minutes was used for the numerical experiments in this study.

The values for the horizontal and vertical viscosity coefficients, A_{MH} and A_{MV}, are taken to be constant in the λ, ϕ and z directions. In the initial diagnostic spin-up run (described in §2.5) $A_{MH} = 10^7\,\mathrm{cm^2/s}$ and $A_{MV} = 1\,\mathrm{cm^2/s}$ are used.[1] In the prognostic assimilation experiments (described in Chapter 3) A_{MH} is decreased by a factor of 10 ($A_{MH} = 10^6\,\mathrm{cm^2/s}$) to facilitate the generation of eddies and to prevent their rapid damping. It should be noted that since a cyclic condition is imposed at the east-west ends of the channel, a Munk boundary layer at the western boundary (Munk, 1950) does not exist. Therefore, the criterion on A_{MH} and the horizontal grid spacing for resolving the Munk layer (Bryan et al., 1975) is not required.

A further requirement on the eddy viscosities arising from the use of centered differences, is that the horizontal and vertical grid Reynolds numbers be less than 2 (Chen, 1971),

$$\begin{aligned} \mathrm{Re}_H &= U\Delta x / A_{MH} < 2, \\ \mathrm{Re}_V &= W\Delta z / A_{MV} < 2, \end{aligned} \tag{2.30}$$

where U and W are a characteristic horizontal and vertical velocity respectively. Although these criteria are grossly violated in this study (i.e., $\mathrm{Re}_H = 150$ and $\mathrm{Re}_V = 75$ for $U = 100\,\mathrm{cm/s}$, $W = 10^{-3}\,\mathrm{cm/s}$, $\Delta x = 15\,\mathrm{km}$, $\Delta z = 750\,\mathrm{m}$, $A_{MH} = 10^6\,\mathrm{cm^2/s}$, and $A_{MV} = 1\,\mathrm{cm^2/s}$), $\mathrm{Re}_H > 2$ and $\mathrm{Re}_V > 2$ are only necessary criteria but not sufficient ones for the existence of a computational mode. In fact, for short duration initial

[1] Cgs and SI units are used interchangeably throughout the thesis.

value problems smooth solutions are often obtained even when (2.30) is not satisfied (Bryan et al., 1975). The existence of the spurious mode appears in the model solution as a rather distinctive oscillation in sign between adjacent grid points. This behaviour is never observed in the model data for the experiments conducted in this study, implying that violating (2.30) is not critical here.

The horizontal diffusivity is set to $4.0 \times 10^5\,\mathrm{cm}^2/\mathrm{s}$ in all experiments (of course the choice of the diffusivities is irrelevant for the diagnostic spin-up where the density field is held fixed). Vertical diffusivity is assigned a depth dependence ranging from $A_{HV} = 0.3\,\mathrm{cm}^2/\mathrm{s}$ at the surface to $A_{HV} = 0.87\,\mathrm{cm}^2/\mathrm{s}$ at the bottom of the channel, according to the expression (Bryan and Lewis, 1979),

$$A_{HV} = A_{HV_{z_0}} + \pi^{-1} \arctan(4.5 \times 10^3 (z - z_0)), \tag{2.31}$$

where z is the depth (measured positive down), $z_0 = 2500\,\mathrm{m}$, and $A_{HV_{z_0}} = 0.8\,\mathrm{cm}^2/\mathrm{s}$ is the value of A_{HV} at z_0. (2.31) is formulated based on observations which indicate that vertical mixing is lowest within the thermocline and increases below it. Criteria similar to (2.30) also exist for the diffusivities, A_{HH} and A_{HV}, (i.e., the Peclet numbers, $\mathrm{Pe}_H = U\Delta x/A_{HH} < 2$ and $\mathrm{Pe}_V = W\Delta z/A_{HV} < 2$) but as with the Reynolds criteria, violation of the Peclet criteria is not sufficient for the existence of a computational mode.

2.5 Initial Conditions

Unlike many of the simpler models (e.g., QG, reduced gravity), the PE model is ideal for studying complex realizations of the ocean circulation. In this study, the idealized numerical experiments are performed in highly nonlinear and energetic flow field conditions, similar to those occurring in the Gulf Stream system.

The initial temperature and salinity fields are chosen to represent mean Gulf Stream conditions. Salinity is made uniform at each level and the values, taken from Emery and Dewar (1982), are tabulated in Table 2.2. The initial temperature distribution is uniform along the channel but has a cross-channel and depth dependence according to the expression,

$$T(y,z) = T_0 + T^* f(y) g(z), \tag{2.32}$$

where

$$\begin{aligned} f(y) &= (5 + \tanh(\delta y))/2, \\ g(z) &= (1 + \epsilon z) e^{-2\epsilon z}, \end{aligned} \tag{2.33}$$

with y and z the cross-channel and depth coordinates respectively.[2] The constant parameters T_0, T^*, ϵ and δ are chosen so that (2.32) is consistent with Gulf Stream conditions. The values are 4°C for the deep water temperature T_0, 7°C for T^*, $1/650\,\mathrm{m}^{-1}$ for the inverse vertical depth scale ϵ, and $1/3 \times 10^4\,\mathrm{m}^{-1}$ for the inverse horizontal length scale δ. The expression is similar to that used by Orlanski and Cox (1973) in their study of baroclinic instabilities in the Gulf Stream.

Figure 2.2 shows a cross-channel section of the initial temperature field calculated from (2.32). The variation in temperature is greatest at the surface where it ranges from approximately 21°C at the southern wall to approximately 15°C at the northern wall. The steep gradient in the isotherms over the central part of the channel is due to the hyperbolic tangent term in (2.33). Over this region, a strong cross-channel (north to south) pressure gradient, p_y, is set-up which, assuming a steady state and geostrophy, will be balanced by a Coriolis force, $-\rho_0 f u$.

To achieve an approximate balanced state, a diagnostic run is performed whereby the model is integrated forward from rest using the initial density field just described

[2]From this point on, the zonal, meridional and vertical directions will be referred to in Cartesian coordinates (x, y, z) instead of spherical coordinates (λ, ϕ, z).

Table 2.2: Initial salinity (in $^0/_{00}$) for each level.

level	depth (m)	salinity ($^0/_{00}$)
1	10	36.493
2	35	36.515
3	70	36.541
4	120	36.542
5	200	36.501
6	325	36.431
7	525	36.057
8	850	35.284
9	1350	35.042
10	2100	34.987

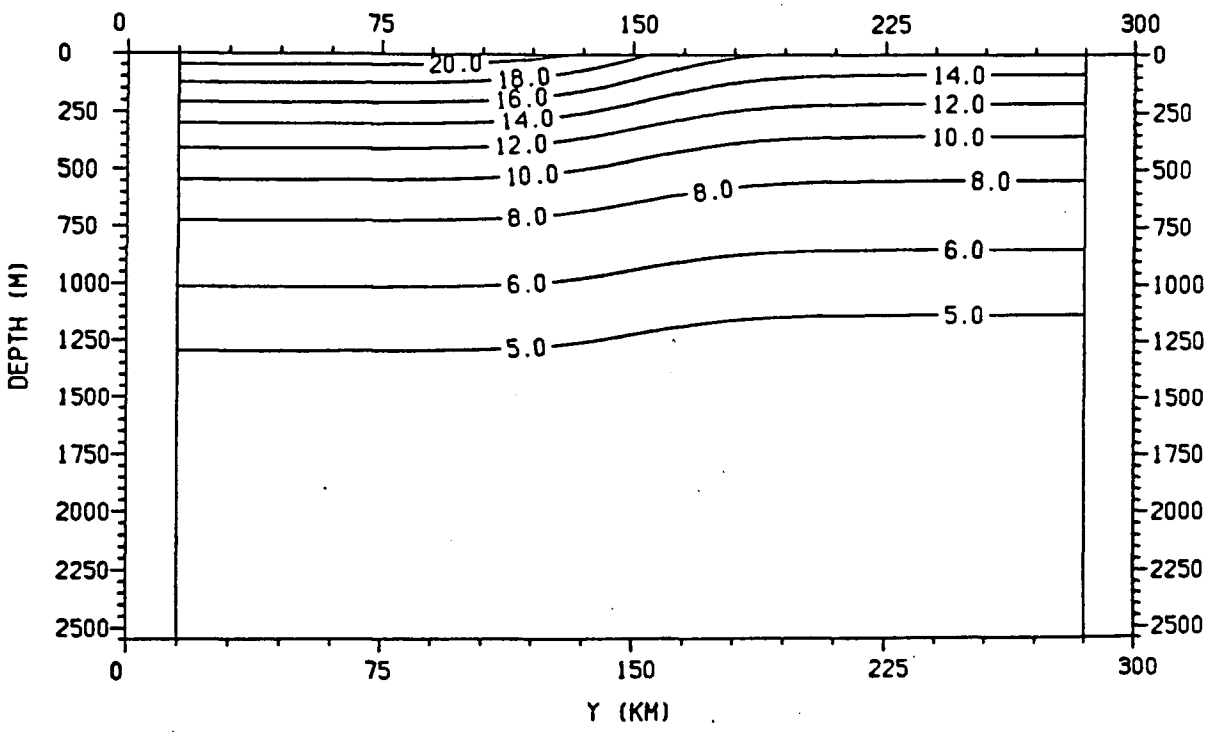

Figure 2.2: Cross-channel section of the initial temperature field (in °Celcius).

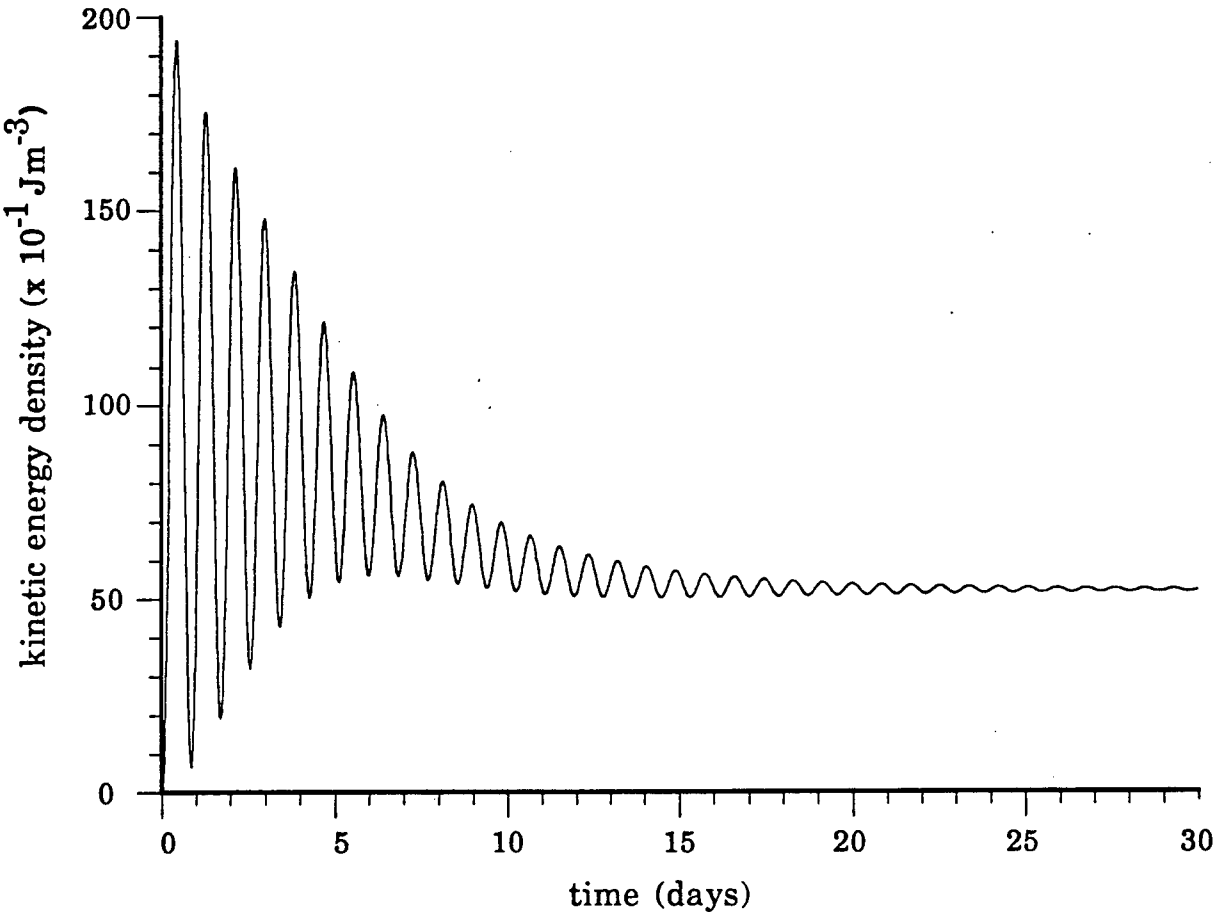

Figure 2.3: Kinetic energy density for the diagnostic run.

until a quasi-equilibrium is attained. Figure 2.3 showing the kinetic energy density as a function of the time integration of the model illustrates the spin-up behaviour of the model. Large inertial oscillations of period 20.9 hours are the dominant feature in the diagnostic spin-up but rapidly die out as the model approaches equilibrium after approximately 30 days.

Figure 2.4 shows current vectors in the top level of the model after the 30 day run. In the central region of the channel (i.e., in the vicinity of the density front), a strong zonally uniform eastward jet (in approximate geostrophic balance) has been set-up with speeds reaching up to 100 cm/s. The eastward jet vanishes at a depth of

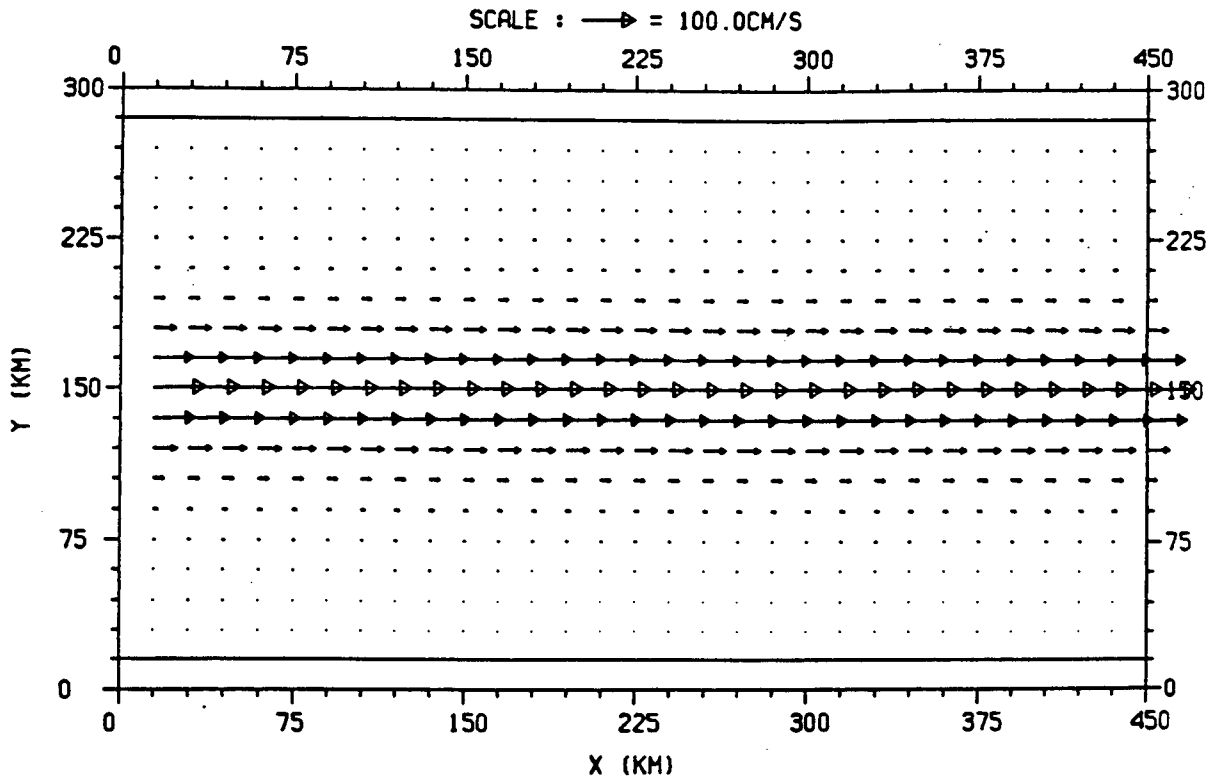

Figure 2.4: Velocity vectors (in cm/s) at level 1 (10 m) of the model after the 30 day diagnostic run.

approximately 800 m below which the jet reverses to a much weaker westward flow. The given temperature and salinity fields, together with the corresponding geostrophic velocity fields generated by this diagnostic run, represent the of initial conditions for the different assimilation experiments described in the next chapter.

Chapter 3

The Assimilation Experiments: Procedure

3.1 Methodology

The basic methodology of the assimilation experiments is similar to the 'identical twin' approach. (Moore et al., 1987, Malanotte-Rizzoli et al., 1989, Holland and Malanotte-Rizzoli, 1989). The procedure consists of setting up three different model runs as follows:

(i) The 'Real Ocean' (Run R): The 'real ocean' in this case refers to a simulated reference ocean. The data provided by this model are used; (a) as 'observations' for assimilation; and (b) to estimate the errors in the simulation runs;

(ii) The 'Simulation' Model (Run A): The 'simulation' model represents in some sense, an imperfect model of the 'real ocean' as described by Run R. In this study, the actual physics contained in the simulation model is assumed to be perfect but the data used to initialize the model inaccurate; and

(iii) The 'Assimilation' Model (Run B): Using the identical simulation model of Run A, an additional run is performed. This time SST 'observations' from Run R are continuously assimilated as the model is integrated forward in time. The assumptions regarding the SST data are that they are (1) available on a daily basis with perfect spatial resolution and (2) free of measurement error. The assimilation technique employed is described in §3.2.

By comparing these three model runs, we can determine how effective SST assimilation is in driving the imperfect model back toward the 'real ocean'. A clear advantage in specifying a simulated reference ocean is that it provides us with a complete description of the 'real ocean' circulation. However, because a strong compatibility exists between the 'observations' and the model (since they are themselves generated by the model), it should be kept in mind that convergence, if at all, of the 'assimilation' model toward the 'real ocean' would be slower in assimilation experiments using real observational data.

As mentioned, the simulation models (Runs A and B) have a slightly different initial condition from the reference ocean (Run R) – corresponding to an imperfect data-set being used in the simulation models. In both runs a small random perturbation is introduced at each grid point into the initial mass and flow fields described in §2.5. The magnitude of the perturbation which is never more than 1% of the model data is calculated using a random number generator sequence. In order to establish different initial conditions for the reference ocean and the simulation model, one random sequence is used for Runs A and B and another sequence for Run R.

The introduction of the perturbation into the initial fields serves an additional purpose as hinted in §2.2. Since the balanced initial velocity and density fields of §2.5 are uniform in every cross-section along the channel, the only way to permit unstable wave growth and the subsequent formation of eddies is by disturbing the geostrophic mean state. This instability in the mean flow is achieved by superimposing random noise in the initial conditions and allowing the model solution to evolve prognostically thereafter. Because the perturbed initial fields of the reference ocean and of the simulation models are different however, the transient features of both runs (i.e., the formation of eddies from the jet) are quite distinct. The characteristics of the flow field will be discussed in more detail in Chapter 4.

3.2 The Assimilation Technique

The technique used to assimilate SST 'observations' is based on the simple Newtonian relaxation or 'nudging' scheme originally developed in meteorology by Anthes (1976) for numerical weather predicition models and more recently applied by Verron (1990) and Holland and Malanotte-Rizzoli (1989) in their study of altimetric data assimilation in a quasi-geostrophic (QG) ocean model. In this method, model variables are relaxed toward observations by adding extra forcing (nudging) terms to the model equations which are proportional to the difference between observations and the corresponding model predicted fields. The robust diagnostic ocean model of Sarmiento and Bryan (1982) incorporated a similar technique to prevent model temperatures and salinities from drifting too far from climatological mean values. In the four dimensional data assimilation approach, however, the nudging term is used to assimilate time dependent ocean observations in the hope of reproducing the transient characteristics of the real ocean circulation.

In this study, the nudging term appears in the model formulation as a surface heat forcing, $Q(x,y,t)$, given by,

$$Q(x,y,t) = C\left(T^{\text{obs}}(x,y,t) - T_1(x,y,t)\right), \tag{3.1}$$

where $T^{\text{obs}}(x,y,t)$ are SST observations, $T_1(x,y,t)$ are the corresponding temperatures in the uppermost level of the model, and C is a relaxation parameter with dimensions of inverse time which controls the rate of SST assimilation.[1] In accordance with the methodology of §3.1, SST 'observations' are represented (exactly) by the top level temperature field of the 'real ocean' (Run R) (i.e., $T^{\text{obs}}(x,y,t) = T_{1R}(x,y,t)$) and the

[1]Strictly speaking, the actual heat flux, Q^* (in Wm^{-2}), into the top level of the model is $Q^* = Q\rho_0 c_p \Delta z_1$ where ρ_0 is the reference density, c_p is the specific heat at constant pressure and Δz_1 is the depth of the top level.

level 1 temperature in (3.1) corresponds to the level 1 temperature in the 'assimilation' model (Run B) (i.e., $T_1(x,y,t)=T_{1B}(x,y,t)$).

There is an apparent similarity between the boundary nudging term (3.1) and the Haney (1971) formulation of the surface thermal boundary condition used in most OGCMs. The interpretation of the two surface heat flux conditions, however, is quite different. In the Haney surface heat flux parameterization, a linear damping boundary condition like that of (3.1) was derived using a heat budget analysis based on longtitudinal and time averaged atmospheric conditions. The observed temperature T^{obs}, in this case, is a zonally and time independent apparent atmospheric temperature, $T^*(y)$, which, in practice, is usually taken as the observed sea surface temperature or surface air temperature. The linear damping coefficient was also determined from zonally and time averaged data.

The nudging term (3.1), however, is an artificial heat source/sink at the upper boundary which acts to constrain the transient top level temperature field of the model to closely follow observations. Moreover, the choice of the particular form of the relaxation paramater C is completely at our disposal. Holland and Malanotte-Rizzoli (1989), for instance, used a time dependent Gaussian nudging coefficient centred around the actual time of the observations to assimilate coarse resolution vorticity information (from altimetery) into a QG ocean model. In all of the idealized assimilation experiments performed here, C is simply taken to be constant in time and space.

In this study, 'satellite observations' of SST are assumed available on a periodic daily basis. To establish a time-continuous approximation to the SST 'observations', a linear interpolation in time is used between available SST data sets. The top level temperature field of Run B is then updated at every timestep with this interpolated SST data using the nudging formula (3.1). The first SST update is performed exactly one day after the small random perturbation is introduced into the model initial conditions.

Two important limiting cases of (3.1) are evident. First, in the case of infinite assimilation ($C = \infty$), the top level temperature field in Run B is completely replaced at every timestep by the corresponding 'observations' from Run R (i.e., $T_{1B}(x,y,t) = T'_{1R}(x,y,t)$, where T'_{1R} is the linearly interpolated 'observational' data-set). This rather abrupt form of data assimilation (or more appropriately direct data insertion) will have the most profound effect on the model simulation. The other extreme case is when the nudging coefficient is chosen to be zero for all time ($C = 0$). In this case, no observational data are assimilated into Run B (i.e., $T_{1B}(x,y,t) = T_{1A}(x,y,t)$) and the model is identical to the strictly predictive 'simulation' model, Run A.

3.3 Diagnostics

A quantitative way of measuring the success of the assimilation experiments is through the root mean square (RMS) error for the various fields defined by,

$$\mathrm{RMS}_k^{(A,B)} = \left[\sum_{i=1}^{I} \sum_{j=1}^{J} (X_{i,j,k}^{R} - X_{i,j,k}^{(A,B)})^2 / N \right]^{1/2}, \tag{3.2}$$

where the parameter X represents any of the model variables and superscripts A, B and R refer to those Runs respectively. The RMS error is evaluated at each k^{th} level and normalized by the total number of horizontal grid points $N = I \times J$. RMS_k^A and RMS_k^B correspond to the error between Run R and Run A (i.e., without SST assimilation) and Run R and Run B (i.e., with SST assimilation) respectively.

By examining the time evolution of the RMS errors together with time series and instantaneous plots of the various model data fields, the following questions can be answered:

(1) Does the 'assimilation' model offer an improvement over the 'simulation' model in terms of its ability to reconstruct the 'real ocean'? If so, we ask more specifically;

(2) For which fields (e.g., velocity, streamfunction, temperature etc.) is the error reduction greatest?

(3) How will SST assimilation affect the deeper circulation?

(4) Is there an optimal value of the nudging coefficient C which minimizes RMS_k^B?

The results from the assimilation experiments are presented in the next chapter.

Chapter 4

The Assimilation Experiments: Results

4.1 Flow Characteristics of the Reference Ocean

In this section, a qualitative description is given of the basic characteristics of the 'real ocean' flow field. The flow fields of the 'simulation' and 'assimilation' models are characterized by similar scales of motion to that of the reference ocean and thus are not included in the general description here.

Run R was integrated forward from the perturbed initial state for a total of 120 days. The kinetic energy density for this time period (Fig. 4.1) shows quite clearly how the model responds to the perturbation. During the first ten days of integration there is very little activity in the channel. The only visible feature during this period is a series of low energy inertial oscillations. These high frequency oscillations are of little significance and occur because the diagnostic run which was used to generate the initial velocity field was never run to an absolute steady state (see Fig. 2.3). The effect of the perturbation is not apparent until day 10 when a sudden increase in the kinetic energy occurs. This abrupt energetic response corresponds to the rapid growth of unstable waves.

The growth of these waves is not continuous however, but occurs in two distinct stages. During the first stage, the kinetic energy increases with an e-folding time of approximately 14 days until around day 20. After this time the kinetic energy decreases

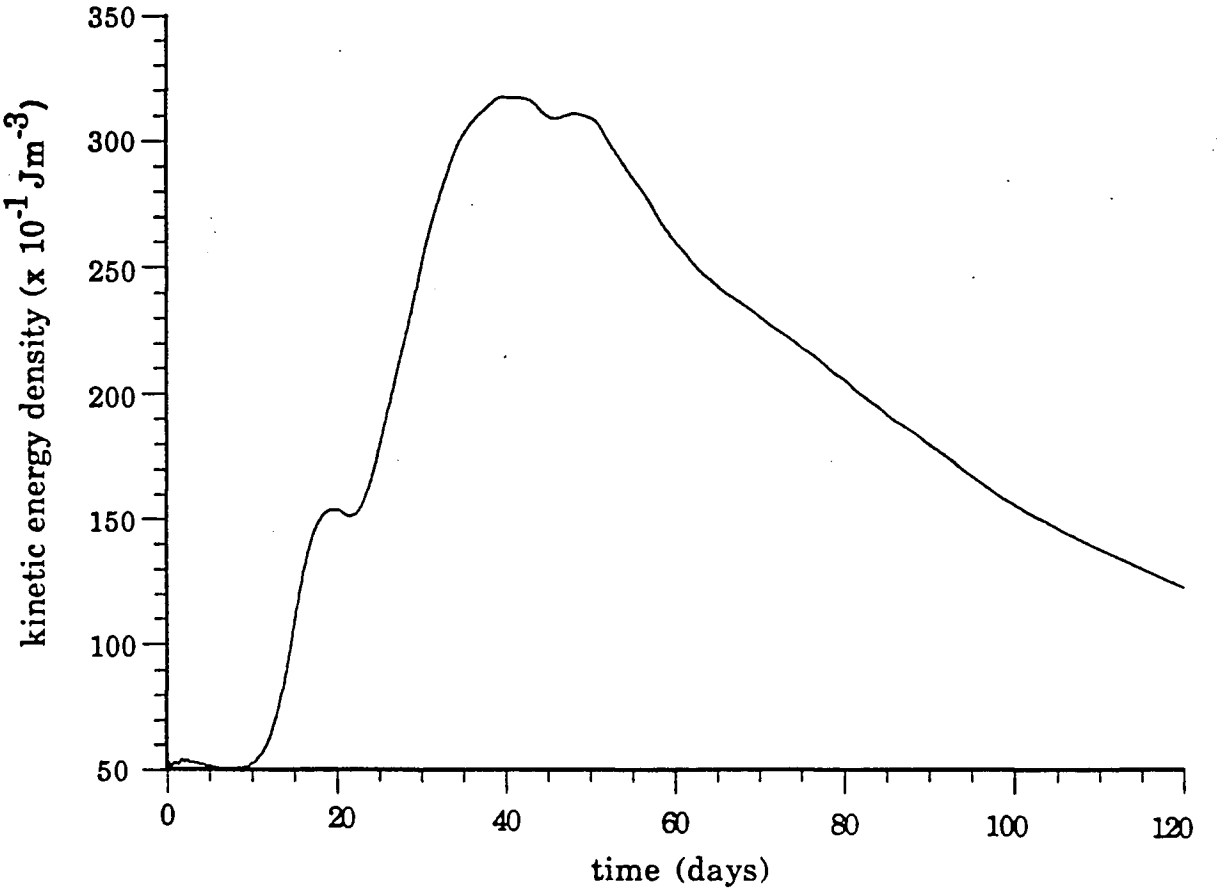

Figure 4.1: Kinetic energy density for Run R.

slightly before undergoing a second dramatic growth cycle around day 22 with an e-folding time of about 16 days. The kinetic energy reaches a maximum around day 40 and then decreases steadily for the remainder of the run (recall that there is no external forcing to maintain the flow).

Figure 4.2 and 4.3 show a sequence of upper level velocity vector plots at various times during the run. Ten days after the introduction of the perturbation, the jet still exhibits a strong eastward flow although now a slight meander is apparent (Fig. 4.2(a)). By day 30 the meander has become much more pronounced with a characteristic wavelength of about 225 km (Fig. 4.2(b)). Further steepening of the jet leads to the

eventual detachment of cyclonic and anticyclonic eddies as illustrated by the intense eddy field on day 60 (Fig. 4.2(c)). However, the rather narrow channel width (relative to the size of the eddies) prevents these eddies from drifting too far from the jet. As the model approaches a state of statistical equilibrium, the eddies coalesce or damp out so that ultimately the flow is dominated by two large circulation cells each having an east-west extent of 225 km and a north-south extent of 300 km (Fig. 4.3(d) and (e)).

The unstable wave development can be seen more clearly in the horizontal contours of the north-south (N-S) component of velocity shown at different depths (10 m, 200 m and 2200 m) in Figures 4.4, 4.5 and 4.6 for days 10, 30 and 70 respectively. After 10 days of integration (Fig. 4.4) the random perturbation has evolved into a fully developed wave pattern with the dominant or, more precisely, most unstable wave occuring at wavenumber 6 (the characteristic wavelength is $\lambda = 75$ km, that is, $L/6$ where $L = 450$ km is the total length of the channel). This wave-like behaviour is observed at all levels with the most coherent pattern occuring in the deepest level (Fig. 4.4(c)). By tracking a series of wave crests and troughs, a rough estimate of the phase speed was found to be on the order of 50 cm/s (eastward). Furthermore, these unstable waves exhibit an eastward phase tilt with depth which is a strong indication that they are a product of baroclinic instability (Pedlosky, 1979, pg. 462).

Figure 4.5 shows the wave development becoming much more intense by day 30, with the most unstable wave now appearing at wavenumber 2 ($\lambda = 225$ km) with an eastward phase speed of about 5 to 15 cm/s. Eventually this wave decreases its growth rate and another wave (wavenumber 1, $\lambda = 450$ km) starts to grow (Fig. 4.6). This wave dominates the channel variability from day 70 onward and is in the form of a westward propagating barotropic Rossby wave with phase speed between -5 to -7 cm/s.

The barotropic streamfunction is shown in Figure 4.7 for the same time sequence

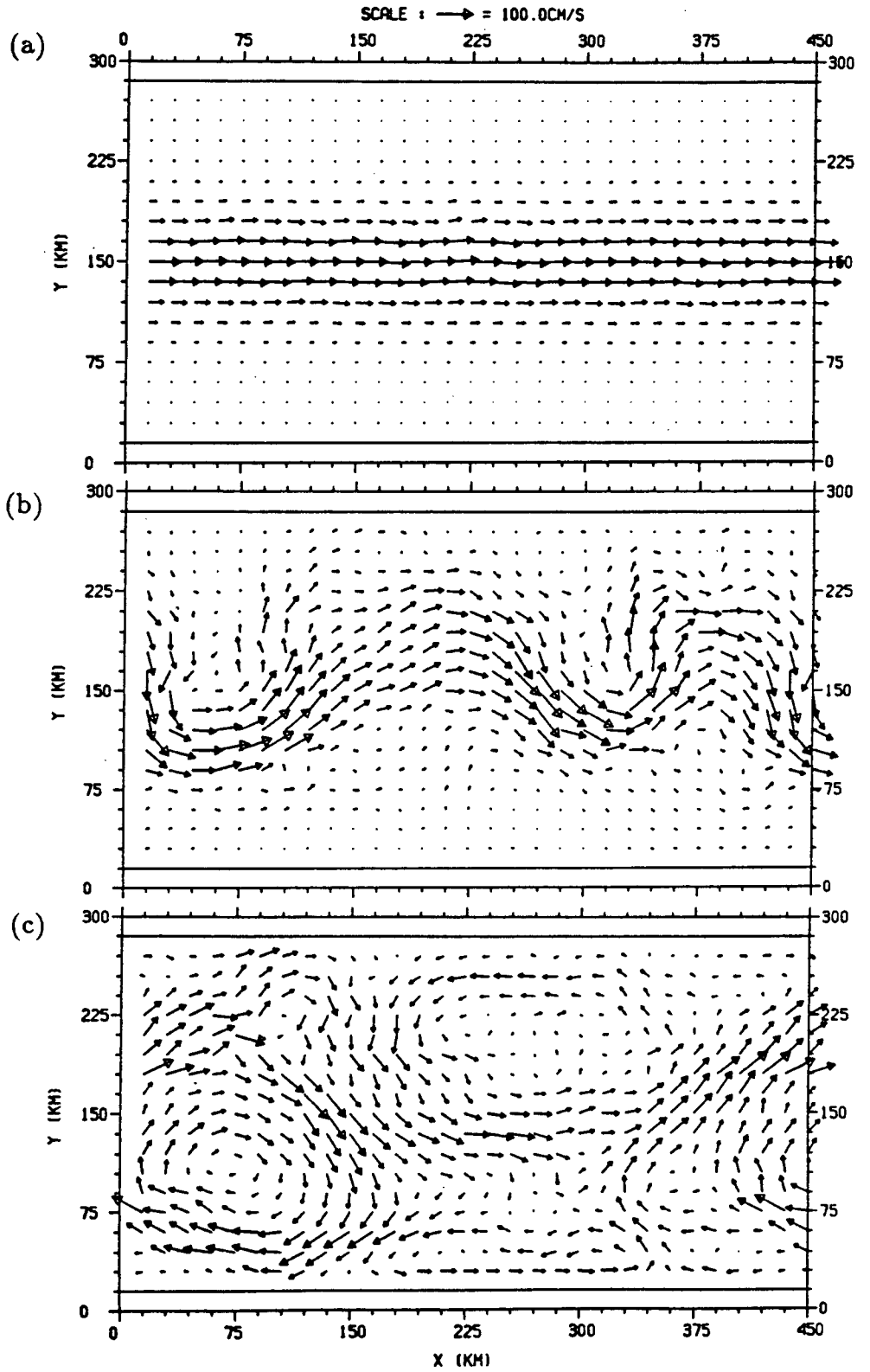

Figure 4.2: The 'Real Ocean': level 1 (10 m) horizontal velocity field on (a) day 10, (b) day 30 and (c) day 60.

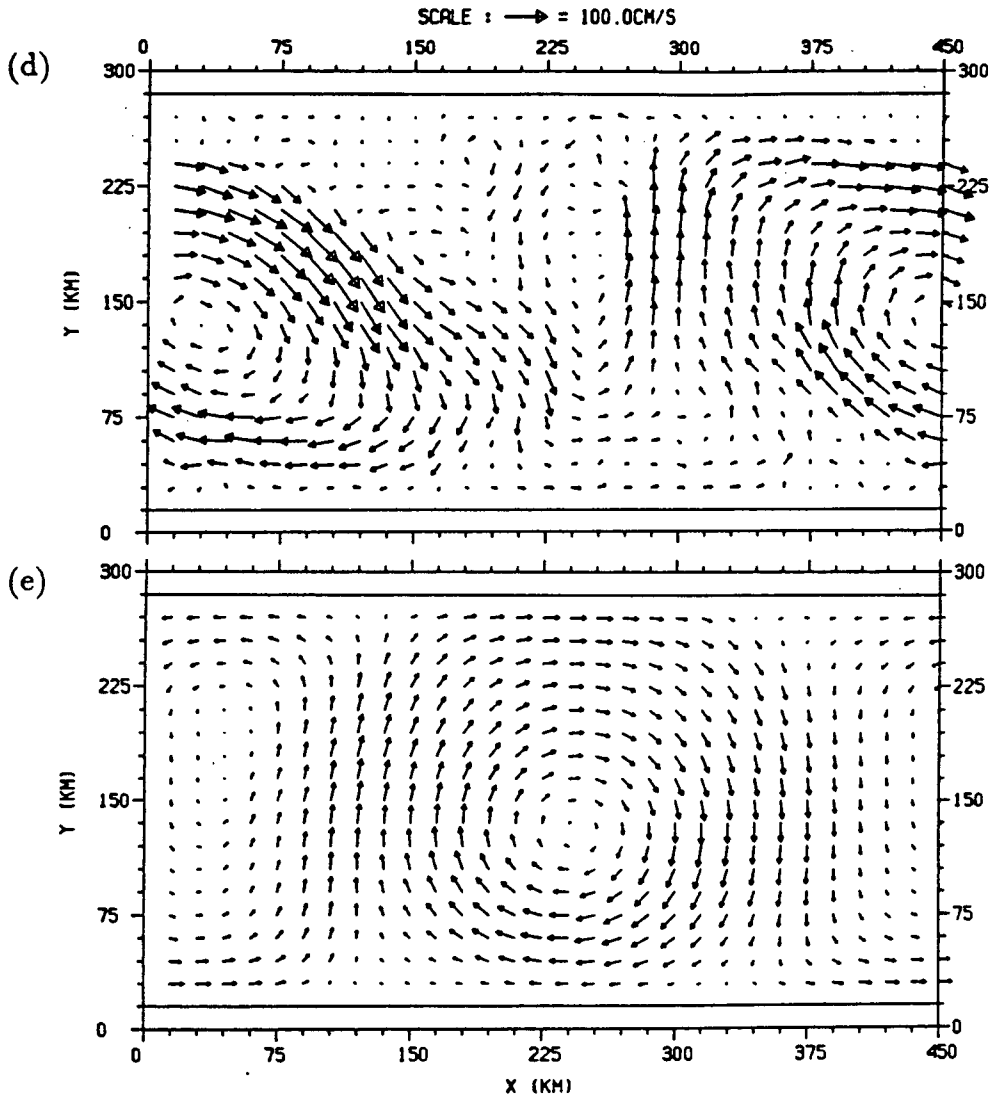

Figure 4.3: The 'Real Ocean': level 1 (10 m) horizontal velocity field on (a) day 70 and (b) day 120.

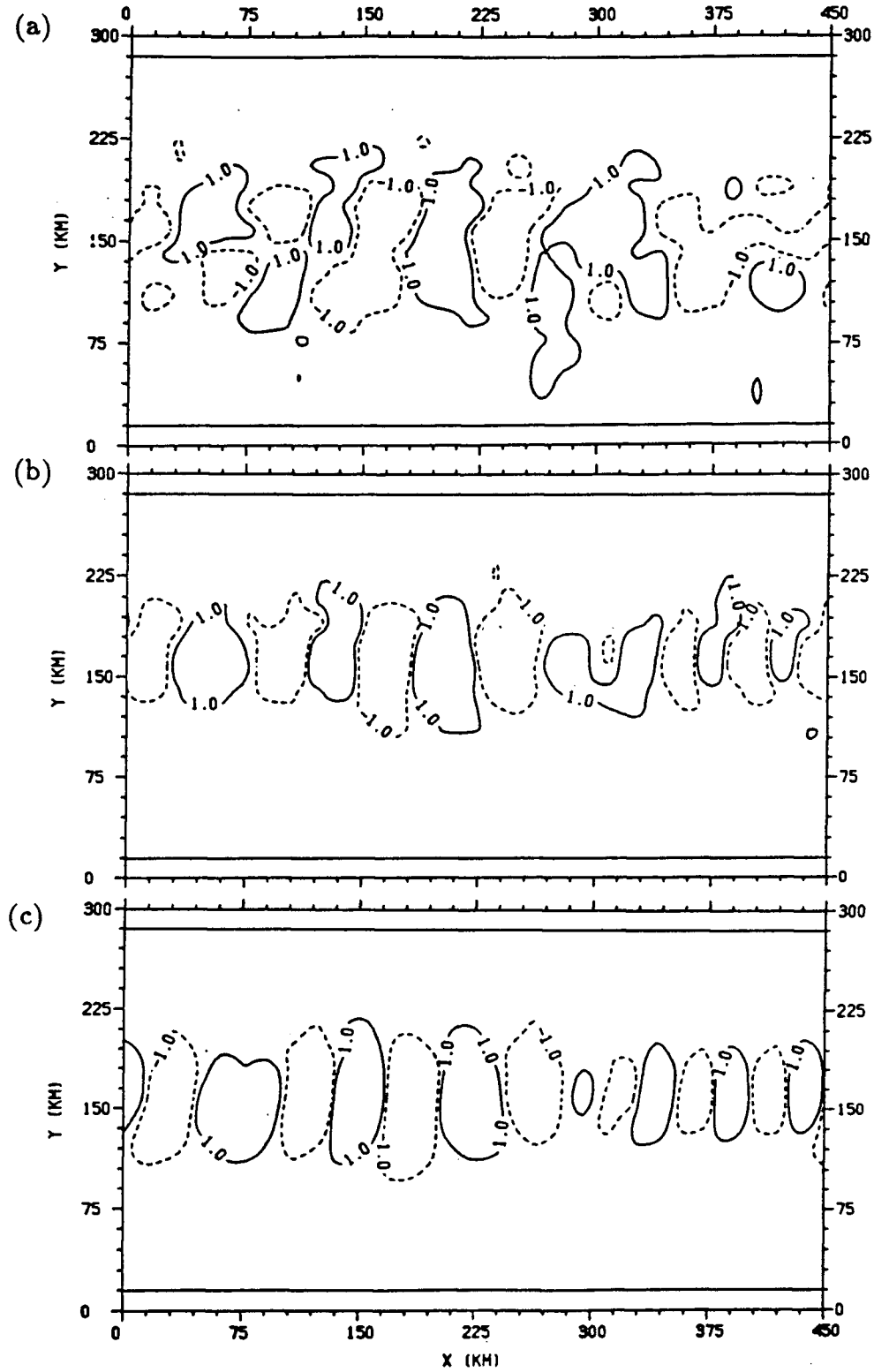

Figure 4.4: The 'Real Ocean': N-S velocity component (contour labels in cm/s) on day 10 at depths (a) 10 m, (b) 200 m and (c) 2200 m.

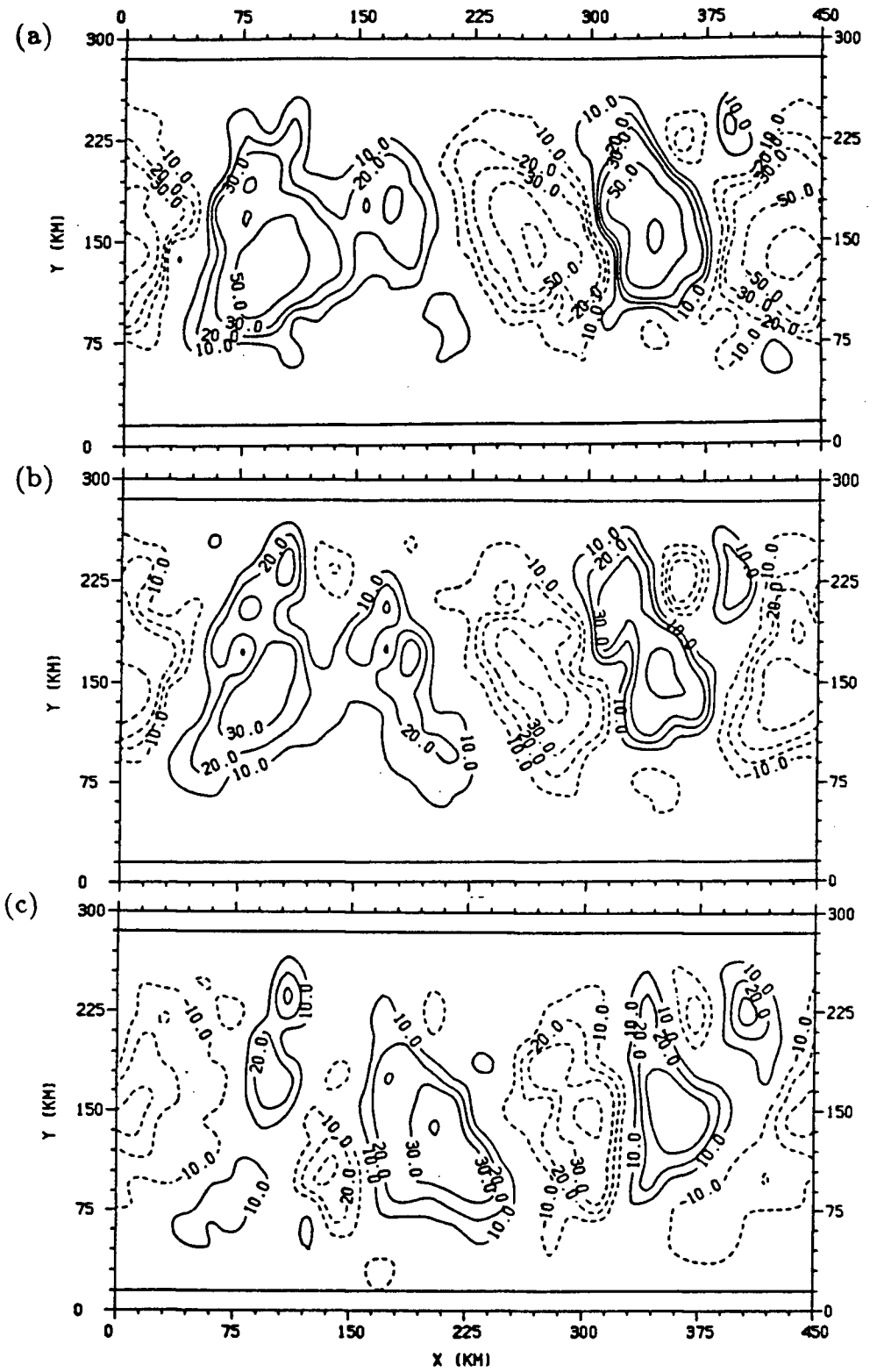

Figure 4.5: The 'Real Ocean': N-S velocity component (contour labels in cm/s) on day 30 at depths (a) 10 m, (b) 200 m and (c) 2200 m.

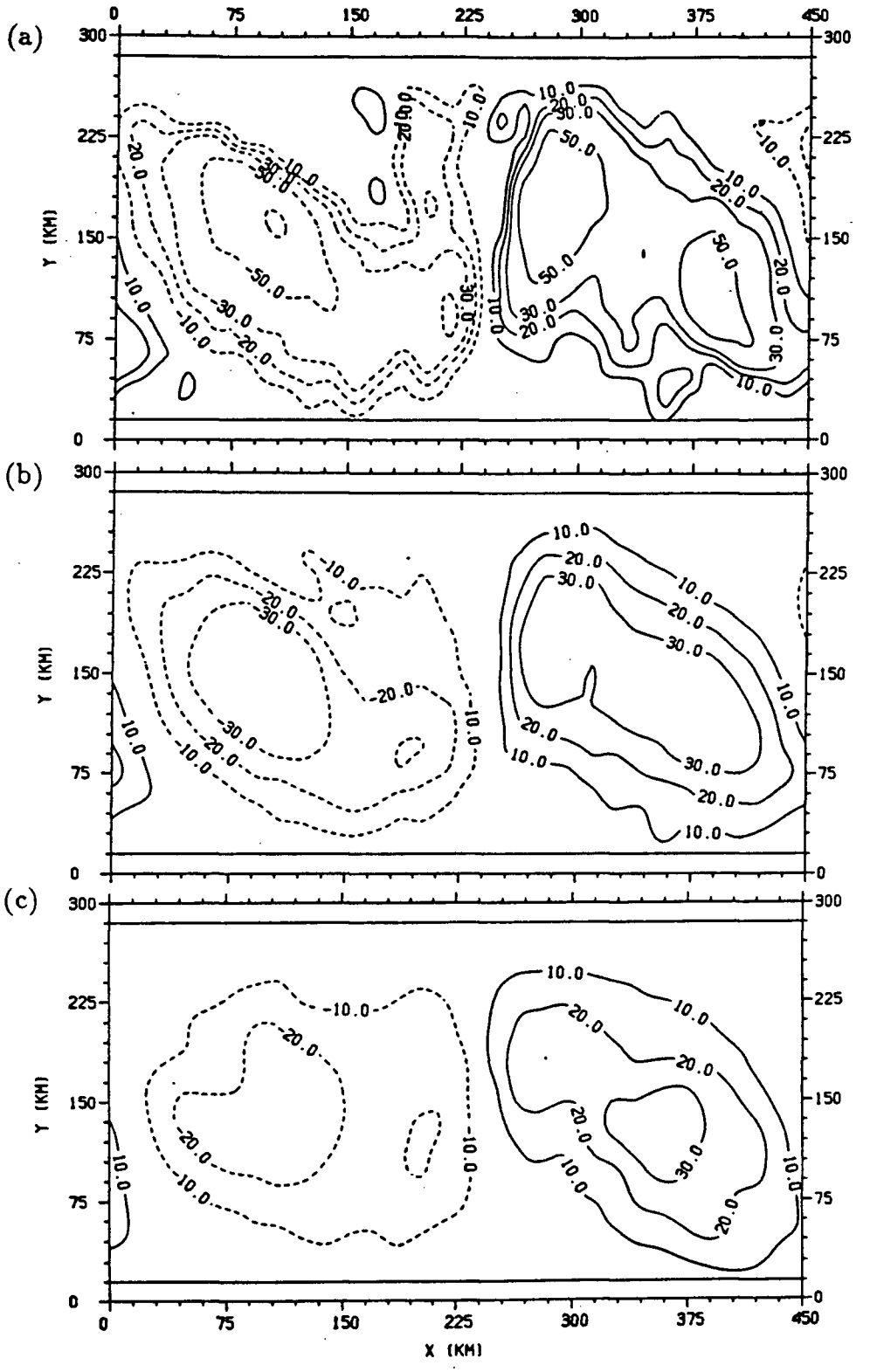

Figure 4.6: The 'Real Ocean': N-S velocity component (contour labels in cm/s) on day 70 at depths (a) 10 m, (b) 200 m and (c) 2200 m.

as the N-S velocity contour plots. Besides illustrating the evolving spatial scales of the flow, these snapshots show the transition from a primarily baroclinic flow field in the early stages of the run to a strong barotropic flow field (over 50 Sv on day 70) characterized by planetary waves of westward phase. In fact, this 'barotropification' is a common feature of unstable flows and arises from nonlinear interactions which act to vertically transfer, or cascade, energy from the shorter scales (i.e., scales on the order of the internal Rossby deformation radius — approximately 17 to 27 km in this case) to produce depth independent currents (Robinson, 1983).

The temperature anomaly, defined as the total temperature minus the temperature averaged in the along-channel direction,

$$T_{\text{anom}}(x, y, z) = T(x, y, z) - \overline{T}(y, z), \tag{4.1}$$

where

$$\overline{T}(y, z) = I^{-1} \sum_{i=1}^{I} T(x_i, y, z), \tag{4.2}$$

exhibits the same wave-like characteristics. Figure 4.8 shows the temperature anomaly in the uppermost level (10m) for the same three day time sequence. During the first 50 days, the anomalies are characterized by baroclinic planetary waves (Fig. 4.8(a) and (b)). The phase speeds of these higher (baroclinic) modes are weak, consequently the anomalies are advected eastward by the mean jet ($\approx$ 50 cm/s from Fig. 4.2). As the lowest (barotropic) mode grows, the westward phase speed increases while the eastward jet decreases in strength so that eventually large barotropic anomalies with westward phase propagation are observed (Fig. 4.8(c)).

To observe temporal variability, time series are plotted for several of the model variables located in the exact centre of the channel ($i = 15, j = 10$). Figure 4.9 shows the evolution of the temperature field at levels 1 (10 m) and 5 (200 m) for the total 120 day duration of the run. During the first 10 days, there is very little response in

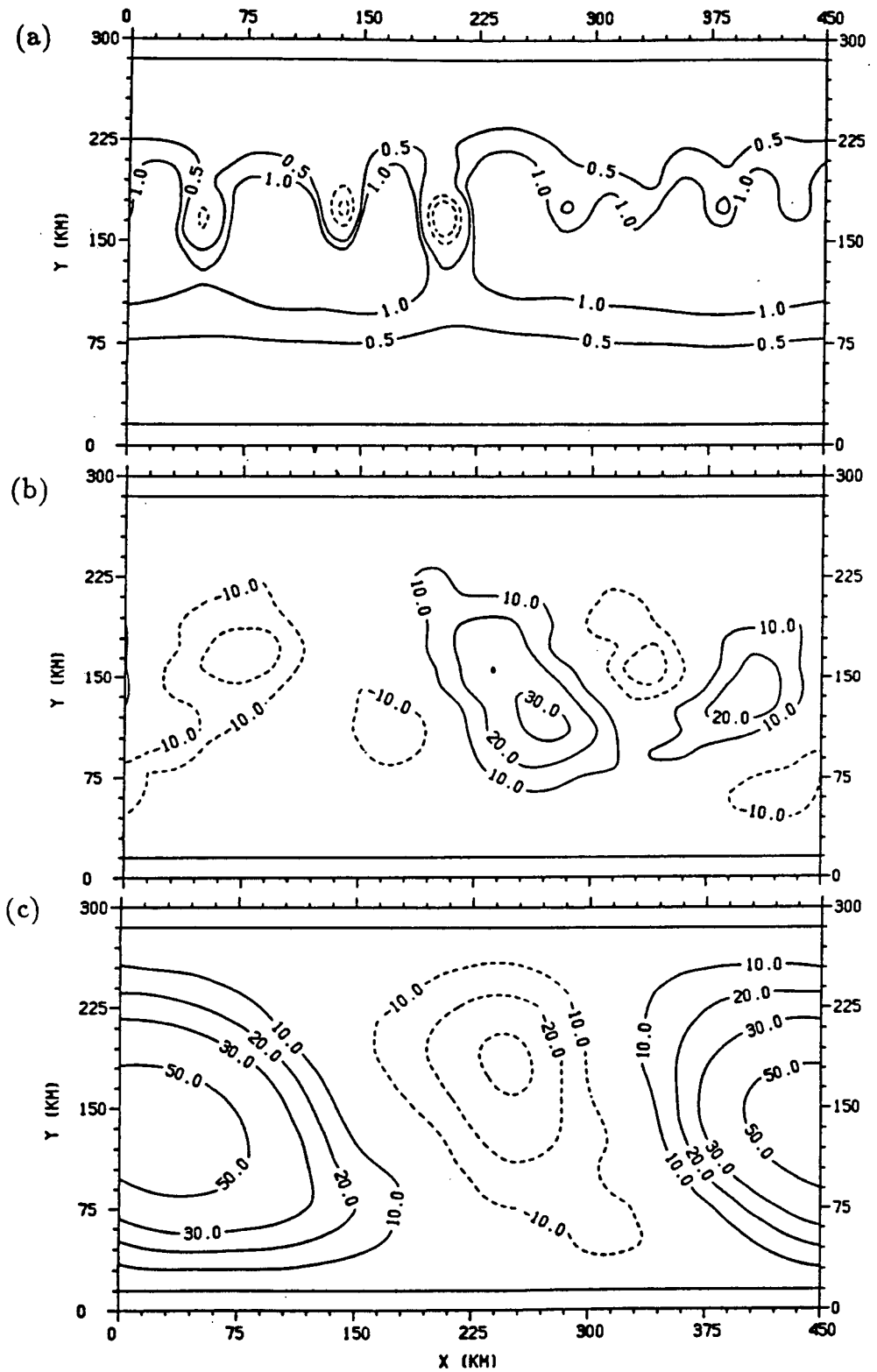

Figure 4.7: The 'Real Ocean': barotropic streamfunction (contour labels in sverdrups) at (a) day 10, (b) day 30 and (c) day 70. Solid and dashed contours correspond to anticyclonic and cyclonic circulations respectively.

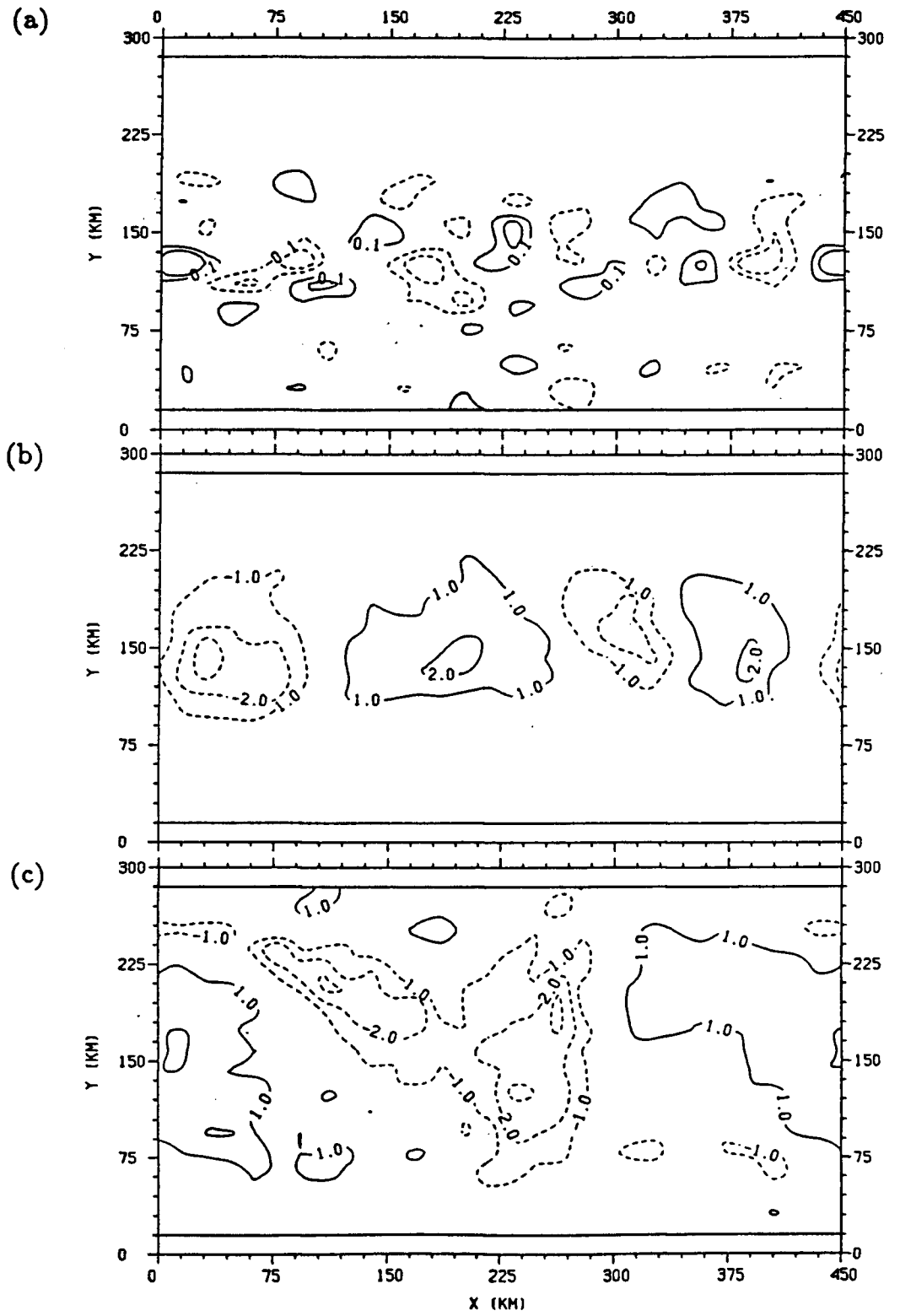

Figure 4.8: The 'Real Ocean': temperature anomaly defined by equation (4.1) and (4.2) (contour labels in °C) at (a) day 10, (b) day 30 and (c) day 70.

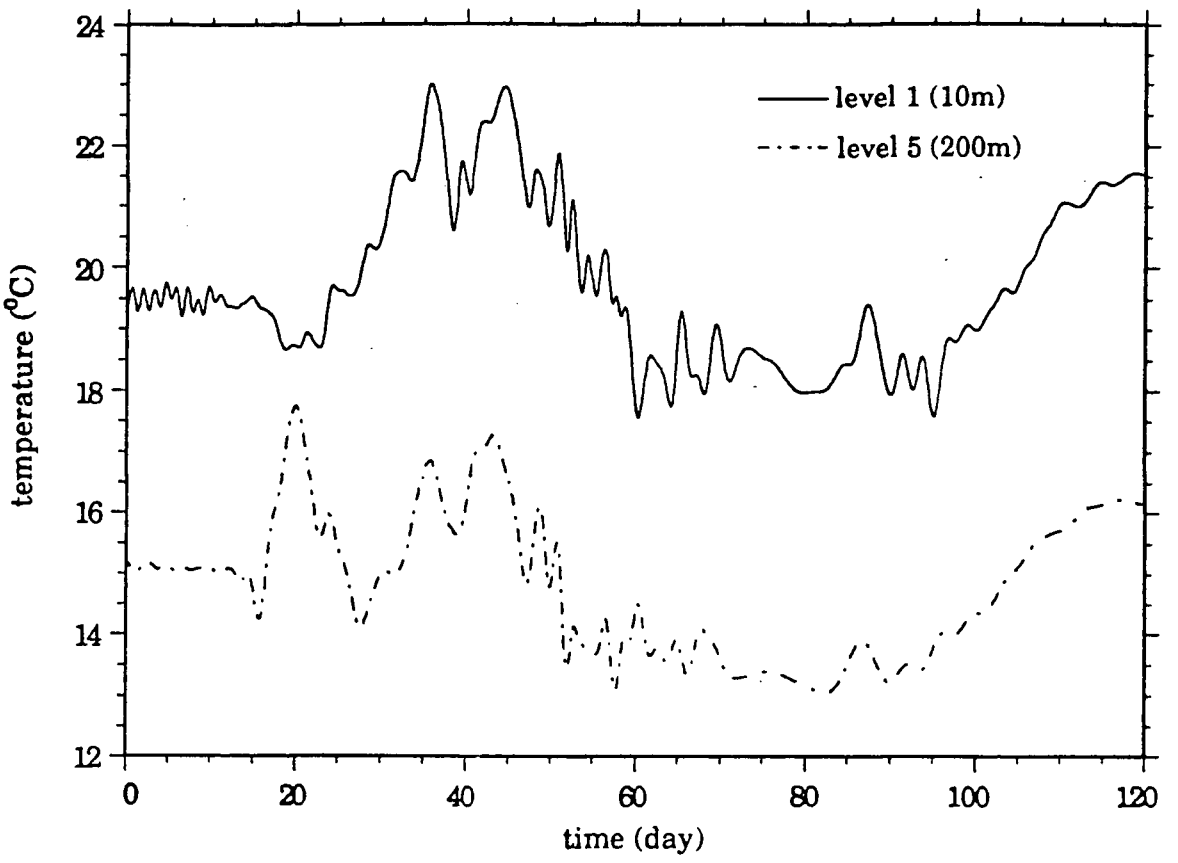

Figure 4.9: The 'Real Ocean': time series of the level 1 (10 m) and level 5 (200 m) temperature field (in °C) at the fixed location ($i = 15, j = 10$).

the temperature field to the perturbation, particularly in the deeper level. The only apparent feature is a series of inertial oscillations left over from the diagnostic spin-up (compare with Fig. 4.1).

The growth of the instabilities is evident soon after day 10, however the response in the temperature field is quite different in both levels. Between days 15 and 30, the temperature at level 5 undergoes a dramatic fluctuation of about 3.5°C. Compared to level 5, the fluctuation at level 1 during this same time period has a much weaker amplitude (< 1°C) and is 180° out of phase. The origins of this fluctuation will be described

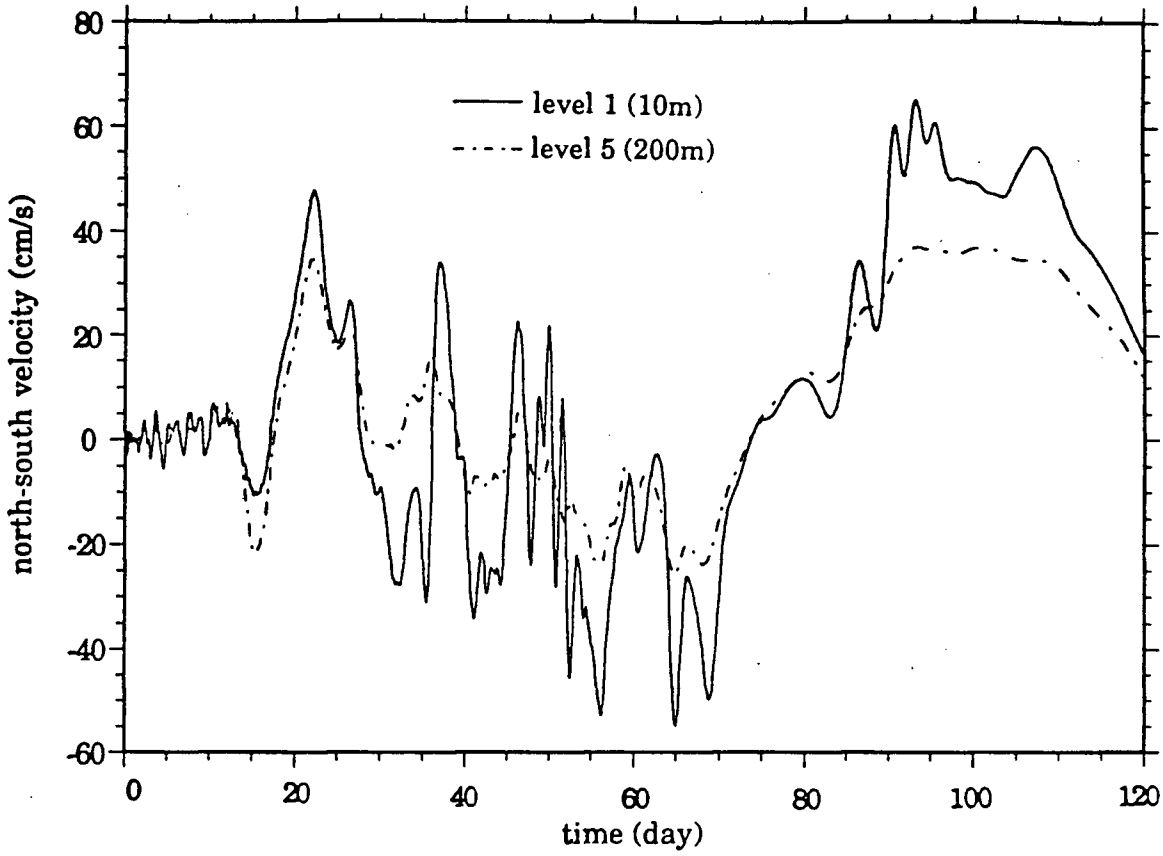

Figure 4.10: The 'Real Ocean': time series of the level 1 (10 m) and level 5 (200 m) N-S velocity field (in cm/s) at the fixed location ($i = 15, j = 10$).

shortly. Following this 15 day period, the two fields begin to exhibit qualitatively the same behaviour. Another prominent feature of this time series is a distinctive long time scale of about 80 days appearing in both levels. Similar behaviour is exhibited in the N-S velocity component time series although the features are considerably more noisy (Fig. 4.10). In particular, the N-S velocity at both levels has a transient character very similar to that of the level 5 temperature.

The long time scale ($\approx$80 days) observed in the time series figures shows up as

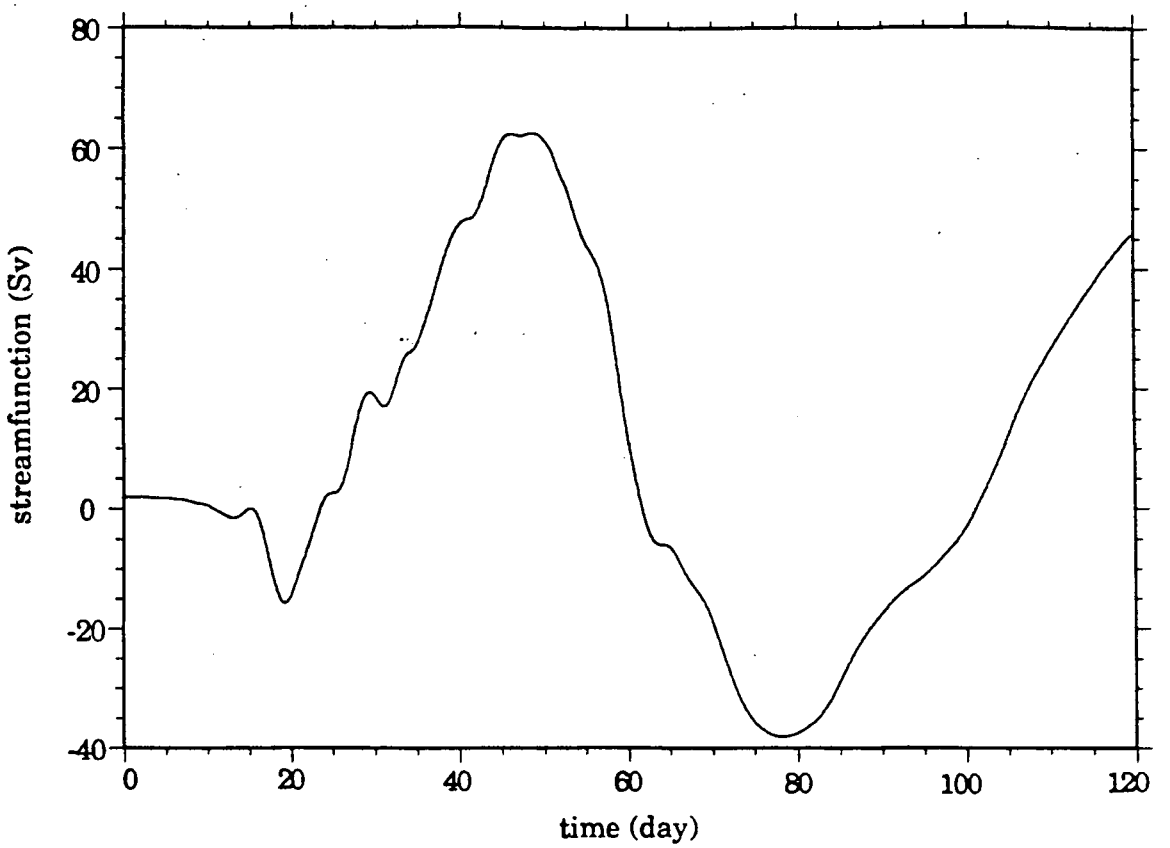

Figure 4.11: The 'Real Ocean': time series of the barotropic streamfunction (in Sv) at the fixed location ($i = 15, j = 10$).

the dominant time scale in the barotropic streamfunction (Fig. 4.11). It can be regarded, therefore, as a barotropic time scale associated with the period of a westward propagating Rossby wave. Notice that the phase speed required for a Rossby wave of wavenumber 1 to travel the length of the channel in 80 days is $-6.5\,\mathrm{cm/s}$ which is consistent with the phase speed (-5 to $-7\,\mathrm{cm/s}$) estimated earlier from a series of contour plots.

The final time series is of the vertical velocity and is shown in Figure 4.12. The most striking feature here is a well-defined oscillation at both levels due to the passage of an

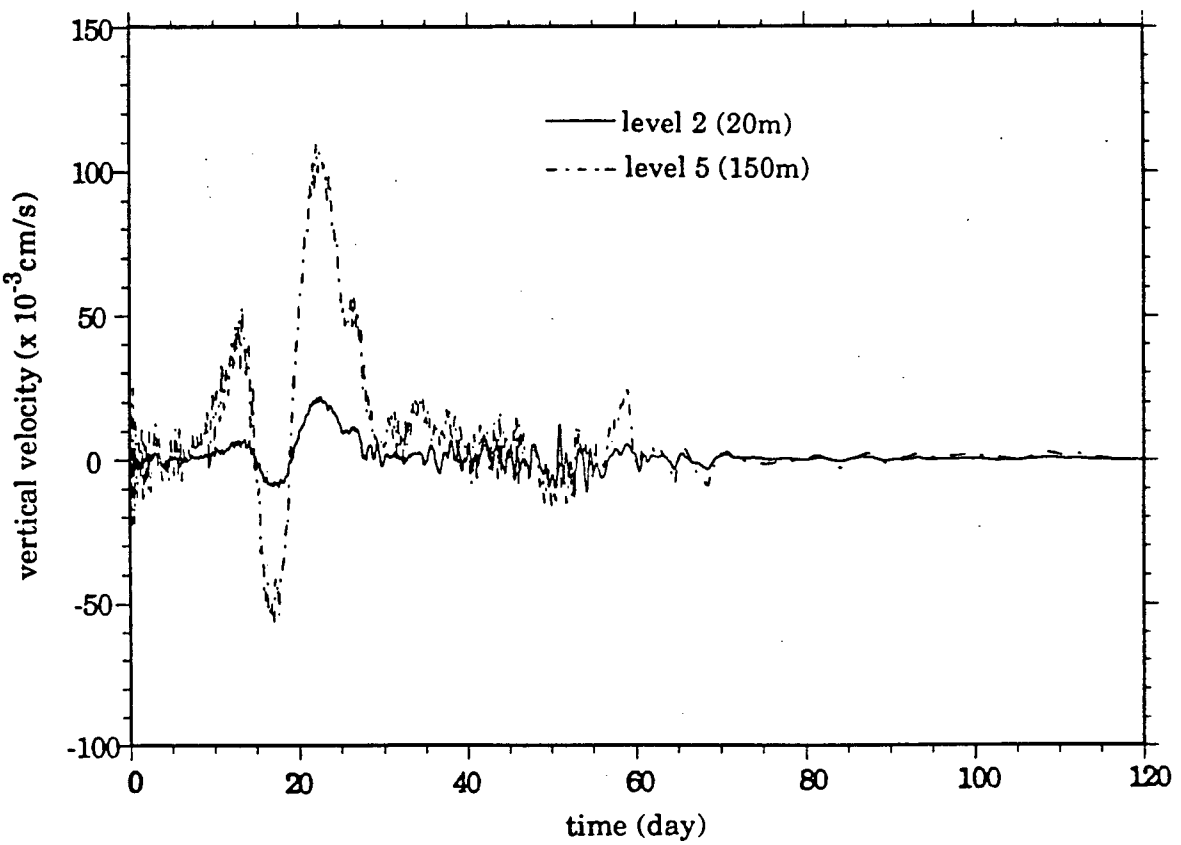

Figure 4.12: The 'Real Ocean': time series of the level 2 (20 m) and level 5 (150 m) vertical velocity (in 10^{-3} cm/s) at the fixed location ($i = 15, j = 10$).

unstable wave between days 10 and 30. The maximum amplitude of the oscillation at level 5 (150 m) is about 5 times larger than at level 2 (20 m). Following this event, the vertical velocity fluctuates noisily about its zero mean value until day 70 when it dies out altogether due to the strong barotropic nature of the model at this time.

There is a strong correlation between the upwelling/downwelling phases associated with the oscillation and the large cooling/warming fluctuations in the temperature field (compare Figs. 4.9 and 4.12 between days 10 and 30). The importance of vertical advection during this period, therefore, is clear – the warming (cooling) cycle corresponding

to warmer surface (cooler deeper) water being advected to the deeper (upper) layers.

4.2 Sensitivity to the Nudging Coefficient

A simple 'trial and error' approach is used to determine the optimal choice for the constant nudging coefficient C in (3.1). The 'optimal' C, in this case, refers to the one which offers the greatest error reduction as measured through the time evolution of the RMS error (calculated daily) given by (3.2). Comparison plots of the actual flow fields will not be presented until the next section.

Four particular values of the nudging coefficient are considered here: (1) $C = 0$; (2) $C = (4\,\text{days})^{-1}$; (3) $C = (0.5\,\text{days})^{-1}$; and (4) $C = \infty$. Case (1) is analogous to the simulation model, Run A, in which no SST data are assimilated. The time evolution of the RMS error (RMS_k^A) for this run is a measure of the model departure from 'reality' or, alternatively, of its unpredictability. It provides a standard reference error to which the RMS errors (RMS_k^B) for the assimilation experiments can be compared. Cases (2) and (3) correspond to relaxing the model surface temperature field to 'observations' on a time scale of 4 days and half a day respectively. The final case (4) refers to the direct SST data insertion experiment already mentioned in §3.2.

Figure 4.13(a), (b) and (c) shows the time evolution of the temperature RMS errors for levels 1 (10 m), 5 (200 m) and 10 (2200 m) respectively. The solid curve corresponds to the standard error RMS_k^A, $(k = 1, 5, 10)$, and the series of dotted and dashed curves to the RMS_k^B, $(k = 1, 5, 10)$, error for the various assimilation experiments. For consistency, the same vertical scale has been used at each level. Note also that the term model SST and the level 1 temperature are used interchangeably here.

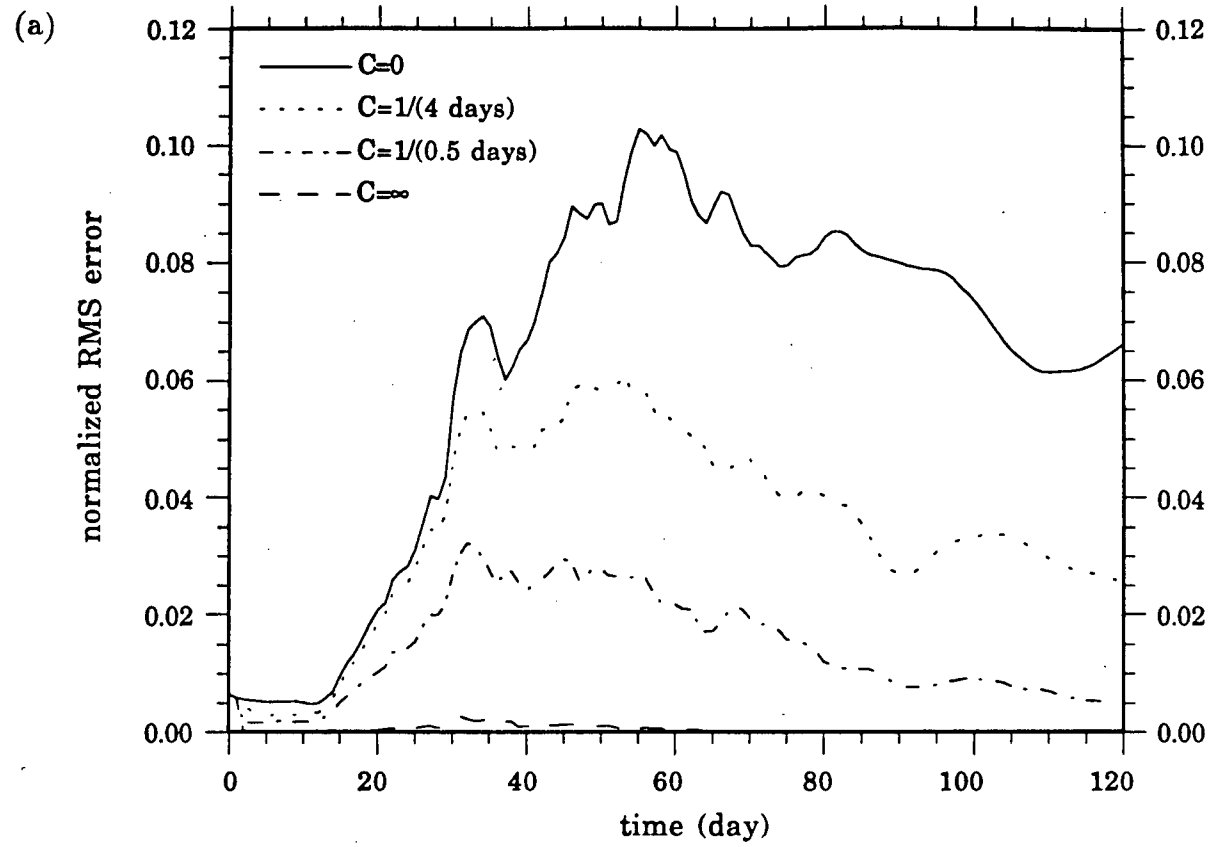
(a)
C=0
C=1/(4 days)
C=1/(0.5 days)
C=∞
normalized RMS error
time (day)
0.00
0.02
0.04
0.06
0.08
0.10
0.12
0
20
40
60
80
100
120

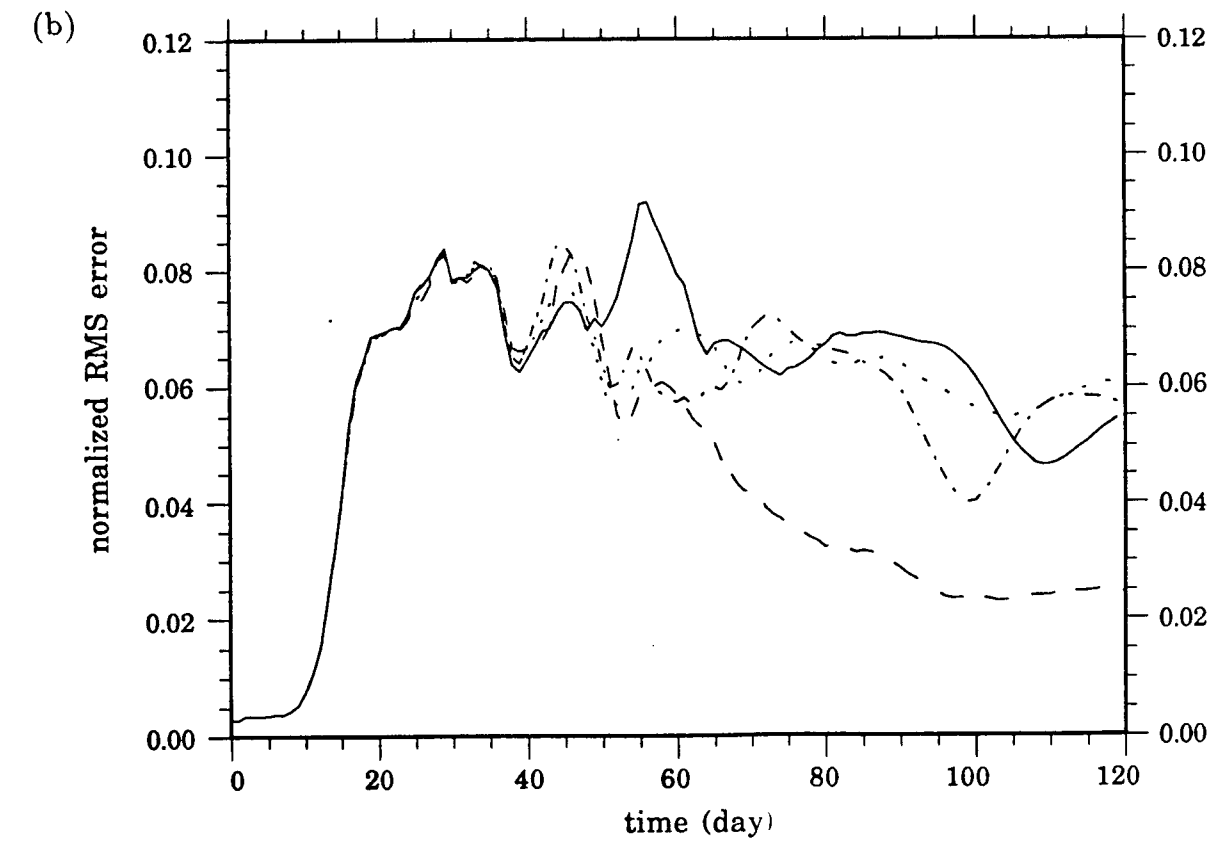
(b)
normalized RMS error
time (day)
0.00
0.02
0.04
0.06
0.08
0.10
0.12
0
20
40
60
80
100
120

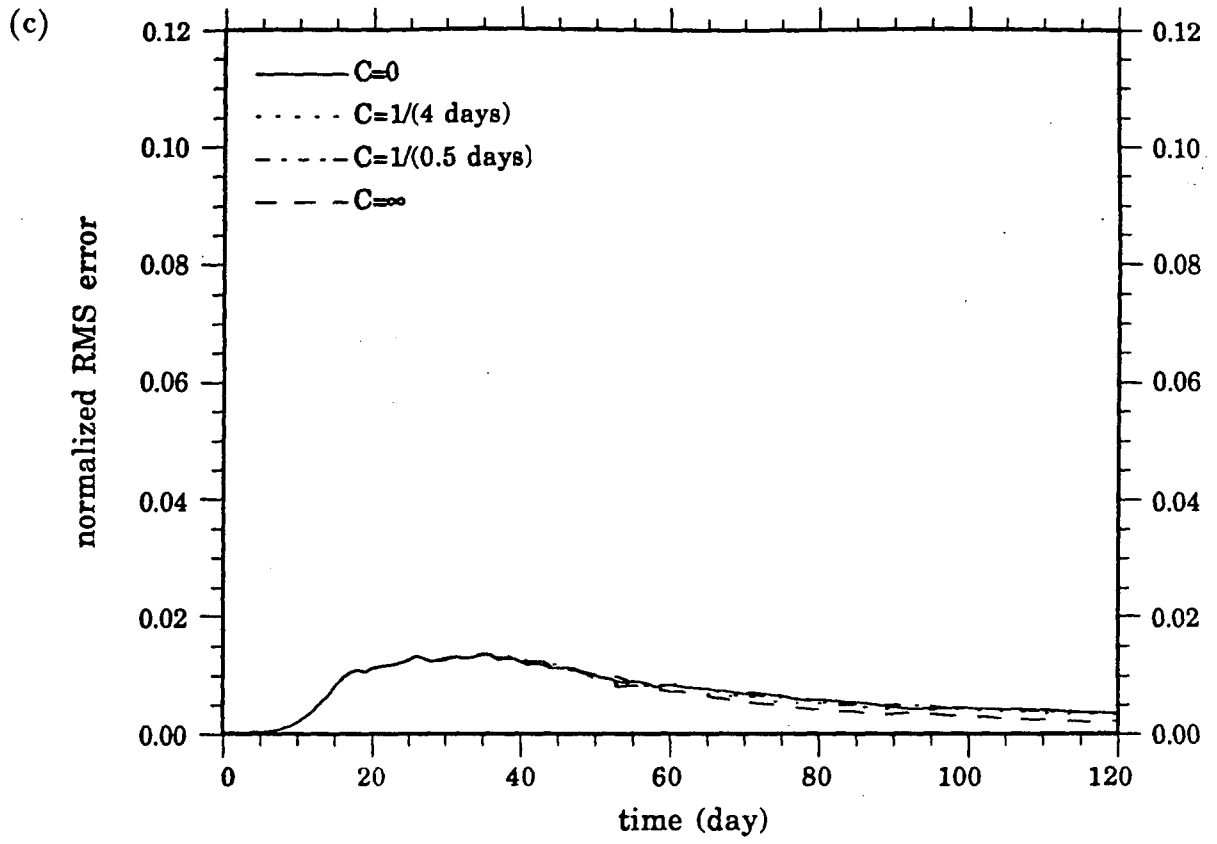

Figure 4.13: The time evolution of the (normalized) temperature RMS error (in °C) at (a) level 1 (10 m), (b) level 5 (200 m) and (c) level 10 (2200 m) for different values of the nudging coefficient (see legend).

First consider the standard error curves ($C = 0$). Only after ten days of integration does the model (Run A) temperature begin to deviate from that of the reference ocean (Run R). This notable increase in the error growth rate is observed at all levels and coincides precisely with the period of rapid unstable wave development as discussed previously in §3.1. The level 1 temperature error (RMS_1^A) exhibits an increasing trend for the next 45 days, attaining a maximum around day 55 and then following a slight decreasing trend thereafter (Fig. 4.13(a)). A similar behaviour is observed in the level 5 temperature error (RMS_5^A) (Fig. 4.13 (b)). One noticeable difference, however, is that the error growth rate between days 10 and 30 is considerably faster at this level. The

magnitude of the temperature error at level 10 (RMS_{10}^{A}) on the other hand, is small in comparison to both RMS_{1}^{A} and RMS_{5}^{A} (Fig. 4.13(c)).

Now consider the temperature assimilation error curves (RMS_{k}^{B}). The RMS_{1}^{B} errors are shown in Figure 4.13(a) to illustrate the rates at which SST data are assimilated into the top level of the model in the different experiments. These errors, therefore, are controlled errors which can be adjusted according to the specific choice of the nudging coefficient in (3.1). The dotted curve corresponds to $C = (4\,\text{days})^{-1}$ and the dashed-dotted curve to $C = (0.5\,\text{days})^{-1}$. The dashed curve which corresponds to direct SST insertion ($C = \infty$) does not coincide exactly with the bottom axis (i.e., zero RMS error) because there is a slight error introduced from the fact that SST 'observations' have been linearly interpolated in time to form a time continuous data-set.

There are two main features to take note of from the RMS_{5}^{B} errors in Figure 4.13(b). First, the curves begin to depart from each other after about 30 days in all experiments, indicating that this is the time scale required for the assimilated SST to spread to a depth of 200 m. Vertical advection is the most important physical process responsible for the effective spreading of this surface information. In some regions, however, convective mixing is also significant. These processes are a key aspect of the assimilation and will be discussed in more detail later in the chapter.

The second distinctive feature emerging from this plot is the different behaviour of the three RMS_{5}^{B} curves. Only the direct SST insertion experiment ($C = \infty$) has a temperature RMS_{5}^{B} curve showing substantial error reduction. In contrast, when the assimilation is performed on a relaxation time scale of 4 days and 0.5 days there is no clear improvement in the temperature at this depth. In both cases the RMS_{5}^{B} error appears to oscillate to some degree about the standard RMS_{5}^{A} error. By the end of the run (day 120), the assimilation runs actually indicate a slight worsening of the level 5 temperature. In the deepest level (2200 m), the RMS_{10}^{B} errors in the temperature

show very little difference from the standard RMS_{10}^{A} error (Fig. 4.13(c)). It takes over one month before assimilation has any effect on the temperature, with again the error reduction being greatest for the experiment with $C = \infty$.

The effect of the assimilation on the velocity field is shown in Figure 4.14(a,b,c) and 4.15(a,b,c) for the N-S and E-W components respectively. It is clear from both figures that the direct SST insertion offers the greatest improvement at all levels. A significant error reduction is particularly noticeable in the N-S component, although the E-W component also exhibits a substantial improvement. In the other two experiments, the SST assimilation was unable to drive the model flow field back toward that of the reference ocean.

The preceding results for the RMS_{k}^{B} velocity errors are not surprising considering that the only significant improvement in the temperature fields was also for the assimilation experiment with $C = \infty$. The density and velocity fields are so intimately related through a quasi-geostrophic balance that an improvement in the temperature (i.e., density) field readily manifests itself as an improvement in the (baroclinic) flow field following geostrophic adjustment. During the first month the SST assimilation is unable to control the rapid divergence of the model from the reference ocean, with the largest error growth occuring in the uppermost level where the intensity of the flow is strongest. Only after the SST information is advected to depth, do the model fields begin to exhibit a steady error reduction. This emphasises how important it is for the model flow dynamics to possess the physical mechanisms which can effectively transfer the assimilated surface information downwards.

(a)

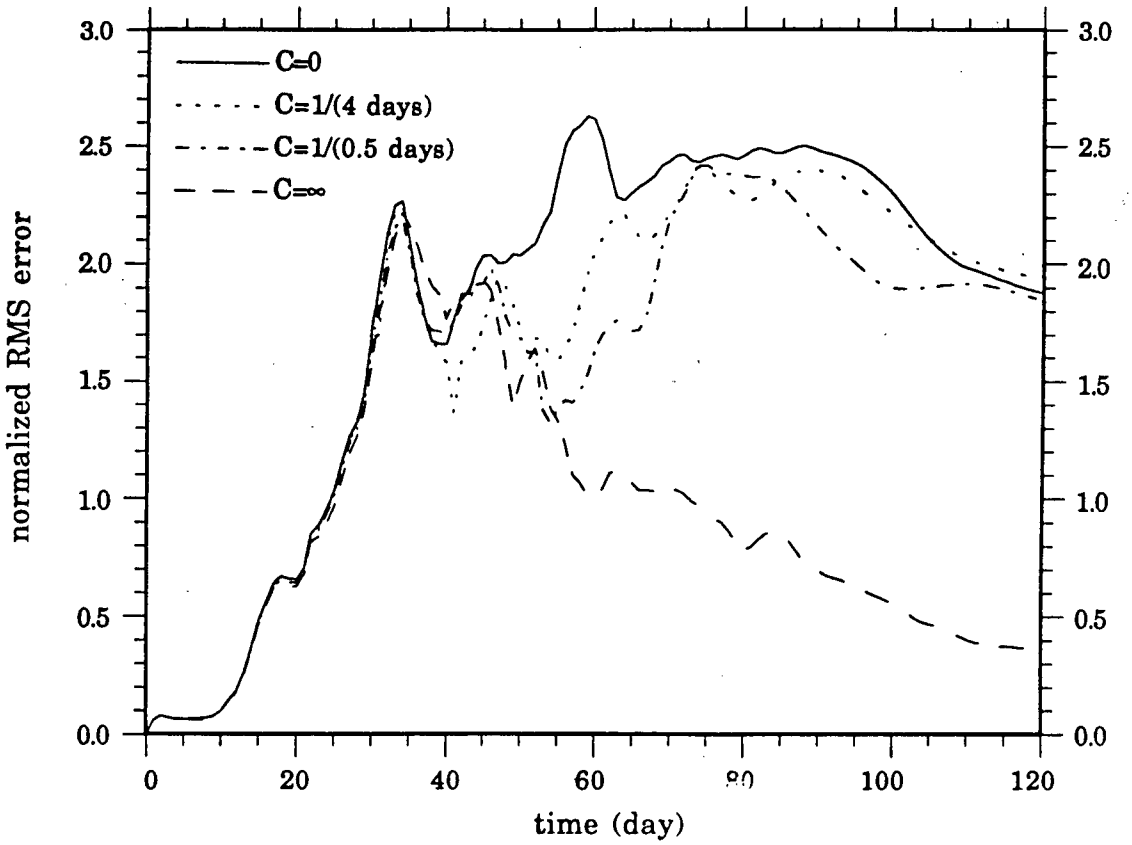
C=0
C=1/(4 days)
C=1/(0.5 days)
C=∞
normalized RMS error
time (day)
0.0
0.5
1.0
1.5
2.0
2.5
3.0
0
20
40
60
80
100
120

(b)

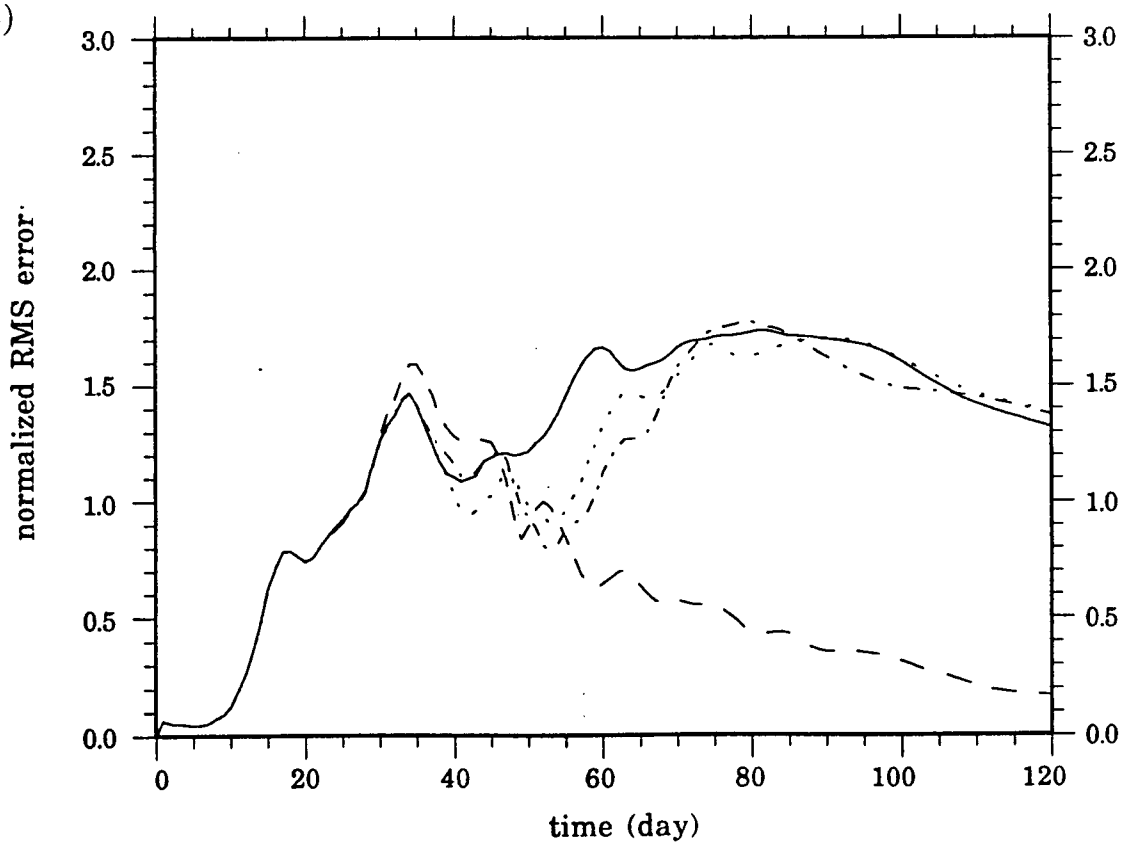
normalized RMS error
time (day)
0.0
0.5
1.0
1.5
2.0
2.5
3.0
0
20
40
60
80
100
120

(c)

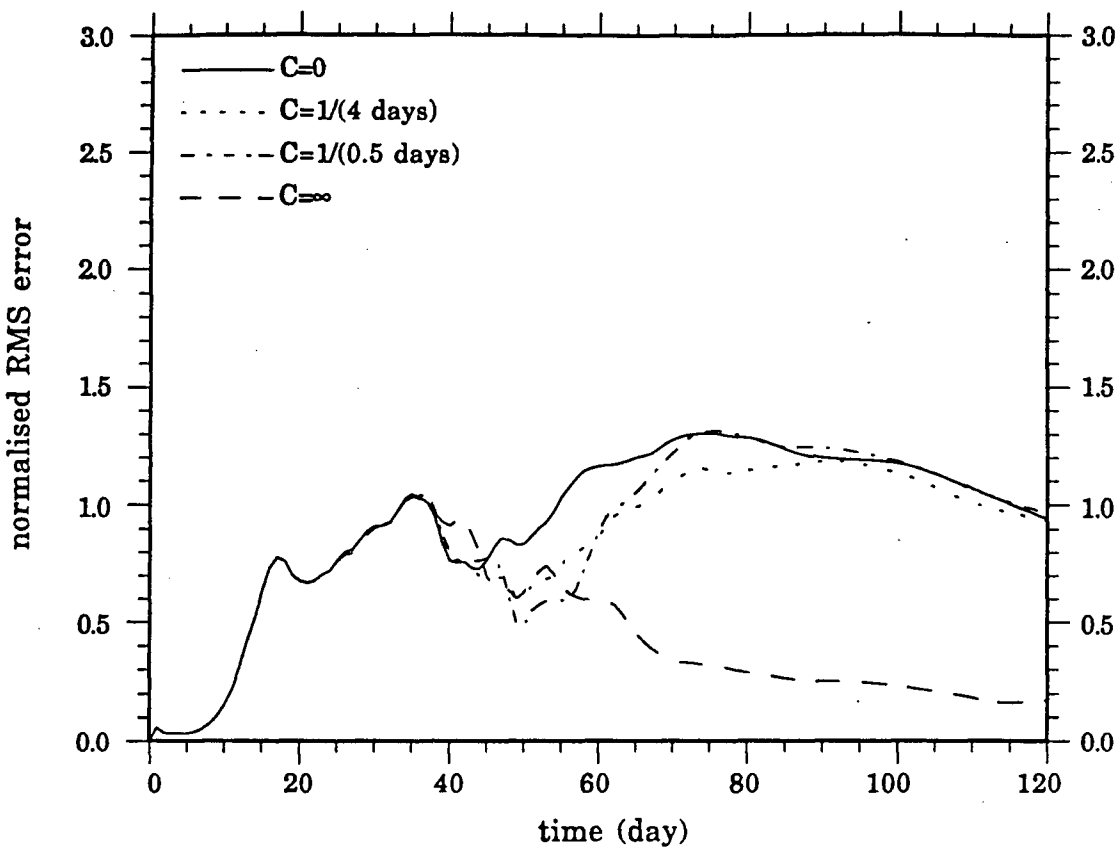

Figure 4.14: The time evolution of the (normalized) N-S velocity component RMS error (in cm/s) at (a) level 1 (10 m), (b) level 5 (200 m) and (c) level 10 (2200 m) for different values of the nudging coefficient (see legend).

(a)

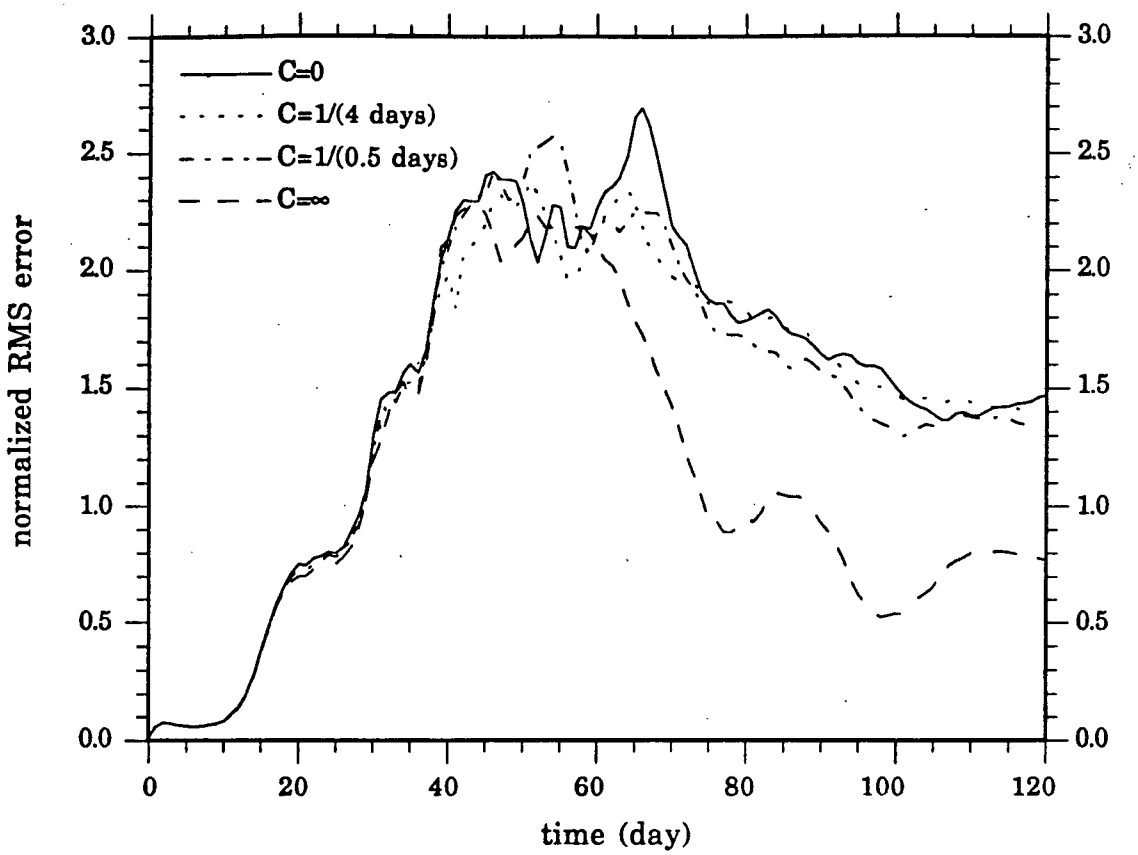
C=0
C=1/(4 days)
C=1/(0.5 days)
C=∞
normalized RMS error
time (day)
0.0
0.5
1.0
1.5
2.0
2.5
3.0
0
20
40
60
80
100
120

(b)

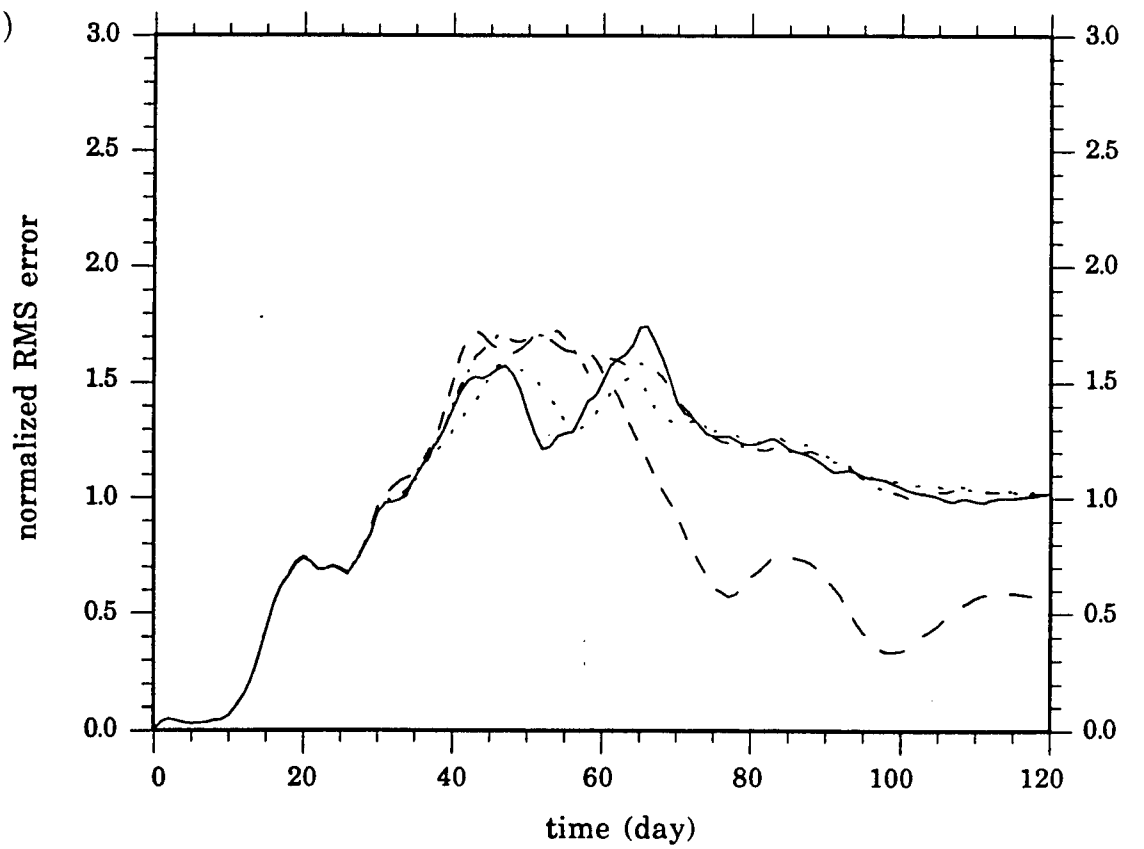
normalized RMS error
time (day)
0.0
0.5
1.0
1.5
2.0
2.5
3.0
0
20
40
60
80
100
120

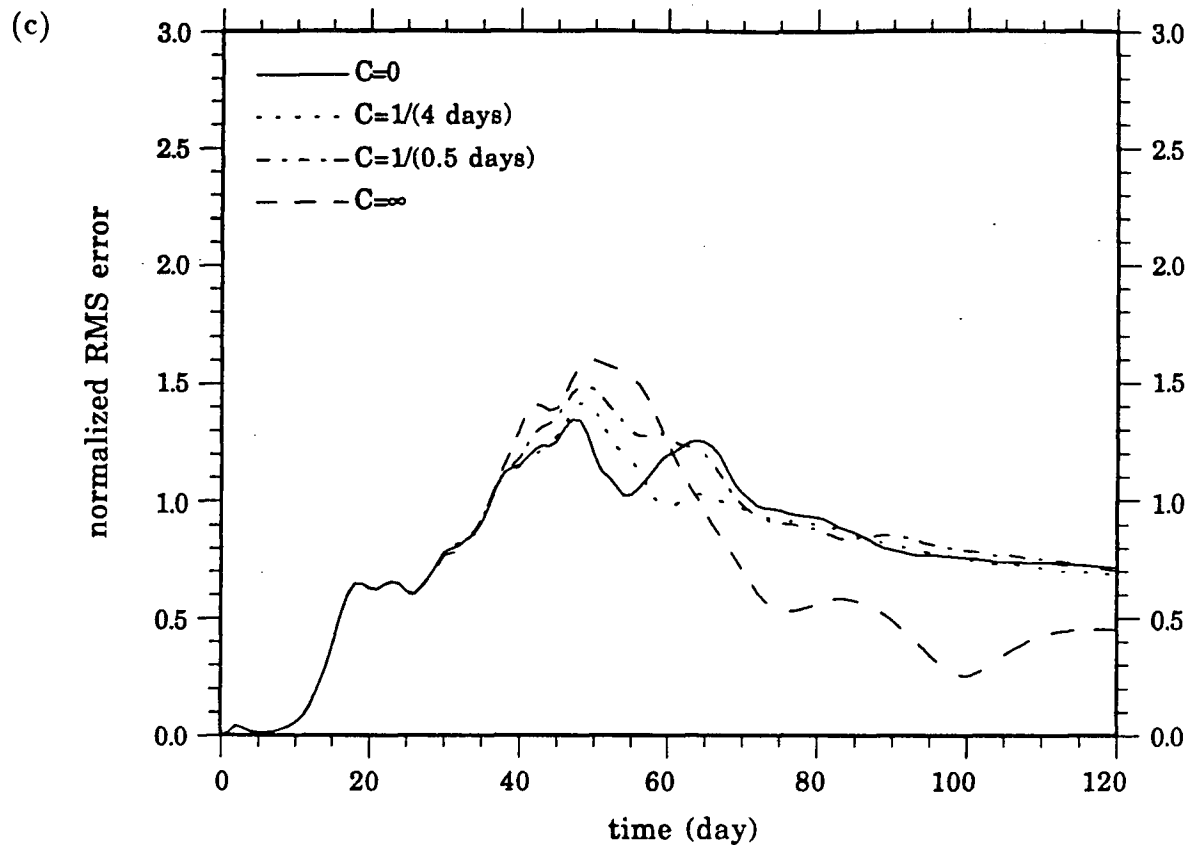

Figure 4.15: The time evolution of the (normalized) E-W velocity component RMS error (in cm/s) at (a) level 1 (10 m), (b) level 5 (200 m) and (c) level 10 (2200 m) for different values of the nudging coefficient (see legend).

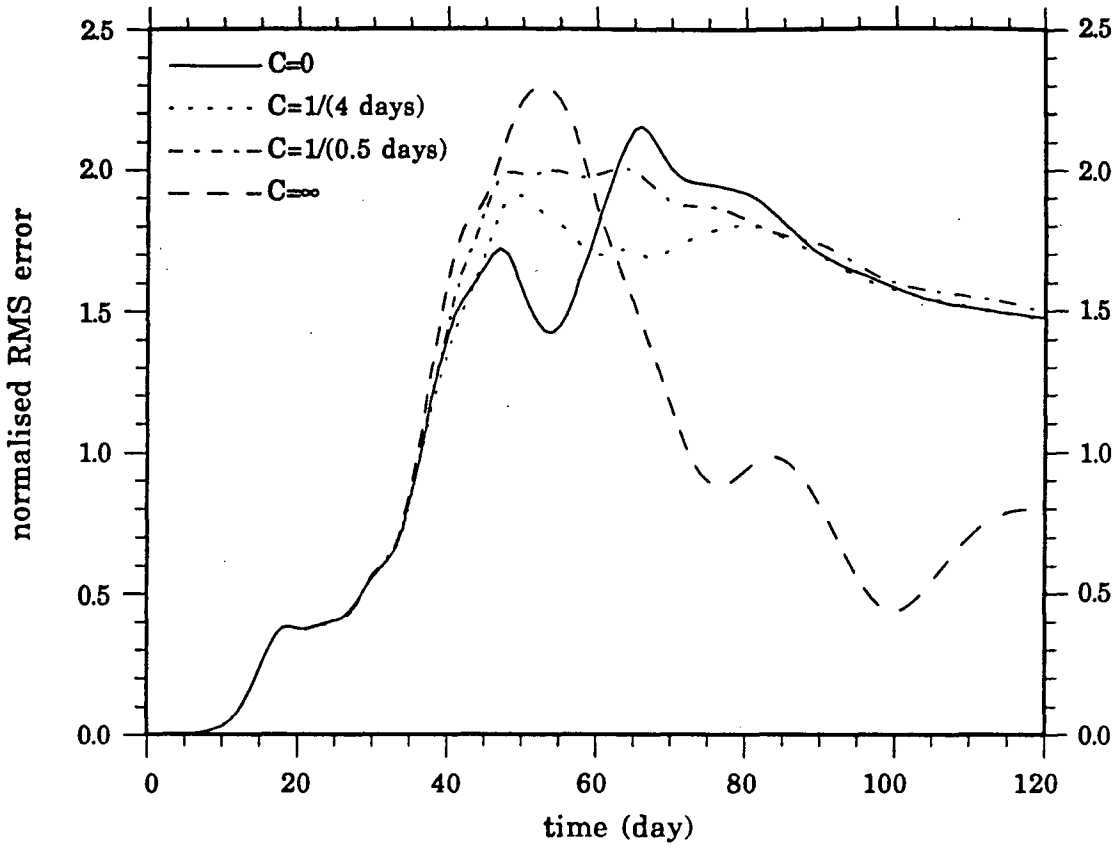

Figure 4.16: The time evolution of the (normalized) barotropic streamfunction RMS error (in Sv) for different values of the nudging coefficient (see legend).

The barotropic streamfunction RMS errors in Figure 4.16 illustrate the response of the barotropic mode to the assimilation of (near) surface baroclinic information (i.e., SST). The most striking feature here is the dramatic decrease in the assimilation RMS^B error with respect to the RMS^A error but, in accordance with previous results, only for the direct insertion experiment. This improvement follows a period (during the second month) in which the barotropic field is worsened by the assimilation. It is unclear what causes this extreme behaviour but it may be an artifact of the complicated nonlinear modal interactions. These interactions and the associated 'barotropication' are inevitably responsible for spreading the assimilated baroclinic information to the barotropic mode (refer to the right hand side of equation (2.25)). Additional forcing

from the baroclinic to the barotropic mode through the joint effect of baroclinicity and relief (JEBAR) effects (Holland, 1973) is excluded due to the absence of bottom topography (i.e., H is constant).

The preceding results indicate unequivocally that SST assimilation performed using the nudging technique is most effective when the nudging coefficient is taken to be infinite, that is, when SST data are inserted directly into the model. It should also be pointed out that there are two important time scales occurring here, both of which ultimately govern the success of the assimilation. First and foremost is the vertical advection time scale, required to distribute the assimilated surface baroclinic information to the deeper levels. The experiments of §4.4 will make this point clear. Second, because the model response in the (unforced) spin-down experiments conducted here is eventually strongly barotropic, there is also an important non-linear mode interaction time scale, over which the cascading of energy from the higher baroclinic modes to barotropic mode takes place.

4.3 Comparison of the Flow Fields

In this section we make use of instantaneous plots and time series of the various data fields to examine and compare the actual flow fields of Run R, A and B. Comparisons are made for the direct SST insertion experiment only, as this experiment showed the greatest convergence toward the reference ocean.

The improvement in the model is clearly seen in Figure 4.17(a), (b) and (c), showing the upper level N-S velocity contours at the end of the run (day 120) for Runs R, A and B respectively. The assimilation Run B (lower panel) has completely restored the proper phase of the large-scale planetary waves while, in contrast, Run A (middle panel) exhibits along-channel planetary wave propagation which is about 180° out of phase

with Run R (upper panel). The wave amplitudes in Run B, however, are slightly smaller than Run R.

The barotropic streamfunction patterns of Run B in Figure 4.18 show a similar improvement. The regions of anticyclonic (solid contours) and cyclonic (dashed contours) eddies correspond to the crests and troughs of the planetary waves respectively. Although the rotational sense of these eddies has been corrected by the assimilation, the actual eddy (barotropic) transports are quite different. The transport is overestimated (by ≈ 30 Sv) in the cyclonic eddy and underestimated (by ≈ 30 Sv) in the anticylonic eddy. Nevertheless, the extent of the improvement in the barotropic component of the flow is quite remarkable considering that no prior knowledge of it assumed from the 'real ocean'. The assimilation model has successfully reconstructed the major features of the 'real ocean' barotropic circulation using only SST 'observations' (i.e., (near) surface baroclinic information).

We now examine the model temperature fields and, in doing so, point out an important, yet potentially harmful, feature of the assimilation process. In Figure 4.19(a) and (b), the top level, or 'surface', temperature field at day 120 is shown for Runs R and A respectively. The top level temperature field for the direct SST insertion experiment (Run B) is identical to Run R and therefore not shown. The presence of warm and cold eddies is evident in both temperature fields. In Run R (and Run B), a large (anticyclonic) warm eddy lies central in the channel and is flanked on its western side by a smaller (cyclonic) cold eddy which begins to reappear at the eastward end due to the periodicity of the channel (compare with Figure 4.18(a)) . The surface temperature field in Run A, on the other hand, is dominated by a cold eddy although a smaller warmer eddy is also observed (compare with Figure 4.18(b)). These warm and cold eddies are most clearly visible in Figure 4.20(a) and (b), showing the temperature

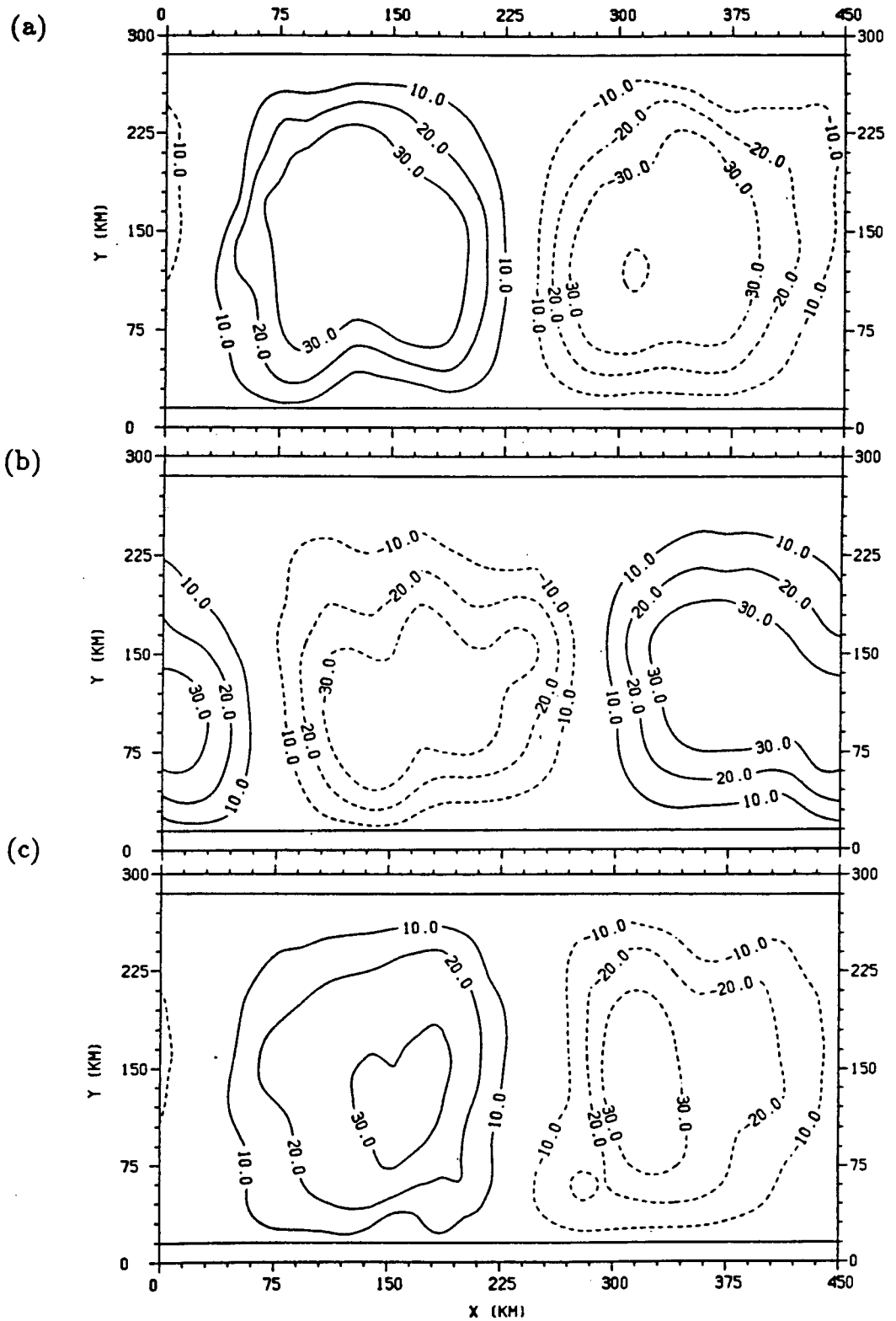

Figure 4.17: Comparison on day 120 of the level 1 (10 m) north-south velocity component (contour labels in cm/s) between (a) Run R, (b) Run A and (c) Run B.

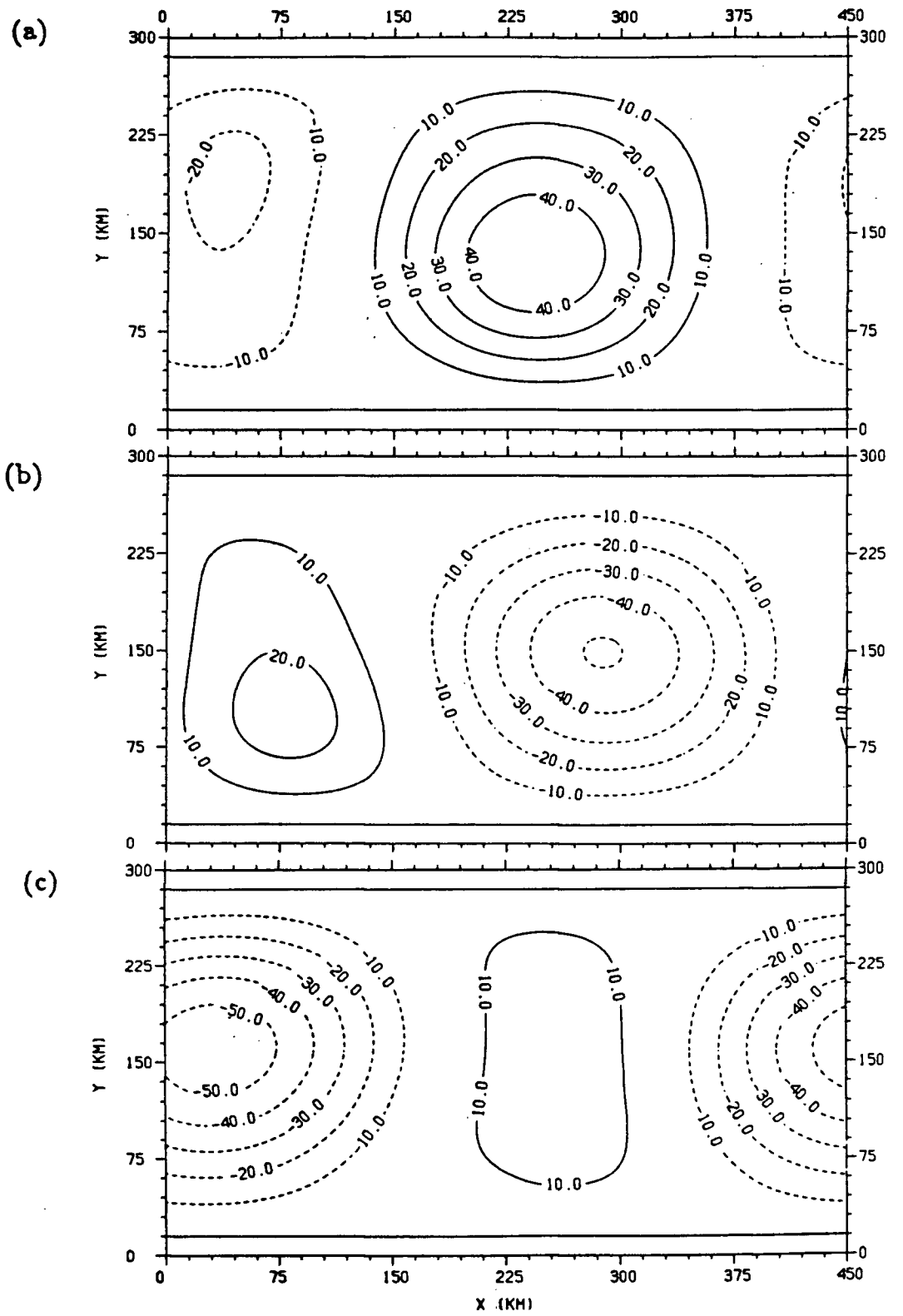

Figure 4.18: Comparison on day 120 of the barotropic streamfunction (contour labels in Sv) between (a) Run R, (b) Run A and (c) Run B. Solid and dashed contours correspond to anticyclonic and cyclonic circulations respectively.

anomalies calculated from (3.2).

The temperature field at level 3 (70 m) is shown in Figure 4.21. The distinctive eddy features observed at the surface in both Run R and A show up clearly at level 3 (Fig. 4.21(a) and (b) respectively) and although not shown, are prominent down to a depth of about 500 m. Figure 4.21(c) shows the extent to which the level 3 temperature field has been corrected by the assimilation (Run B). While Run B shows an obvious improvement over Run A, it still is unable to capture the proper horizontal structure of the eddies. In particular, the well-defined warm eddy in Run R is poorly resolved and about 2°C colder in Run B. Also, note the large patch of cold water at the end of the channel in comparison to a much smaller cold region in Run R. Thus, in general, the ocean of the assimilation Run B appears considerably colder than Run R (and Run A) and possesses much weaker horizontal temperature gradients.

The apparent smoothing of horizontal temperature gradients is best seen by comparing the temperature anomalies of Figure 4.22. The anomalies of Run B (lower panel), although once again exhibiting the correct phase, are substantially weaker than those of Run R (upper panel) and A (middle panel). The cold anomaly is particularly weak. These features can be explained by the effects of convective mixing which occur when colder (denser) near surface temperature data are assimilated into a region with warmer (lighter) subsurface water. This is assuming that the ocean's upper level density field is predominantly temperature dependent which is indeed the case here. When the numerical model encounters an unstable water column, it immediately mixes the water column until stability is restored. In the assimilation model, this convective adjustment can take place over the top three to four levels (i.e., down to 150 m).

Following this rapid mixing process, the new colder subsurface waters are advected by the intense jet to other regions of the channel as well as advected vertically by strong

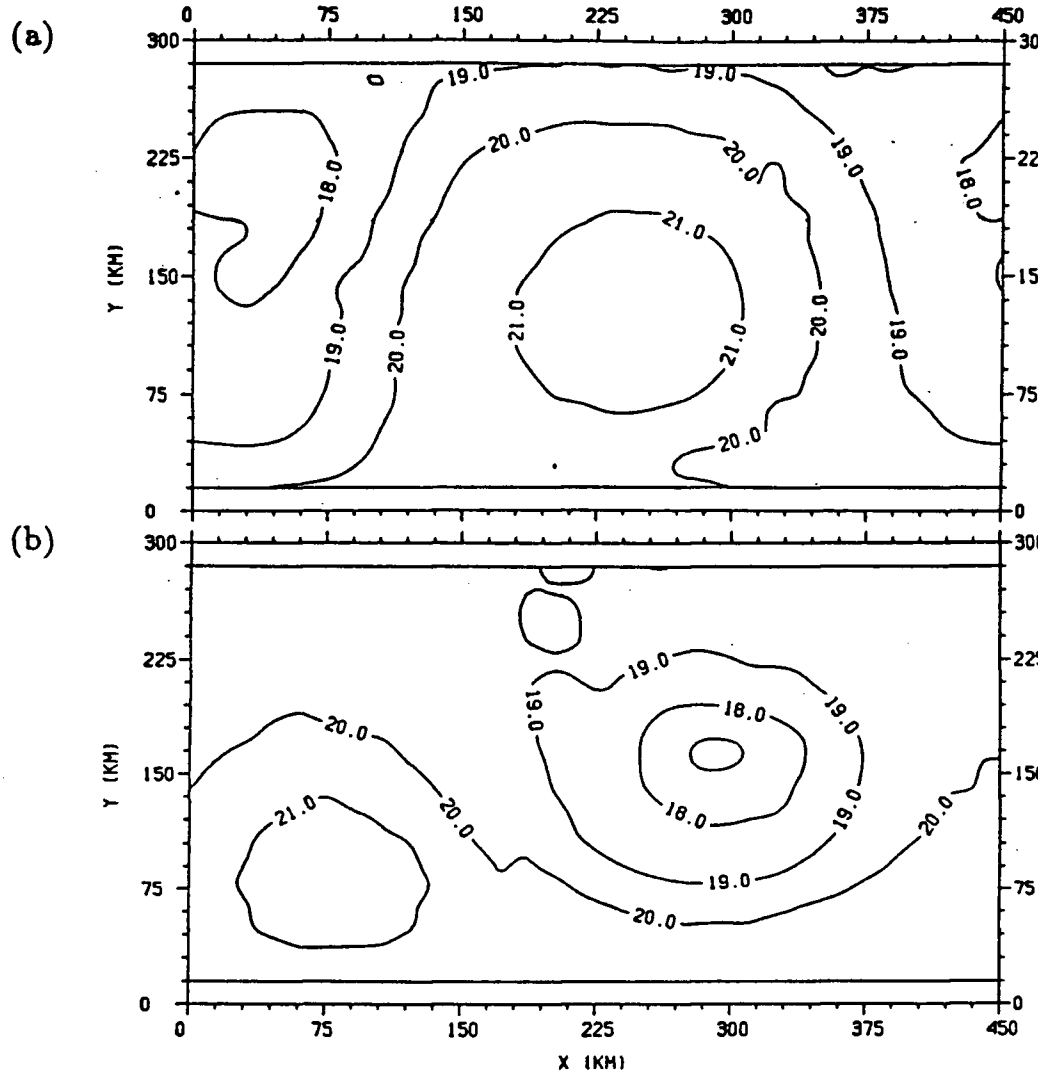

Figure 4.19: Comparison on day 120 of the level 1 (10 m) temperature (contour labels in °C) between (a) Run R (and Run B), and (b) Run A.

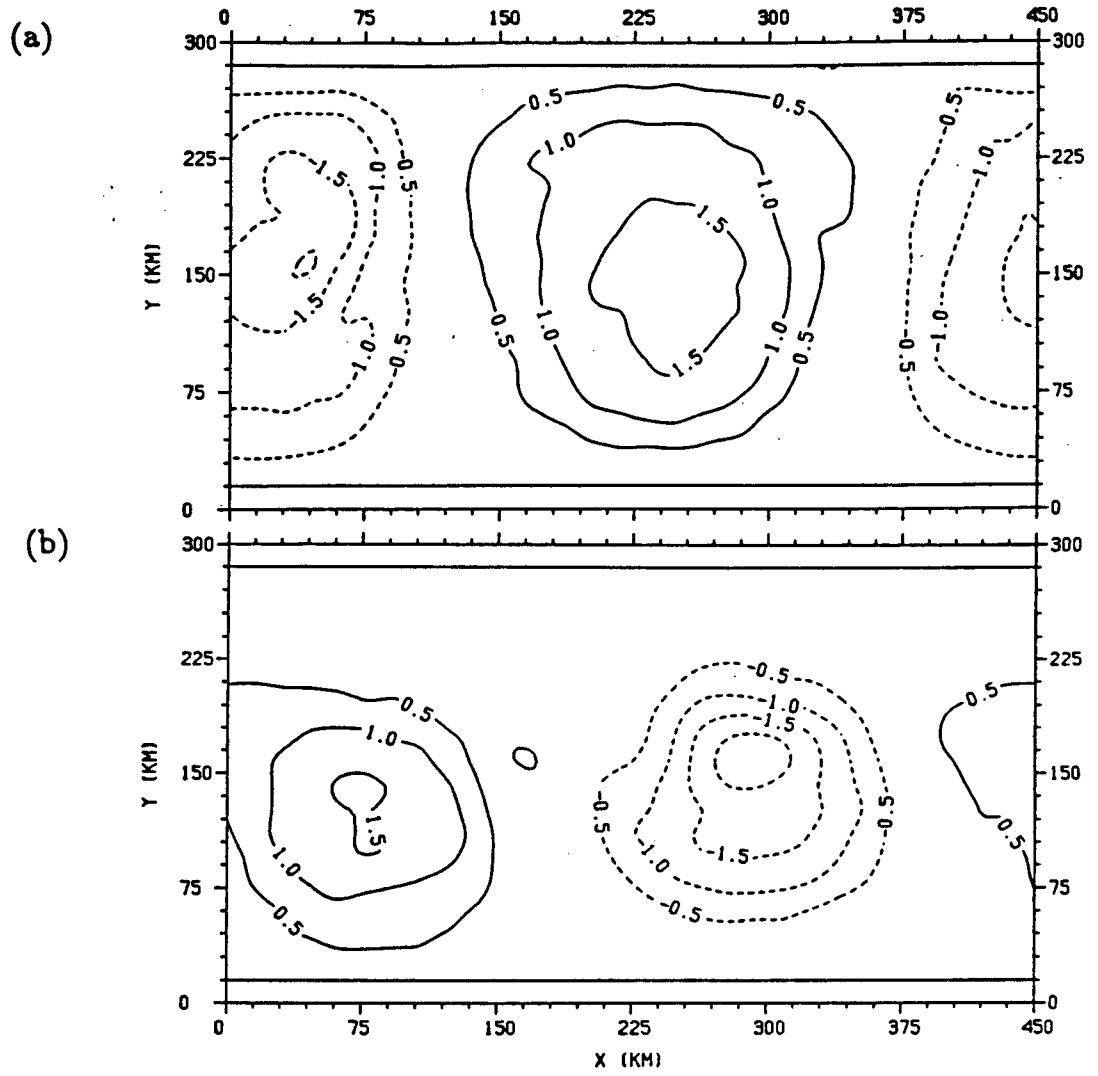

Figure 4.20: Comparison on day 120 of the level 1 (10 m) temperature anomaly (contour labels in °C) between (a) Run R (and Run B), and (b) Run A.

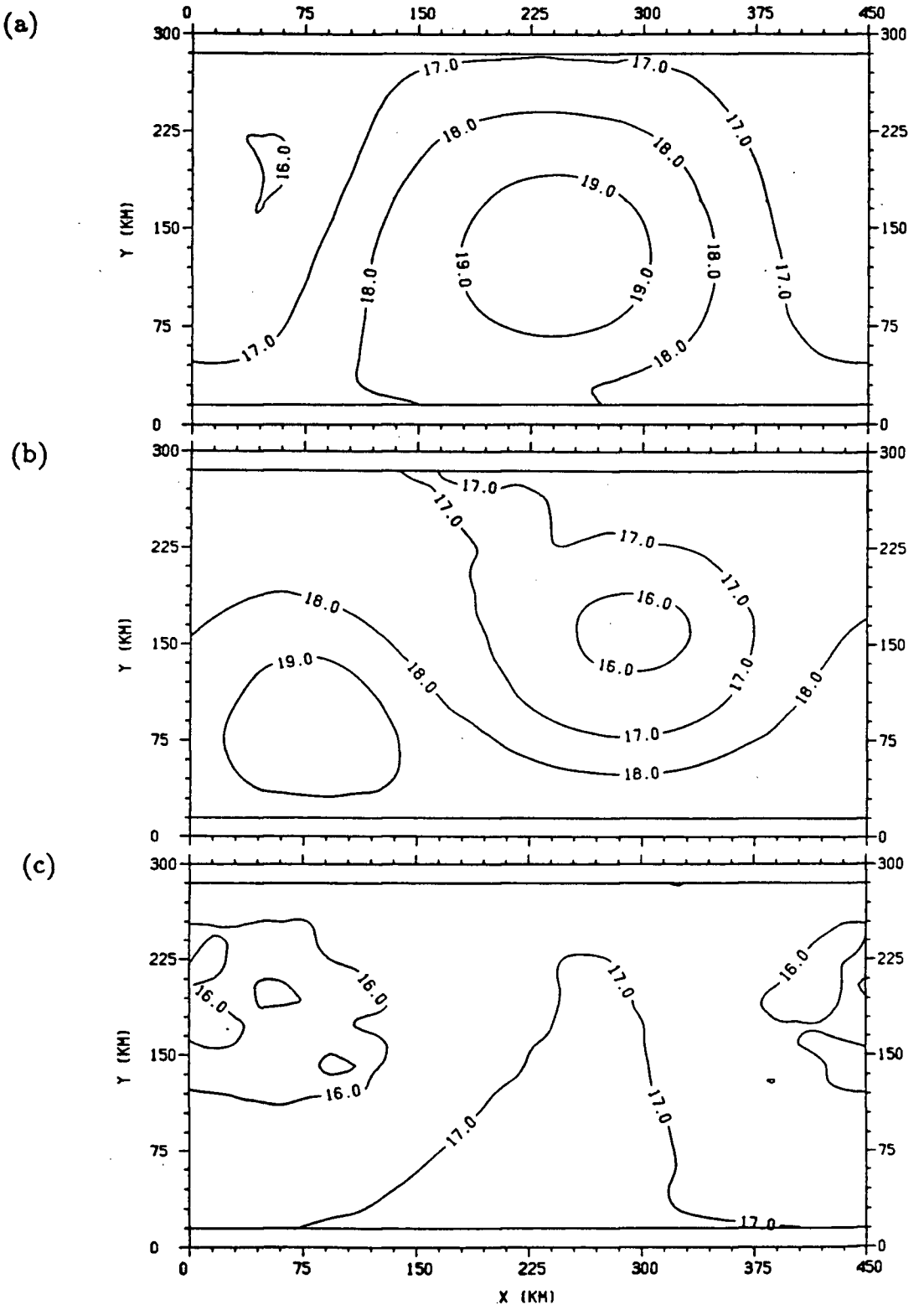

Figure 4.21: Comparison on day 120 of the level 3 (70 m) temperature (contour labels in °C) between (a) Run R, (b) Run A and (c) Run B.

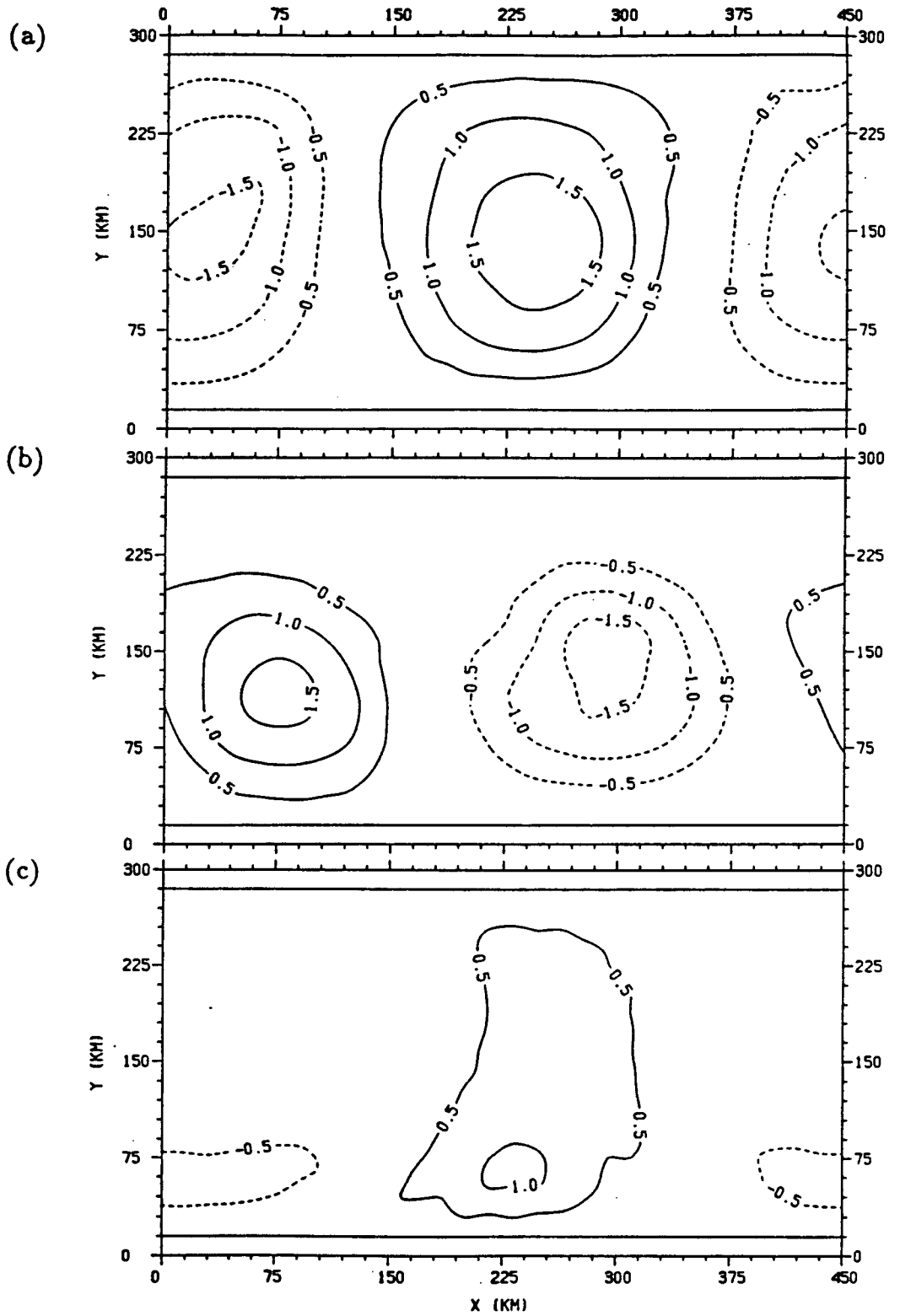

Figure 4.22: Comparison on day 120 of the level 3 (70 m) temperature anomaly (contour labels in °C) between (a) Run R , (b) Run A and (c) Run B.

downwelling occurring within the thermocline (to be described shortly). Therefore, although convection enables the assimilated colder (denser) near surface data to penetrate the deeper levels quickly which is critical for SST assimilation to be successful, it has the adverse effect of weakening the stratification as well as causing unrealistically cold temperatures in other areas of the ocean.

On the other hand, the assimilation of warmer (lighter) near surface temperature data into areas with underlying colder (denser) water has quite the opposite effect. In this situation, a warm slab of water, in many cases several degrees warmer than the subsurface temperatures, is confined to the surface level until advection and diffusion transfer the heat away. At the surface their effects are relatively weak. Vertical downwelling velocities are between -5 to $-10\,\mathrm{x}\,10^{-3}$ cm/s (see Fig. 4.25(b)) compared to $-50\,\mathrm{x}\,10^{-3}$ cm/s at 150 m (see Fig. 4.26(b)). Also, the diffusive processes, which operate on very long time scales, are particularly weak at the surface where the coefficient of vertical diffusion is smallest ($0.3\,\mathrm{cm}^2/\mathrm{s}$ from expression (2.31)).

To continue with the analysis of the different flow fields, time series from Run A and B are compared with those already described in §4.1 for Run R. Recall that the time series are measured at a fixed point in the centre of the channel. The time evolution of the 'surface' temperature of Run A and B at this location is plotted along with the corresponding 'surface' temperature from Run R in Figure 4.23(a) and (b) respectively. Referring first to the time series in Figure 4.23(a), the transient behaviour of the upper level temperature of the 'simulated' model (Run A (dashed-dotted curve)) with respect to that of the reference ocean (Run R (solid curve)) appears to be quite different, most notably in the later stages when a phase lag of approximately 180° shows up clearly. This phase difference is consistent with previous observations made from the contour plots (Fig. 4.20). Figure 4.23(b) compares the true SST field (solid curve) of Run R with the assimilated (approximate) SST field (bold solid curve) based on a

linearly-interpolated data-set. The point to note here is that there is no serious aliasing occurring through the interpolation procedure used to form a time continuous data-set from daily SST 'observations'. The major features of the transient temperature are well represented by the approximate data-set with only the small amplitude inertial oscillations at the very beginning and a few additional high frequency fluctuations being poorly resolved.

The assimilation does not affect the temperature at a depth of 200 m (level 5) until after day 30 whereupon the two fields of Run A and B start to show differences between them (compare dashed-dotted curves in Fig. 4.24(a) and (b)). Not only does the temperature of Run B exhibit a vast improvement in its long-term trend associated with the slower time scale of the barotropic Rossby waves (period $\approx$ 80 days), but its higher frequency characteristics (periods of less than 10 days) are also well-correlated with Run R after day 60.

The reason for the approximate 30 day delay before the model fields respond to the assimilation can be explained by examining the time series of the vertical velocity. First, the evolution of the level 2 (20 m) vertical velocities is shown in Figure 4.25. Notice that the prominent oscillation in Run R between day 10 and 30 is common to Run A as well although its amplitude and phase are slightly different (Fig. 4.25(a)). It should be mentioned that continuous assimilation of temperature (density) data into the upper level of Run B forces the vertical velocity which is strictly a diagnostic variable in the model, to undergo a dramatic adjustment at each time step in order to satisfy the mass conservation equation (2.7). This explains the generally larger and more erratic vertical velocities observed in Run B, particularly during the first 20 days (Fig. 4.25(b)). Also notice that the well-defined oscillation of Run A (and Run R) is absent at this level in Run B.

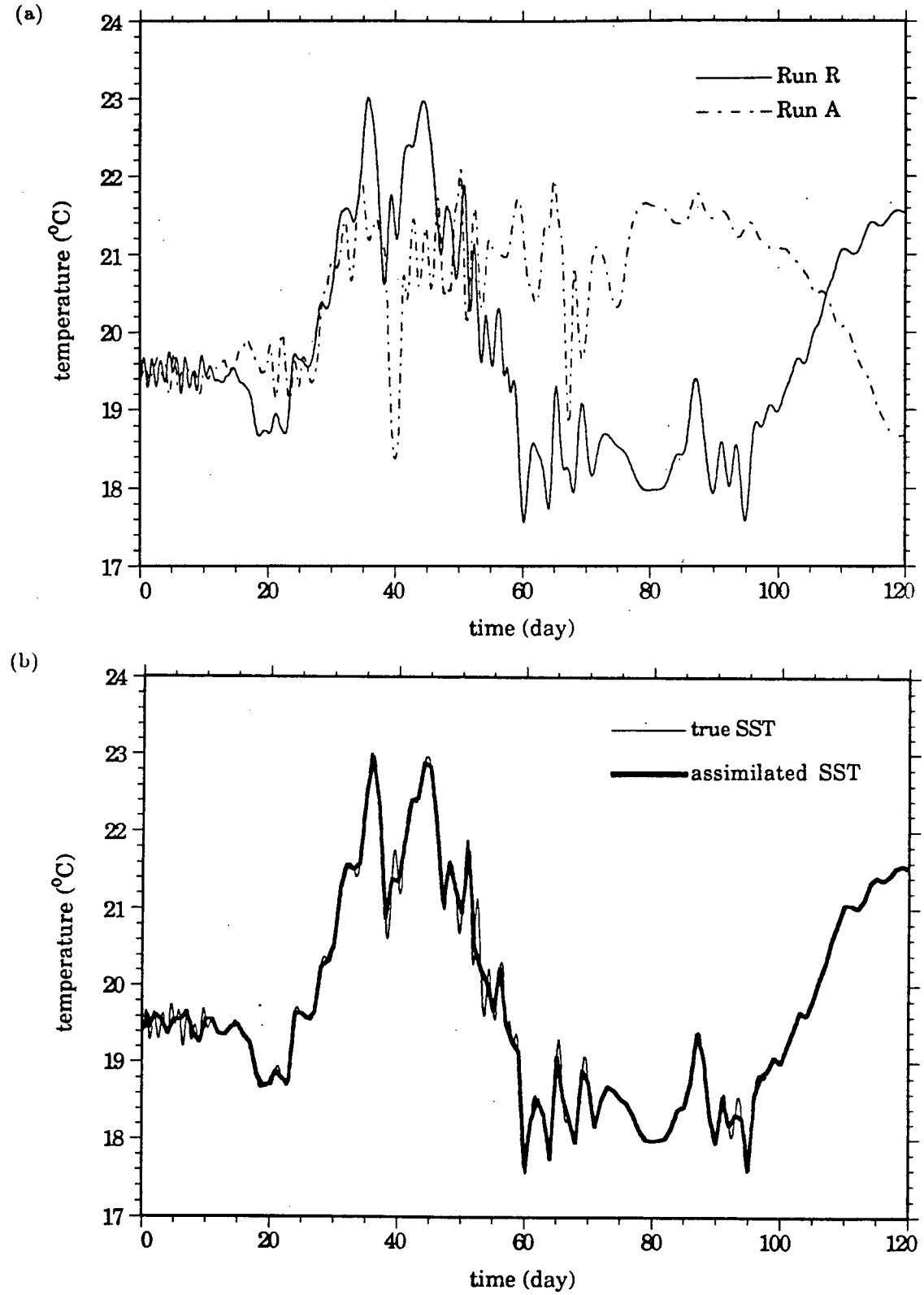

Figure 4.23: Time series of the level 1 (10 m) temperature field (in °C) at the fixed location ($i = 15, j = 10$) comparing (a) Run R and A and (b) Run R and B.

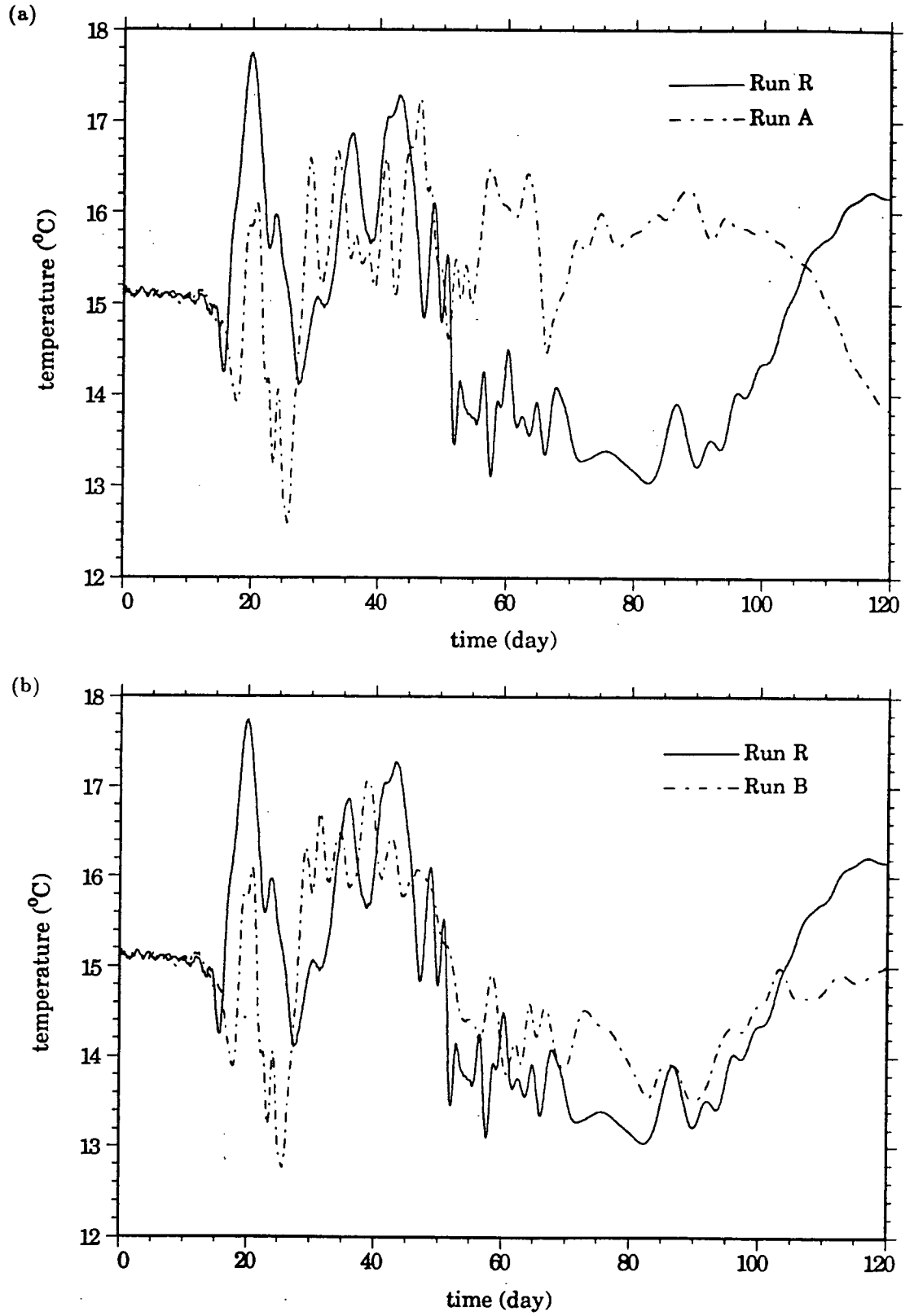

Figure 4.24: Time series of the level 5 (200 m) temperature field (in °C) at the fixed location ($i = 15, j = 10$) comparing (a) Run R and A and (b) Run R and B.

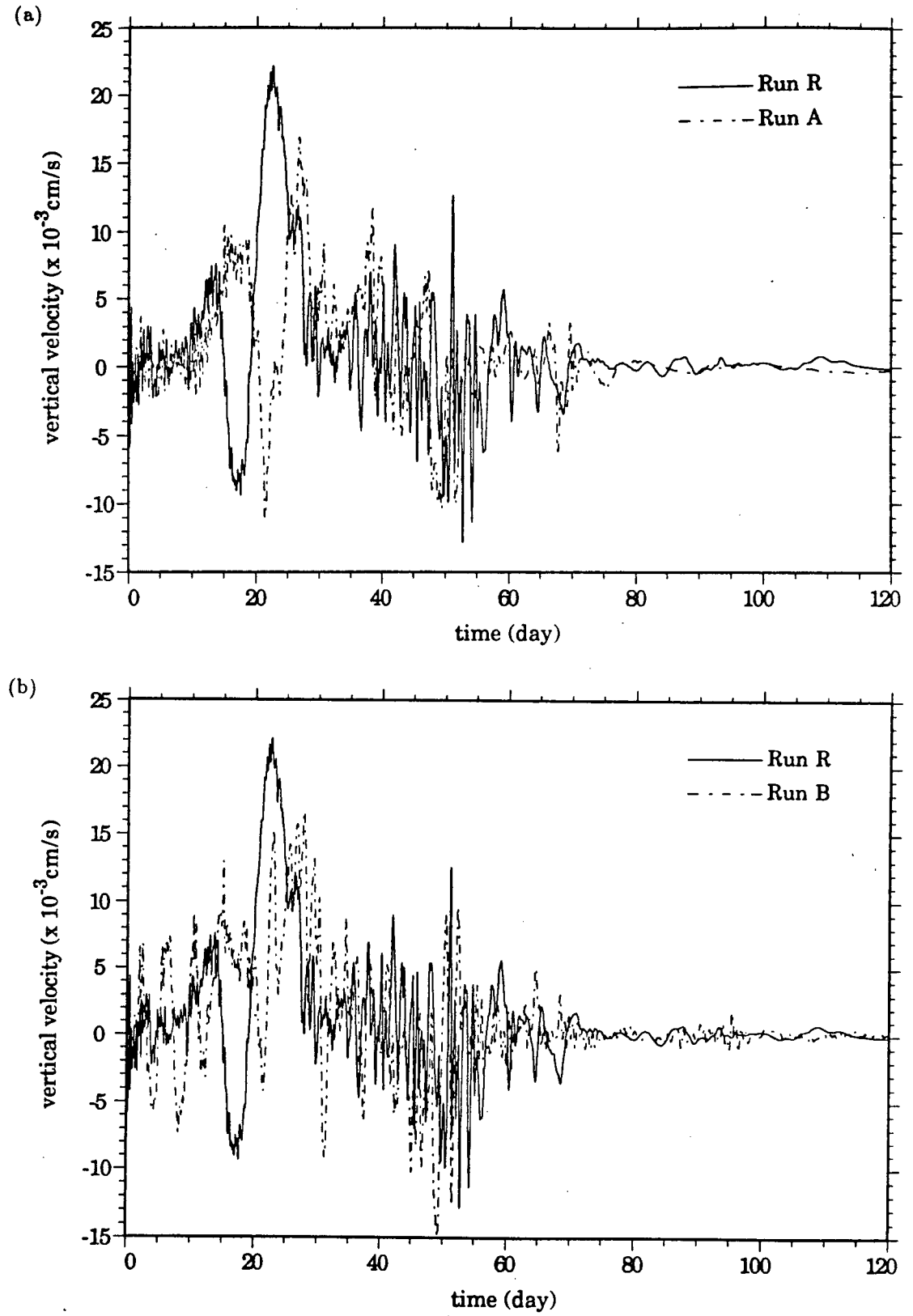

Figure 4.25: Time series of the level 2 (20 m) vertical velocity (in 10^{-3} cm/s) at the fixed location ($i = 15, j = 10$) comparing (a) Run R and A and (b) Run R and B.

In Figure 4.26, time series of the level 5 (150 m) vertical velocity are shown for the three runs. The large oscillation corresponding to the passage of an unstable wave, is the dominant feature showing up in Run B and A. (Note the oscillation's phase lag ($\approx$ 5 days) with respect to Run R and also the significantly larger amplitude (over 5 times) with respect to level 2). It is the downwelling associated with this oscillation that is the primary mechanism leading to the effective advection of assimilated SST to depth. In fact, it is only after this event (i.e., after day 30) that the velocity field of Run B begins to exhibit significant changes and eventual improvement over that of Run A, a point well-illustrated in Figure 4.27 showing the evolution of the north-south velocity component at level 1 (10 m).

4.4 Additional Experiments

To investigate further the importance of the strong downwelling event occurring during the first month of integration, two additional data assimilation experiments are conducted. In the first experiment, SST data are assimilated (by direct insertion) into Run B for the first 30 days only (i.e., up to the end of the downwelling event). Thereafter, the assimilation of SST is discontinued and the model is integrated forward for the remainder of the run as a strictly predictive model. This experiment will be referred to as Run B2; Run B referring to the direct SST assimilation experiment already described in detail in §4.2 and §4.3. In the second experiment (Run B3), the insertion of SST is carried out only for the time period between days 30 and 120 (i.e., immediately following the downwelling event), so that during the first 30 days, Run B is predictive like Run A.

The RMS_k^B, $(k = 1, 5, 10)$, errors for Runs B, B2 and B3 are shown together with the standard RMS_k^A, $(k = 1, 5, 10)$, error in Figures 4.28–31 for temperature, N-S and E-W

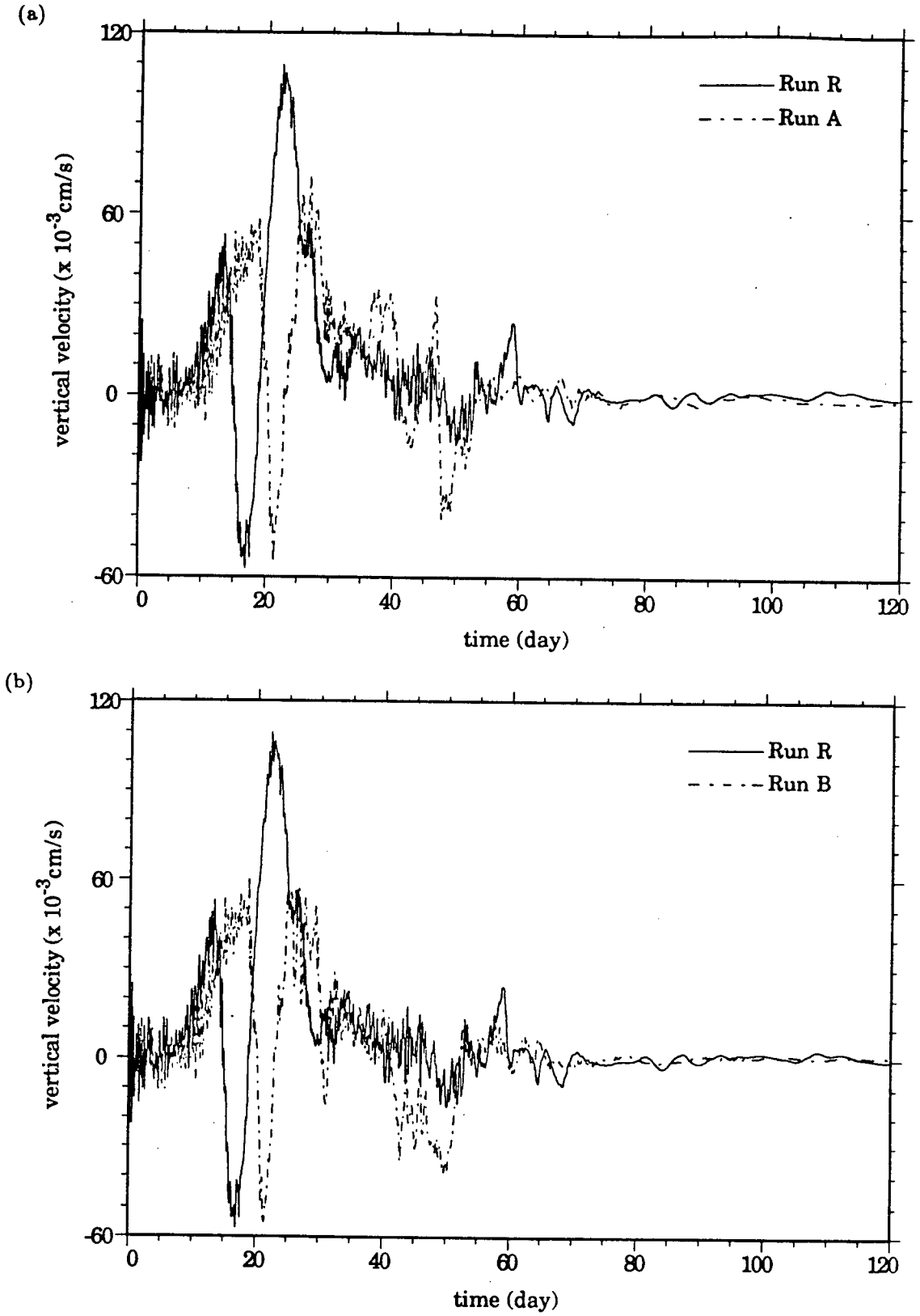

Figure 4.26: Time series of the level 5 (150 m) vertical velocity (in 10^{-3} cm/s) at the fixed location ($i = 15, j = 10$) comparing (a) Run R and A and (b) Run R and B.

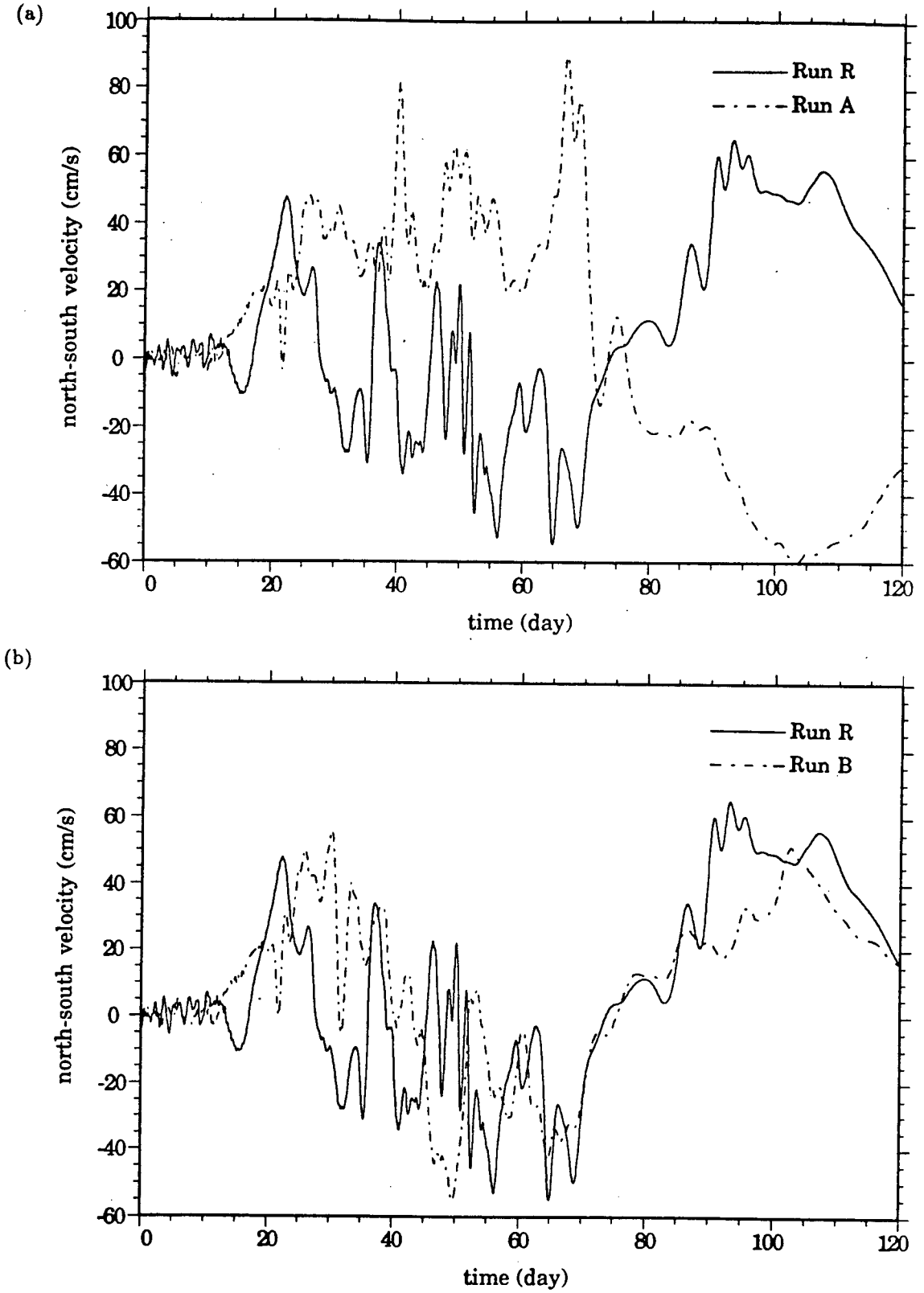

Figure 4.27: Time series of the level 1 (10 m) N-S velocity component (in cm/s) at the fixed location ($i = 15, j = 10$) comparing (a) Run R and A and (b) Run R and B.

velocity, and the barotropic streamfunction respectively. The RMS_k^A error is represented by the solid curves and the RMS_k^B errors for Runs B, B2 and B3 are represented by the dashed, dotted and dashed-dotted curves respectively. It is clear from all these figures that Run B2 is much more effective than Run B3 in reducing the RMS_k^B errors of the different model fields. In fact, the results from Run B3 very clearly indicate a worsening of the model fields except for the N-S velocity component. The results of Run B2, on the other hand, actually indicate a greater improvement in comparison with the basic experiment Run B. This suggests, therefore, that the assimilation of SST during the first month of integration is sufficient to significantly reduce the errors in all fields but that further assimilation of SST could be detrimental to the model.

Notice that the surface temperature of Run B2, which after day 30 is no longer a continuously assimilated field but a predicted one, shows a vast improvement over Run A by day 120 (Fig. 4.28(a)). The near vertical dotted (dashed-dotted) line at day 30 in Figure 4.28(a) corresponds to a sudden error growth (reduction) when data assimilation is 'turned-off' ('turned-on') in Run B2 (Run B3). Contour plots in Figure 4.32 of the upper level temperature and temperature anomaly fields of Run B2 (day 120) show that the major features of the 'real ocean' SST field have been reconstructed reasonably well (compare with Fig. 4.19). The positioning of the eddies has been restored although the temperatures vary about 1°C – the warm eddy being about 1°C colder and the cold eddy about 1°C warmer than reality. The upper level temperature field in Run B3 is an assimilated 'observational' data-set at day 120 and, therefore, corresponds exactly to the SST field of Run R in Figure 4.19.

Comparing the level 3 (70 m) temperature and temperature anomalies of Run B2 in Figure 4.33 with those in Figures 4.21 and 4.22 reveals that the problem of weaker anomalies and generally colder subsurface temperatures has been alleviated to a great extent. The warm anomaly is particularly well-represented, however the cold anomaly

is still about 0.5°C warmer in Run B2. In contrast, the corresponding plots for Run B3 in Figure 4.34(b) illustrate substantially weaker anomalies with maximum strengths about ±0.5°C compared to ±1.5°C in Run R. Also, notice in Figure 4.34(a) that Run B3 has been completely ineffective in reconstructing the predominant warm eddy in the centre of the channel of Run R. The subsurface thermal fields of Run B3 actually indicate a weak cold eddy in this region.

The implications on the barotropic field in Run B3 are severe as illustrated in Figure 4.36 (compare with Fig. 4.18). Lying central in the channel, is an intense cyclonic cell ($\approx$ 50 Sv) compared to a prominent anticyclonic cell in the same region in Run R. In contrast, the streamfunction patterns of Run B2 in Figure 4.35 show an improvement similar to Run B (compare with Fig. 4.18(c)). The estimates of the transports are still overestimated in the cyclonic cell and underestimated in the anticyclonic cell by about 20 Sv in both but this, nevertheless, is an improvement over Run B which predicted transports with errors on the order of 30 Sv.

The results presented in this section have illustrated two important points regarding the assimilation of SST. First, is the crucial requirement that the dynamics of the model be able to transfer assimilated SST into subsurface information. In the experiments performed here, this is achieved by intense downwelling arising from baroclinically unstable events during the first month of integration. Second, is that in the absence of effective dynamical transfer processes, there is a strong tendency for SST assimilation to harm the model. For example, when the flow is strongly barotropic, the most effective surface to subsurface transfer mechanism is convection, occurring when the assimilation of SST yields an unstable water column. However, as discussed in §4.3, there are serious adverse effects associated with the convective mixing of assimilated data. On the other hand, if the stability of the water column is maintained after assimilation, then the only vertical transfer mechanism (in the strongly barotropic case) is diffusion. As mentioned

in §4.3, the time scales associated with vertical diffusive processes are very long (e.g., the time required for temperature to diffuse (with $A_{HV} = 0.3\,\mathrm{cm}^2/\mathrm{s}$) from level 1 (10 m) to level 2 (35 m) is $t_{\mathrm{diff}} = H^2/A_{HV} \approx 240$ days!). Therefore, besides convection, another possible danger with continuous SST assimilation is the creation of unrealistically large temperature differences between the top two levels of the model as diffusion is unable to vertically smooth out the assimilated warm surface temperature. In these experiments, the surface temperature can be up to 4°C warmer than that in the second level.

(a)

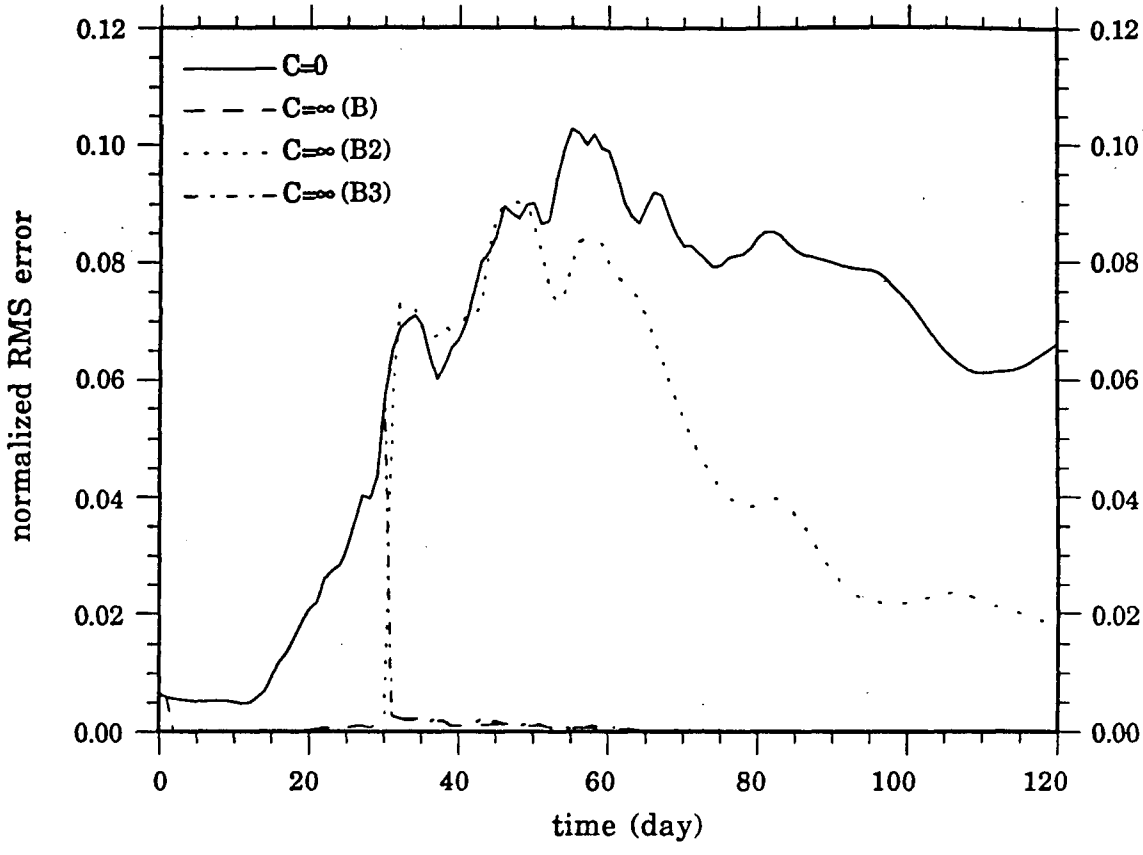
C=0
C=∞ (B)
C=∞ (B2)
C=∞ (B3)
normalized RMS error
time (day)
0.00
0.02
0.04
0.06
0.08
0.10
0.12
0
20
40
60
80
100
120

(b)

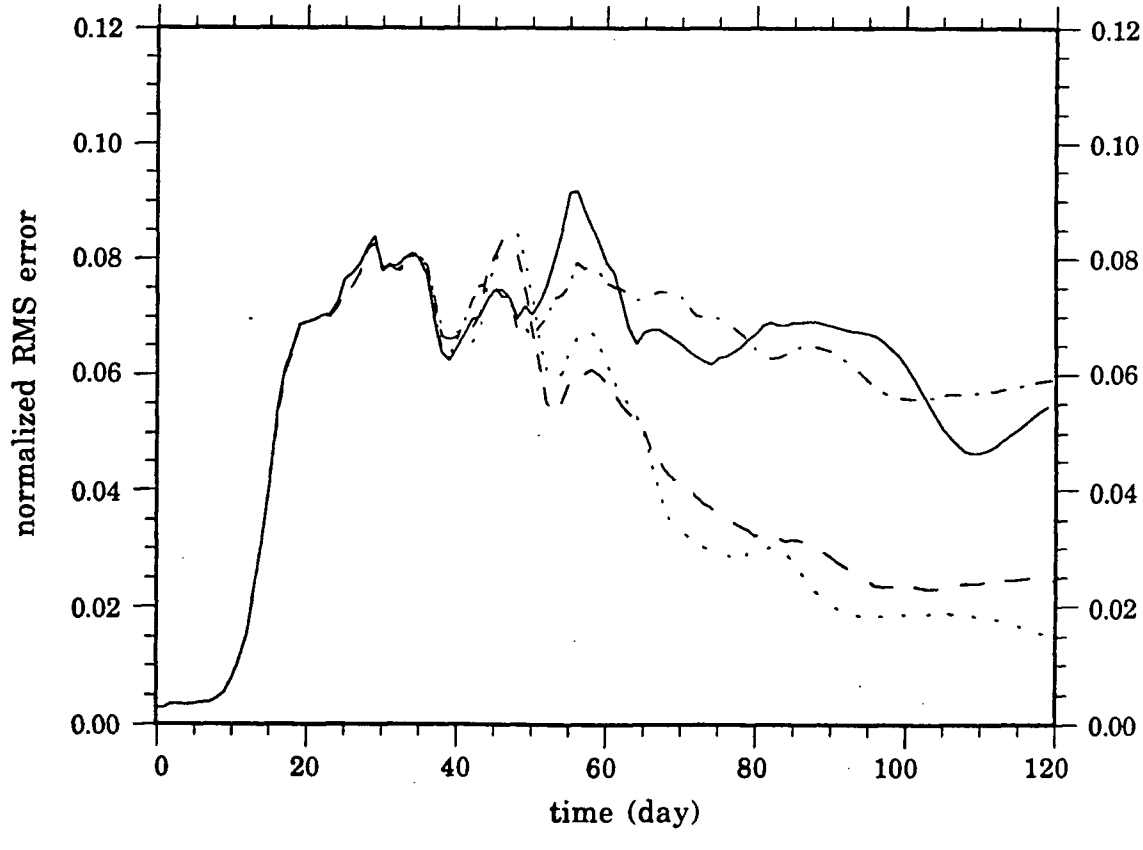
normalized RMS error
time (day)
0.00
0.02
0.04
0.06
0.08
0.10
0.12
0
20
40
60
80
100
120

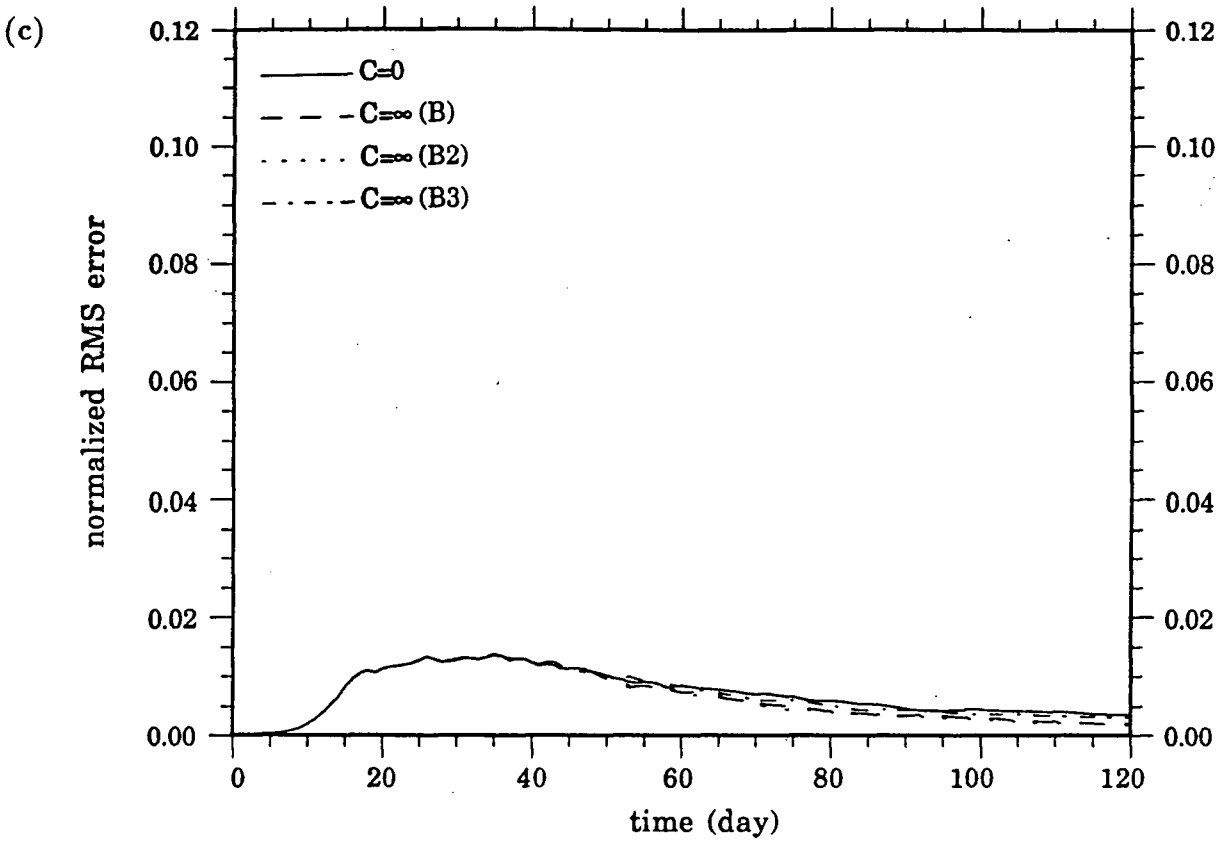

Figure 4.28: The time evolution of the (normalized) temperature RMS error (in °C) at (a) level 1 (10 m), (b) level 5 (200 m) and (c) level 10 (2200 m) for Run A and assimilation experiments Run B, B2 and B3 (see legend).

(a)

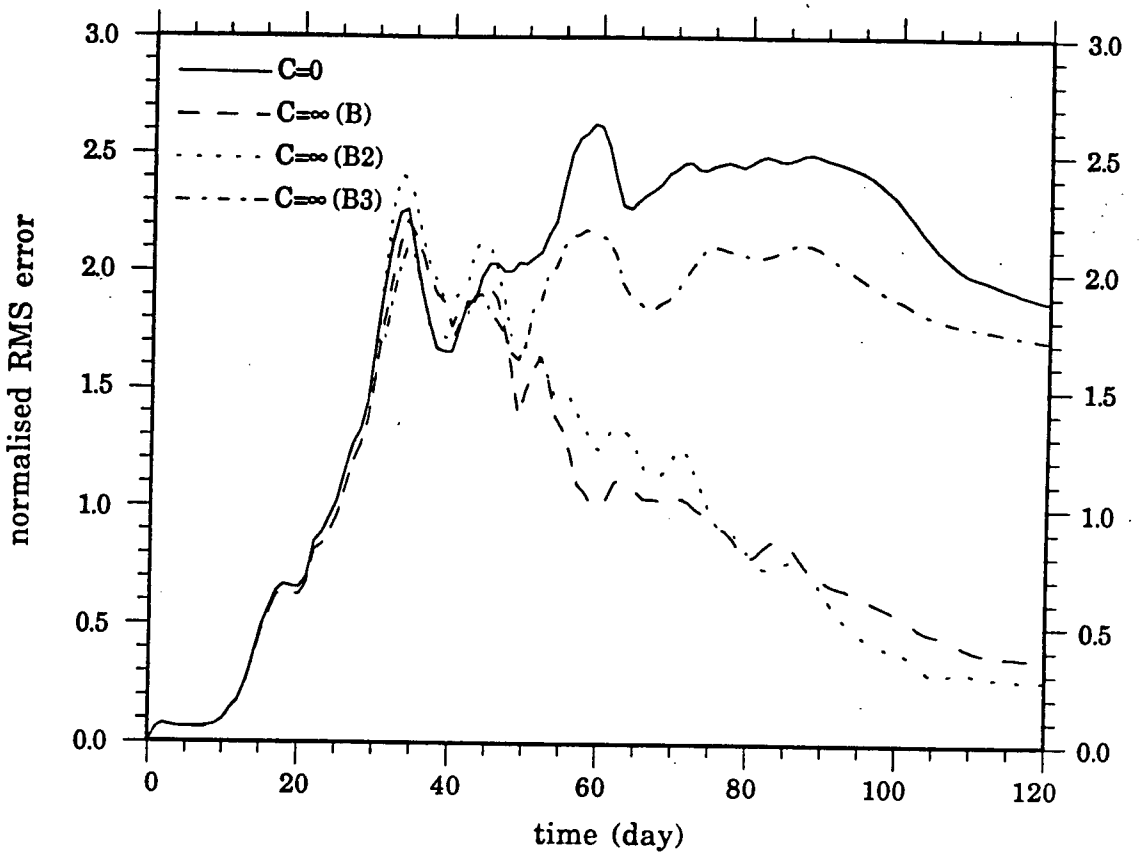
C=0
C=∞ (B)
C=∞ (B2)
C=∞ (B3)
normalised RMS error
time (day)
0.0
0.5
1.0
1.5
2.0
2.5
3.0
0
20
40
60
80
100
120

(b)

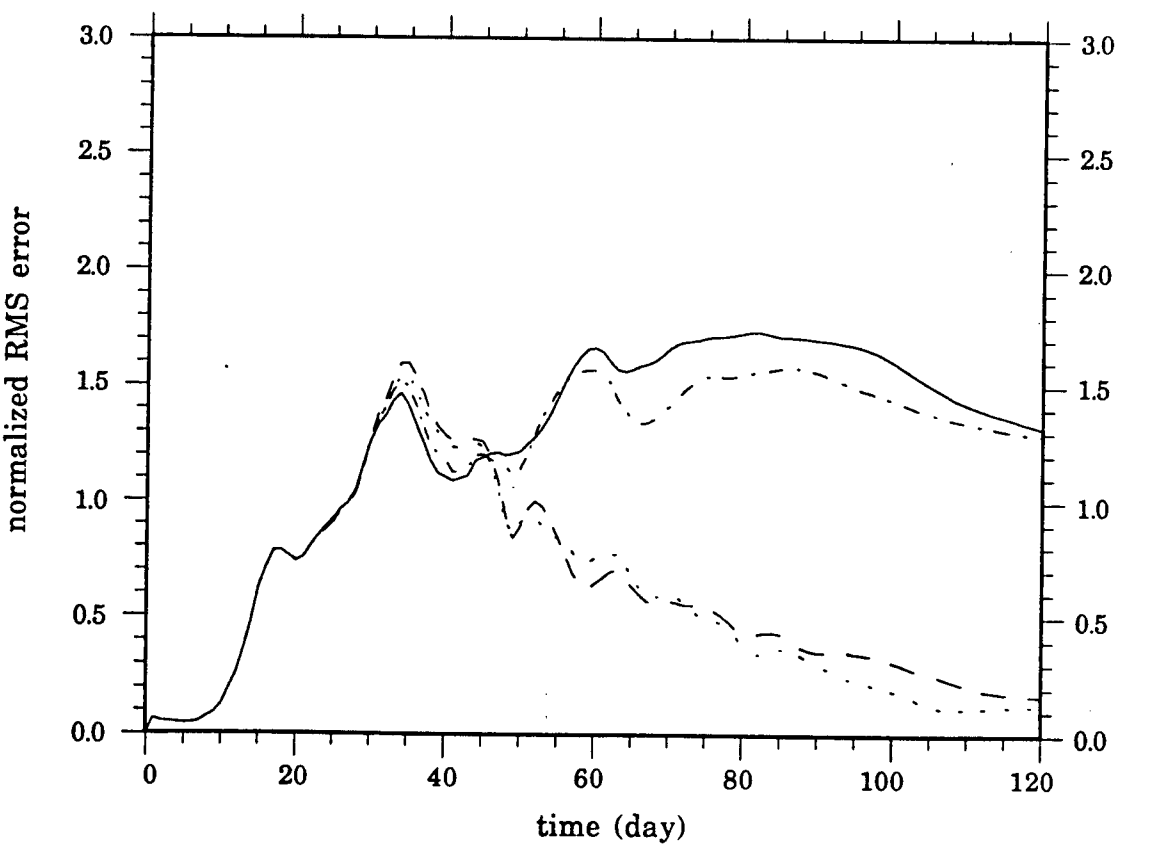
normalized RMS error
time (day)
0.0
0.5
1.0
1.5
2.0
2.5
3.0
0
20
40
60
80
100
120

(c)

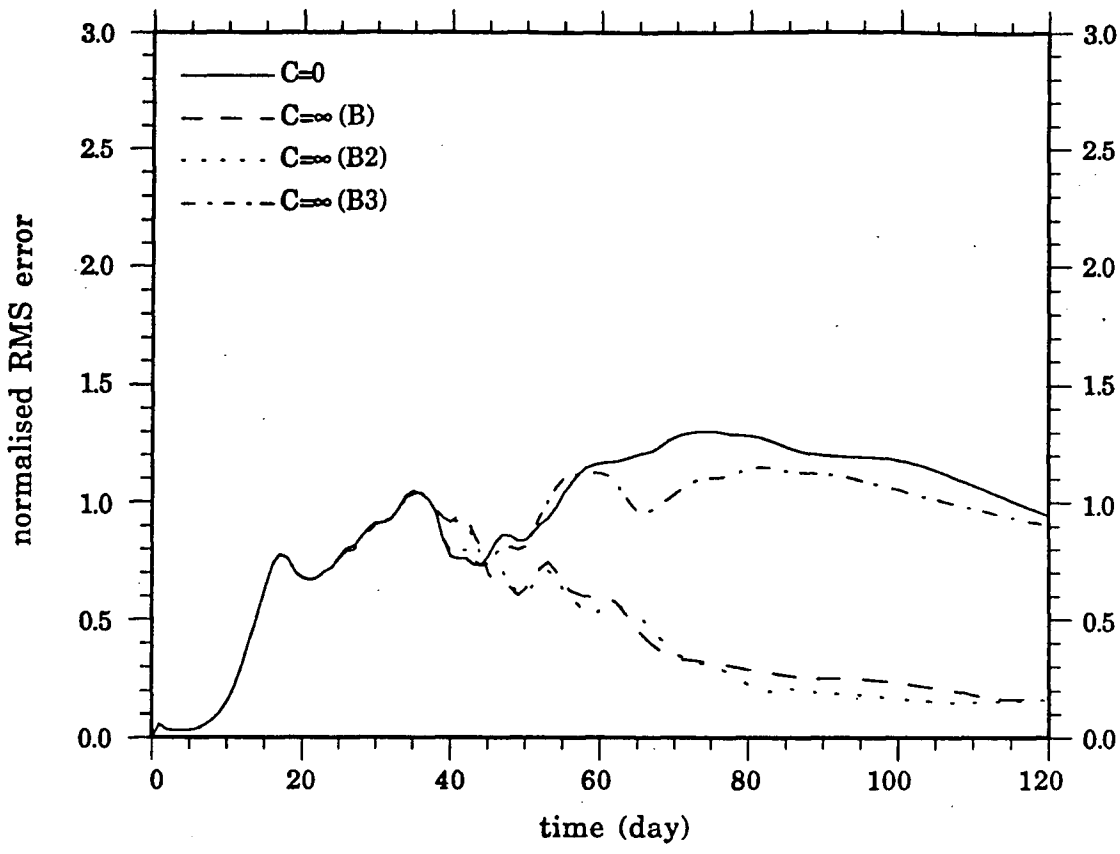

Figure 4.29: The time evolution of the (normalized) N-S velocity component RMS error (in cm/s) at (a) level 1 (10 m), (b) level 5 (200 m) and (c) level 10 (2200 m) for Run A and assimilation experiments Run B, B2 and B3 (see legend).

(a)

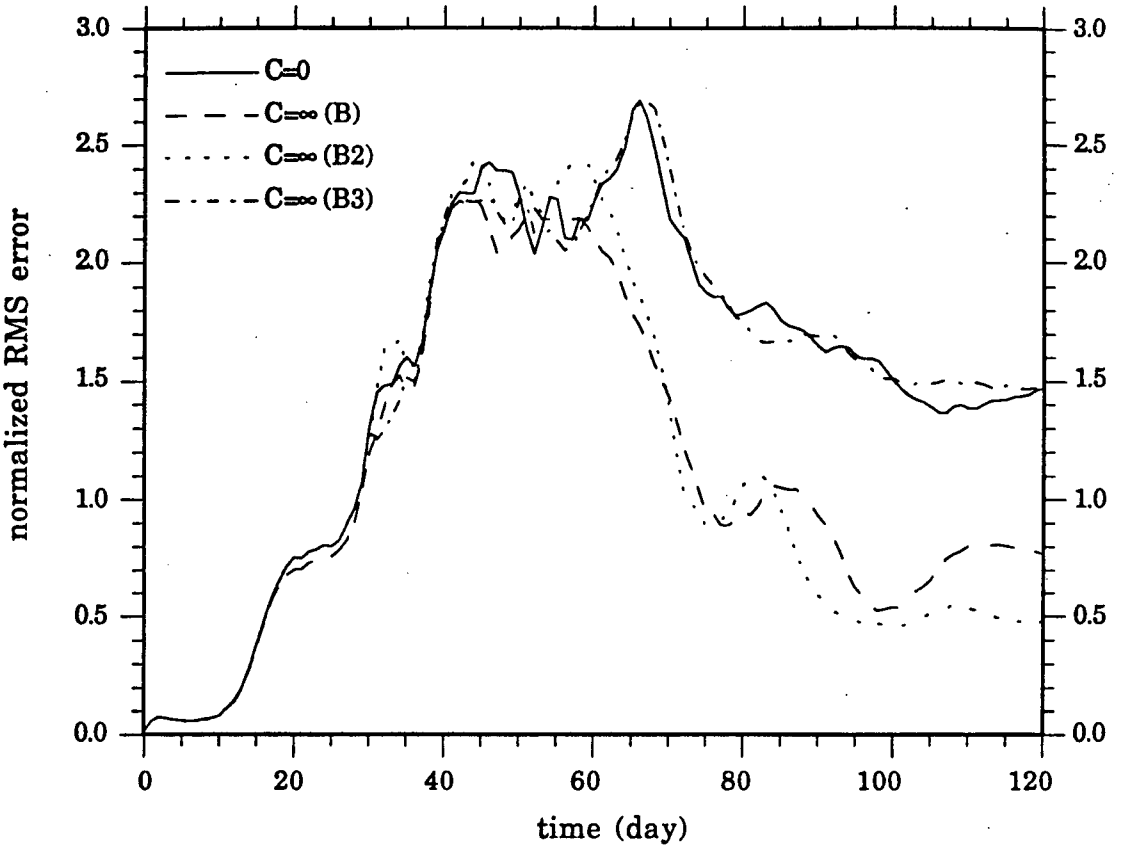
C=0
C=∞ (B)
C=∞ (B2)
C=∞ (B3)
normalized RMS error
time (day)
0.0
0.5
1.0
1.5
2.0
2.5
3.0
0
20
40
60
80
100
120

(b)

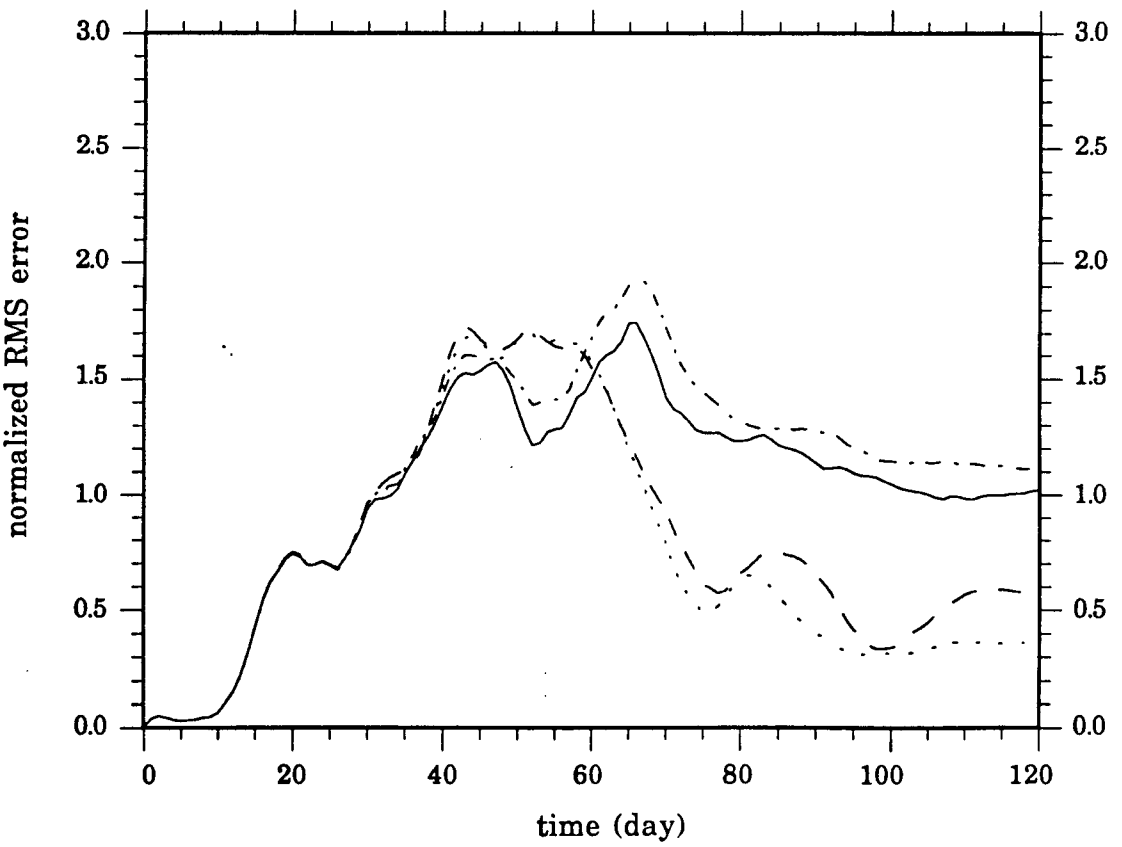
normalized RMS error
time (day)
0.0
0.5
1.0
1.5
2.0
2.5
3.0
0
20
40
60
80
100
120

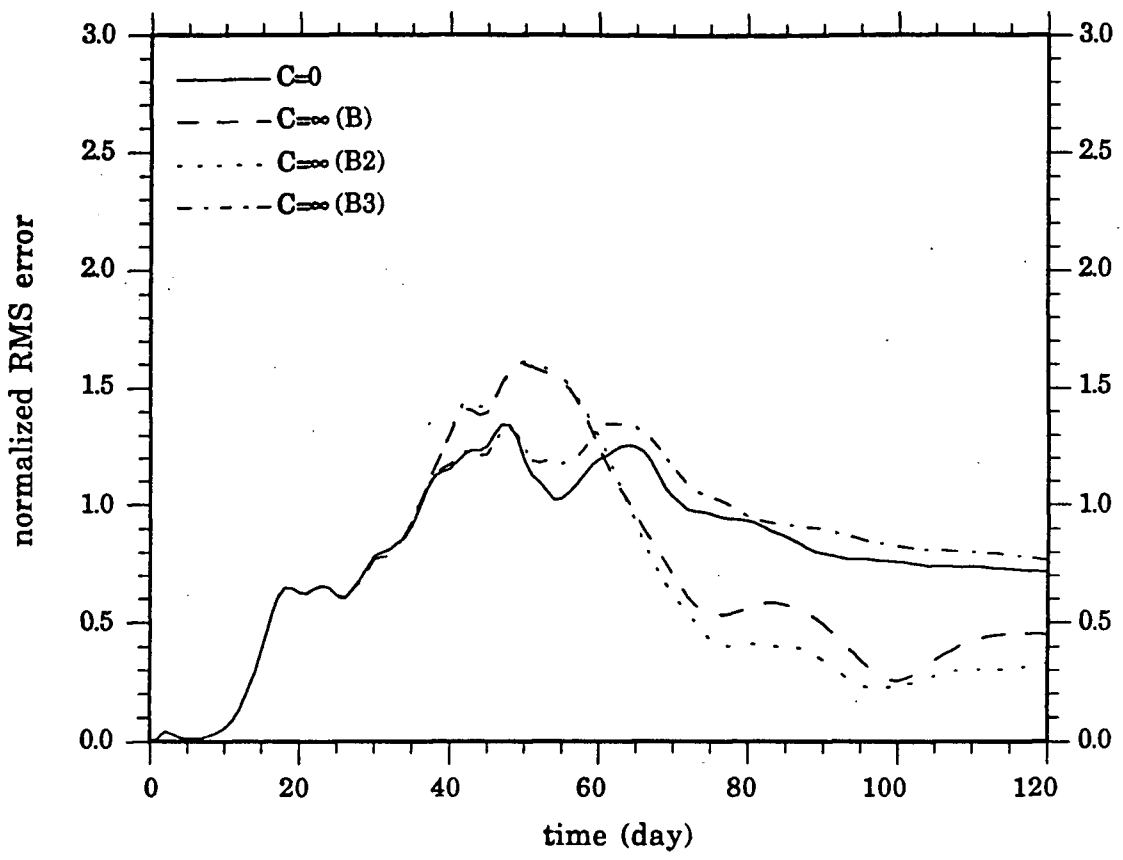

Figure 4.30: The time evolution of the (normalized) E-W velocity component RMS error (in cm/s) at (a) level 1 (10 m), (b) level 5 (200 m) and (c) level 10 (2200 m) for Run A and assimilation experiments Run B, B2 and B3 (see legend).

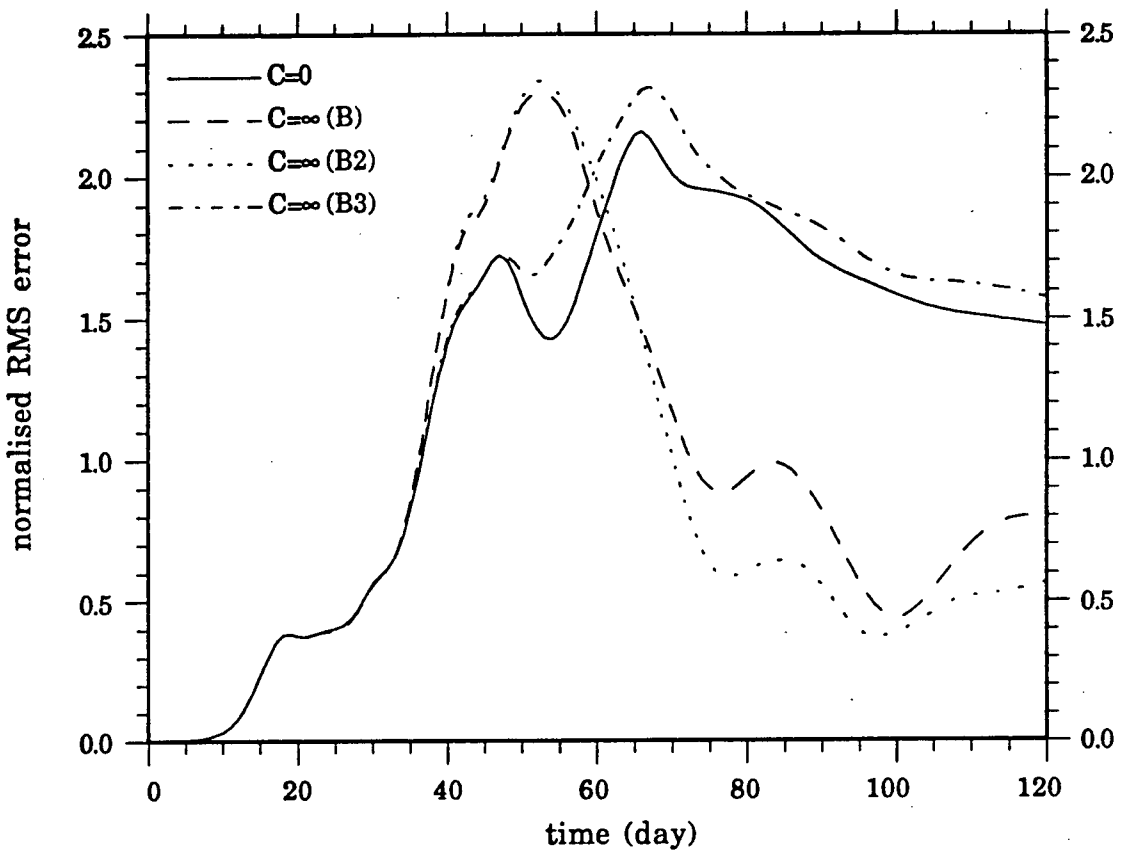

Figure 4.31: The time evolution of the (normalized) streamfunction RMS error (in Sv) for Run A and assimilation experiments Run B, B2 and B3 (see legend).

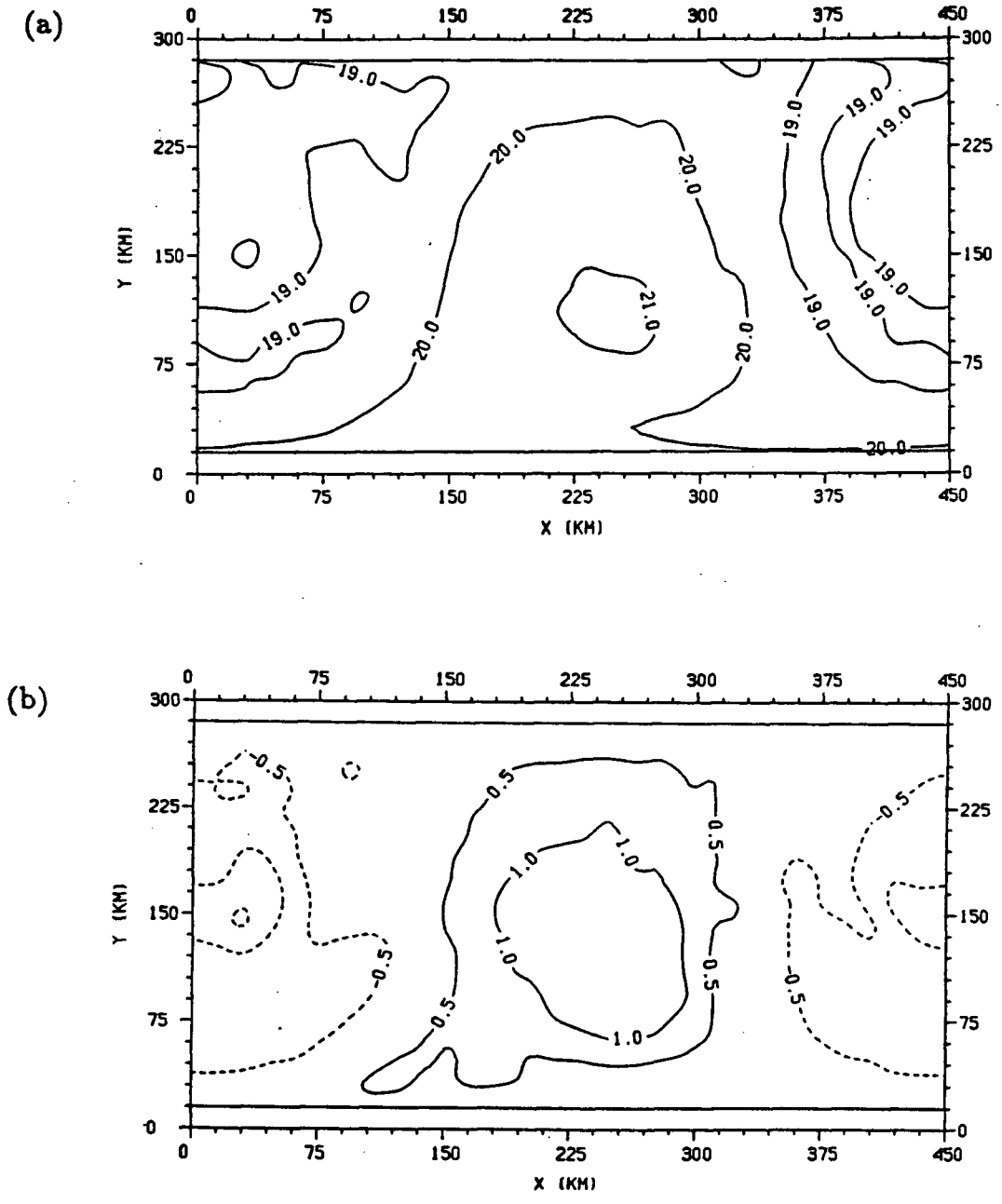

Figure 4.32: The level 1 (10 m) (a) temperature (contour labels in °C) and (b) temperature anomaly (contour labels in °C) at day 120 for Run B2.

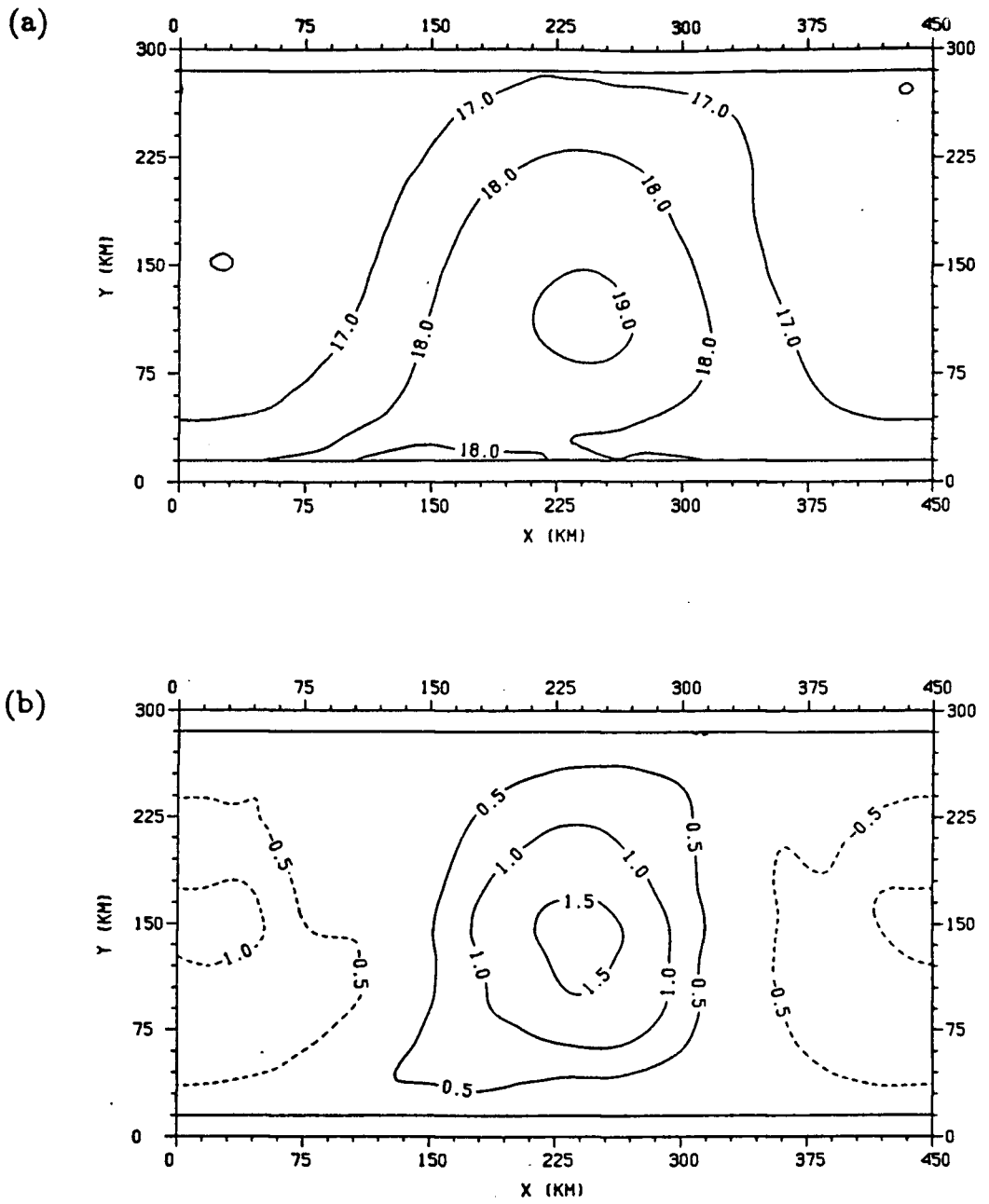

Figure 4.33: The level 3 (70 m) (a) temperature (contour labels in °C) and (b) temperature anomaly (contour labels in °C) at day 120 for Run B2.

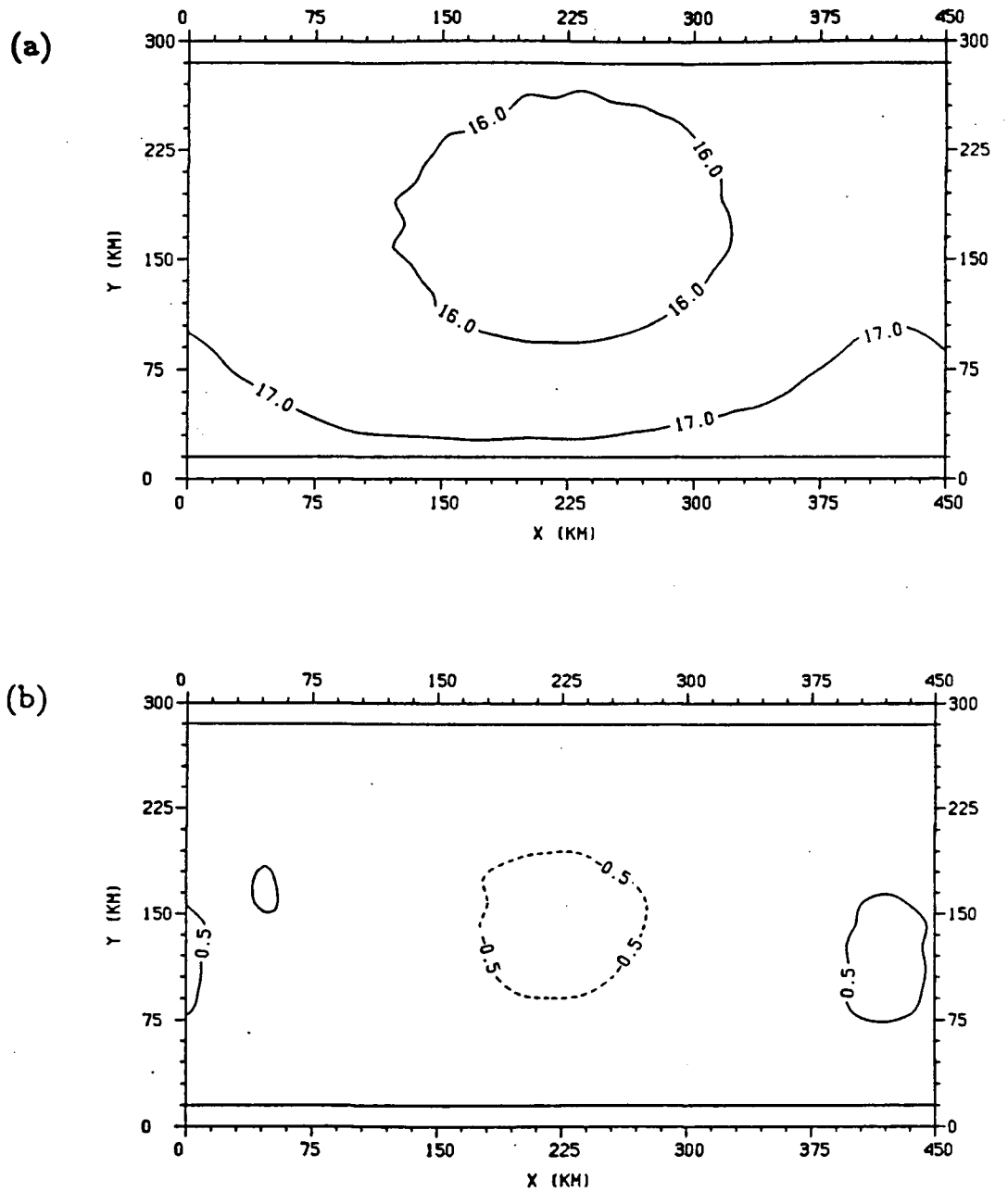

Figure 4.34: The level 3 (70 m) (a) temperature (contour labels in °C) and (b) temperature anomaly (contour labels in °C) at day 120 for Run B3.

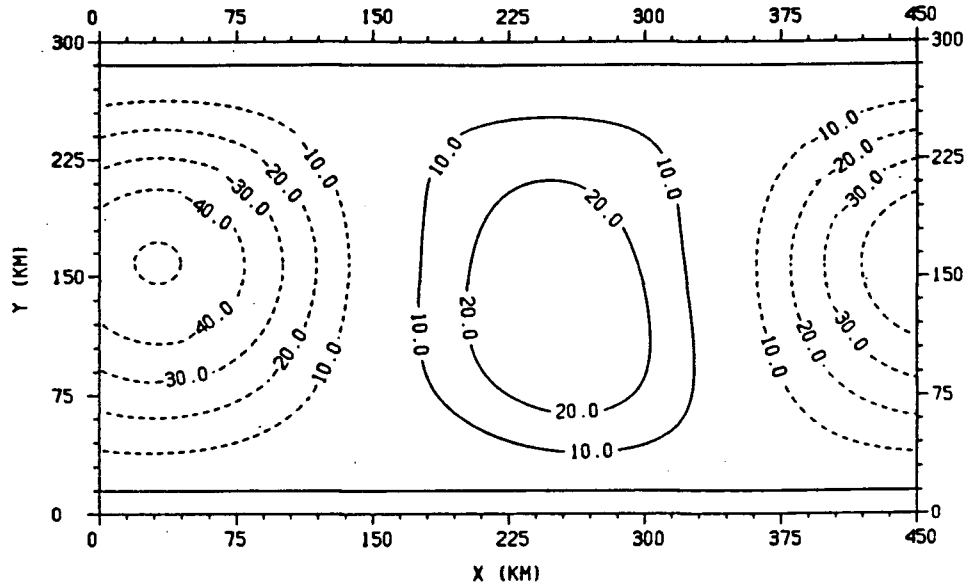

Figure 4.35: The barotropic streamfunction (contour labels in Sv) at day 120 for Run B2. Solid and dashed contours correspond to anticyclonic and cyclonic circulations respectively.

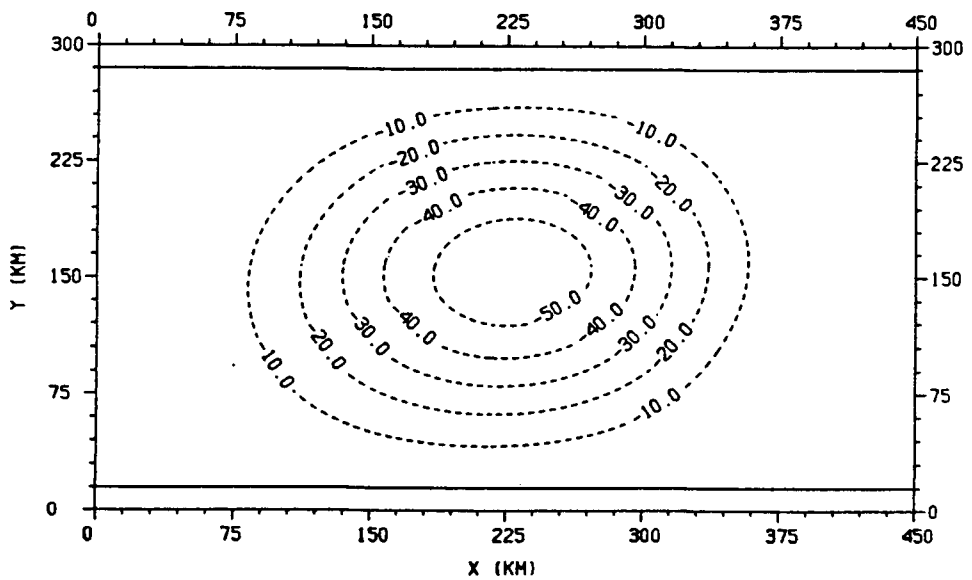

Figure 4.36: The barotropic streamfunction (contour labels in Sv) at day 120 for Run B3. Solid and dashed contours correspond to anticyclonic and cyclonic circulations respectively.

Chapter 5

Summary and Conclusions

With the advent of satellite remote sensing techniques, oceanographers are now provided with ocean surface data of global coverage. These data include synoptic measurements of sea surface height (from altimetry) and temperature (from radiometry) together with measurements of the ocean's major forcing mechanism, the wind stress field (from scatterometry). Of these, satellite sea surface temperature (SST) measurements have the best spatial and temporal resolution and are, in general, the most readily available. It is desirable, therefore, to determine whether the assimilation of SST (alone) into a numerical ocean model may be effective in improving the model's prediction of the ocean circulation. This was the object of this study.

A series of idealized data assimilation experiments has been carried out to examine the effects of SST assimilation into an OGCM. A methodology similar to the 'identical twin' approach has been employed in which the model itself is used to simulate a reference ocean in a control integration. The control run which is derived from an assumed 'perfect' initial state, provides a complete description of the 'real ocean' from which we can (1) collect 'observational data' for assimilation and (2) estimate the errors in the predicted fields of the simulation runs. In contrast to the control model, the simulation model has been initialized with an 'imperfect' data-set.

The experiments have been conducted using the sophisticated GFDL Bryan-Cox-Semtner primitive equation OGCM set-up as an unforced, eddy-resolving, flat bottomed channel of uniform depth. A zonally uniform jet in approximate geostrophic balance

with an imposed along-channel temperature front constituted the basic initial state for the various model runs. The 'perfect' and 'imperfect' initial conditions of the control model and simulation model respectively were established by randomly perturbing this balanced state differently in each model. The introduction of the perturbation was also necessary to enable meander growth and subsequent shedding of eddies. As the perturbed initial fields of the two models were different, the transient features of their respective flow fields were distinct. Thus, the primary question addressed in this study was: "can the assimilation of time-dependent SST 'observations' alone be sufficient to drive the simulation model toward the 'real ocean'?"

The assimilation technique used is based on the simple 'nudging' scheme in which sequential observations of SST are blended with corresponding model predicted fields through a linear relaxation condition applied at the upper boundary. A series of 'trial and error' experiments revealed that the most effective method for assimilating SST was to insert the 'observations' directly into the model. This corresponds to the extreme case of setting the relaxation parameter in the 'nudging' term to be infinite. This abrupt form of data assimilation resulted in a substantial improvement in the temperature and velocity (baroclinic and barotropic) fields at all levels. This improvement was quantified by monitoring the time evolution of the root mean square (RMS) errors relative to the reference ocean. In contrast, SST data proved quite ineffective in reducing the RMS errors when assimilated into the upper level temperature field on longer relaxation time scales of 4 days and 1/2 day respectively.

An analysis of the flow fields revealed that the improvement seen in the direct insertion experiment stemmed from the model's ability to transfer assimilated SST into subsurface information through intense downwelling arising from baroclinically unstable events during the first month of the run. Only after the information had been advected to the deeper levels in this manner did the velocity fields begin to

evolve differently from those in the model without SST assimilation, thereby showing the weak dynamical relationship between SST and the circulation in ocean models. Further experimentation revealed that the reconstruction of the eddy flow field was best achieved when the insertion of SST was discontinued immediately following the strong downwelling event, thereafter enabling the surface (upper level) temperature field to adjust prognostically with the other model fields. When assimilated in the absence of an effective dynamical transfer mechanism (i.e., when the model was predominantly barotropic), SST degraded the model performance slightly.

Assimilating cool SST over warm subsurface water contrasted sharply with assimilating warm SST over cool subsurface water. In the former, convective overturning enabled the assimilated cool SST to rapidly penetrate through the thermocline after which strong vertical velocities advected the information to the deeper levels. This process, however, adversely affected the vertical thermal structure by an unrealistic deepening of the mixed layer. In the latter, the surface to subsurface transfer of information occurred on a much slower time scale producing in many cases unrealistically large temperature differences between the warm surface level and the water below. The different features of cold and warm SST assimilation coupled to produce generally colder than normal subsurface waters and weakened horizontal temperature gradients. These problems were overcome to a great extent when the continuous insertion of SST was performed for the first month only and then 'turned-off' for the remainder of the run. Otherwise, systematically biased injection of coldness into the model may have to be compensated in long-term assimilation experiments by some form of 'heat flux correction'.

Since the results from these experiments indicate that the success of SST assimilation is highly dependent on the physical mechanisms in the model being able to effectively communicate the assimilated surface information to the subsurface, it seems

that an a priori understanding of the dynamics in the region of interest is essential to ensure the feasibility of assimilating real SST data into a realistic ocean model. In addition, the assimilation of real SST would require other important considerations, namely: (1) Satellite measurements of SST will contain experimental error and will not be as dynamically compatible with the model as the simulated 'observations' used in this study; (2) In many regions satellites will give no data due to extensive cloud cover; (3) The SST field in some cases may bear little resemblance to the subsurface thermal structure particularly in areas of intense surface forcing (Robinson et al., 1989). Consequently, definitive warm and cold eddy features appearing in the subsurface field may be disguised in the SST signature, or conversely, no eddies may exist in regions where visible warm or cold patches of water at the surface suggest otherwise. This situation did not occur in the unforced experiments here as cold and warm eddies had a distinct manifestation in the surface (upper level) temperature field.

The complexities implied by the above remarks suggest that further experimentation reflecting more realistic situations is needed to assess the feasibility of inserting SST data into a numerical model. For example, there is the obvious extension to include surface forcing (heat/salt fluxes and wind stress) and possibly a bulk-mixed layer formulation (e.g., Kraus and Turner (1967)). In addition, the assumptions of 'perfect' data with 'perfect' spatial coverage need to be relaxed to address cases (1) and (2) above. To alleviate many of the defficiencies associated with SST, supplemental assimilation data-sets (e.g., altimeter and/or XBT) should be considered if they are available.

Bibliography

[1] Anthes, R.A., 1976: Data assimilation and initialization of hurricane prediction models. J. Atmos. Sci., 31: 702-719.

[2] Arakawa, A., 1966: Computational design for long-term numerical integration of the equations of fluid motion: Two dimensional incompressible flow. Part 1. J. Comput. Phys., 1: 119-143.

[3] Arakawa, A.. and V.R. Lamb, 1977: Computational design of the basic dynamical processes of the UCLA General Circulation Model. In: Methods in Computational Physics, Vol. 17. Academic Press, New York, pp. 174-265.

[4] Bengtsson, L., 1975: Four-dimensional assimilation of meteorological observations. World Meteor. Org., International Council of Scientist Unions, Joint Organizing Committee, 75 pp. [GARP Publ. Ser. No. 15.]

[5] Bengtsson, L., M. Ghil and E. Källén (Eds.), 1981: Dynamic Meteorology: Data Assimilation Methods. Springer-Verlag, 330 pp.

[6] Bennett, A.F., and W.P. Budgell, 1987: Ocean data assimilation and the Kalman filter. J. Phys. Oceanogr., 17: 1583-1601.

[7] Bennett, A.F., and W.P. Budgell, 1989: The Kalman smoother for a linear quasi-geostrophic model of ocean circulation. Dyn. Atmos. Oceans., 13: 219-268.

[8] Berry, P. and J. Marshall, 1989: Ocean modelling in support of altimetry. Dyn. Atmos. Oceans., 13: 269-300.

[9] Bryan, K., 1969: A numerical method for the study of the world ocean. J. Comput. Phys., 4: 347-376.

[10] Bryan, K., and M.D. Cox, 1967: A numerical investigation of the ocean general circulation. Tellus, 19: 54-80.

[11] Bryan, K., and M.D. Cox, 1972: An approximate equation of state for numerical models of the ocean circulation. J. Phys. Oceanogr., 2: 510-514.

[12] Bryan, K. and L.J. Lewis, 1979: A water mass model of the world ocean. J. Geophys. Res., 84: 2503-2517.

[13] Bryan, K., S. Manabe and R.C. Pacanowski, 1975: A global ocean-atmosphere climate model. Part II. The ocean circulation. J. Phys. Oceanogr., 5: 30-46.

[14] Cox, M.D., 1984: A primitive equation 3-dimensional model of the ocean. GFDL Ocean Group Tech. Rep. No. 1, 143 pp.

[15] Chen, J-H., 1971: Finite difference methods and the leading edge problem. Ph.D. thesis, Princeton University, 102 pp.

[16] Cressman, G.P., 1959: An operational objective analysis system. Mon. Weather Rev., 87: 367-374.

[17] Daley, R., 1981: Normal mode initialization. In: L. Bengtsson, M. Ghil and E. Källén (Eds.), Dynamic Meteorology, Data Assimilation Methods. Springer-Velag, New York, 330 pp.

[18] Derber, J.C., 1985: The variational four-dimensional assimilation of analyses using filtered models as constraints. Ph.D thesis, Univ. of Wisc., Madison.

[19] Derber, J.C. and A. Rosati, 1989: A global oceanic data assimilation system. J. Phys. Oceanogr., 19: 1333-1347.

[20] De Mey, P. and A.R. Robinson, 1987: Assimilation of altimeter eddy fields in a limited-area quasi-geostrophic model. J. Phys. Oceanogr., 17: 2280-2293.

[21] Emery, W.J. and J.S. Dewar, 1982: Mean temperature-salinity, salinity-depth and temperature-depth curves for the North Atlantic and the North Pacific. Prog. Oceanog. Vol. II. pp. 219-305.

[22] Gandin, L.S., 1963: Objective Analysis of Meteorological Fields, Gidrometeorolgich eskoe Izdatel 'sivo, 242 pp.

[23] Ghil, M., M. Halem and R. Atlas, 1978: Time-continuous assimilation of remote-sounding data and its effect on weather forecasting. Mon. Wea. Rev., 107: 140-171.

[24] Ghil, M., 1989: Meteorological data assimilation for oceanographers. Part I: Description and theoretical framework. Dyn. Atmos. Oceans., 13: 171-218.

[25] Haney, R.L., 1971: Surface thermal boundary condition for ocean circulation models. J. Phys. Oceanogr., 1: 241-248.

[26] Holland, W.R., 1973: Baroclinic and topographic influences on the transport in western boundary currents. Geophys. Fluid Dyn., 4: 187-210.

[27] Holland W.R. and P. Malanotte-Rizzoli, 1989: Assimilation of altimeter data into an ocean circulation model: Space versus time resolution studies. J. Phys. Oceanogr., 19: 1507-1534.

[28] Hurlburt, H.E., 1986: Dynamic transfer of simulated altimeter data into subsurface information by a numerical ocean model. J. Geophys. Res., 91: 2372-2400.

[29] Kraus, E.B. and J.S. Turner, 1967: A one dimensional model of the seasonal thermocline. II. The general theory and its consequences. Tellus, 19: 98-109.

[30] Le Dimet, F.X., and O. Talagrand, 1986: Variational algorithms for analysis and assimilation of meteorological observations: Theoretical aspects. Tellus, 38A: 97-110.

[31] Leetma, A., and M. Ji, 1989: Operational hindcasting of the tropical Pacific. Dyn. Atmos. Oceans, 13: 465-490.

[32] Leith, C., 1980: Nonlinear normal mode initialization and quasi-geostrophic theory. J. Atmos. Sci., 37: 958-968.

[33] Lewis, J.M. and J.C. Derber, 1985: The use of the adjoint equations to solve a variational adjustment problem with advective constraints. Tellus, Ser. A, 37: 309-322.

[34] Long, R.B. and W.C. Thacker, 1989(a): Data assimilation into a numerical equatorial ocean model. I. The model and the assimilation algorithm. Dyn. Atmos. Ocean, 13: 379-412.

[35] Long, R.B. and W.C. Thacker, 1989(b): Data assimilation into a numerical equatorial ocean model. II. Assimilation experiments. Dyn. Atmos. Ocean, 13: 413-440.

[36] Malanotte-Rizzoli, P. and W.R. Holland, 1986: Data constraints applied to models of the ocean general circulation. Part I: The steady case. J. Phys. Oceanogr., 16: 1666-1682.

[37] Malanotte-Rizzoli, P. and W.R. Holland, 1988: Data constraints applied to models of the ocean general circulation. Part I: The transient eddy-resolving case. J. Phys. Oceanogr., 18: 1093-1107.

[38] Malanotte-Rizzoli, P., R.E. Young, and D.B. Haidvogel, 1989: Initialization and data assimilation experiments with a primitive equation model. Dyn. Atmos. Oceans, 13: 349-378.

[39] Miller, R.N., 1986: Toward the application of the Kalman filter to regional open ocean modelling. J. Phys. Oceanogr., 16: 72-86.

[40] Miller, R.N., 1989: Direct assimilation of altimetric differences using the Kalman filter. Dyn. Atmos. Oceans, 13: 317-333.

[41] Moore, A.M., 1989: Aspects of geostrophic adjustment during tropical ocean data assimilation. J. Phys. Oceanogr.,19, 435-461.

[42] Moore, A.M., 1990: Linear equatorial wave mode initialization in a model of the tropical Pacific Ocean: An initialization scheme for tropical ocean models. J. Phys. Oceanogr., 20: 423-445.

[43] Moore, A.M. and D.L.T. Anderson, 1989: The assimilation of XBT data into a layer model of the tropical Pacific Ocean. Dyn. Atmos. Oceans, 13: 441-464.

[44] Moore, A.M., N.S. Cooper and D.L.T. Anderson, 1987: Initialization and data assimilation in models of the Indian Ocean. J. Phys. Oceanogr., 17: 1965-1977.

[45] Munk, W.H., 1950: On the wind-driven ocean circulation. J. Meteor., 7: 79-93.

[46] Orlanski, I. and M.D. Cox, 1973: Baroclinic instability in ocean currents. Geophys. Fluid Dyn., 4: 297-332.

[47] Pedlosky, J., 1979: Geophysical Fluid Dynamics. Springer-Verlag. 624 pp.

[48] Robinson, A.R., 1983: Overview and summary of eddy science. In: A.R. Robinson (Ed.), Eddies in Marine Science. Springer-Verlag. pp. 3-15.

[49] Robinson, A.R., M.A. Spall and N. Pinardi, 1988: Gulf Stream simulations and the dynamics of ring and meander processes. J. Phys. Oceanogr., 18: 1811-1853.

[50] Robinson, A.R., M.A. Spall, L.J. Walstad and W.G. Leslie, 1989: Data assimilation and dynamical interpolation in Gulfcast experiments. Dyn. Atmos. Oceans, 13: 301-316.

[51] Sarmiento, J.L. and K. Bryan, 1982: An ocean transport model for the North Atlantic. J. Geophys. Res., 87: 384-408.

[52] Sheinbaum, J. and D.L.T. Anderson, 1990(a): Variational assimilation of XBT data. Part I. J. Phys. Oceanogr., 20: 672-688.

[53] Sheinbaum, J. and D.L.T. Anderson, 1990(b): Variational assimilation of XBT data. Part I: Sensitivity studies and use of smoothing constraints. J. Phys. Oceanogr., 20: 689-704.

[54] Thacker, W.C., and R.B. Long, 1987: Fitting dynamics to data. J. Geophys. Res., 93: 1227-1240.

[55] Tziperman, E., and W.C. Thacker, 1989: An optimal-control/adjoint-equations approach to studying the oceanic general circulation. J. Phys. Oceanogr., 19: 1471-1485.

[56] Verron, J., 1990: Altimeter data assimilation into an ocean general circulation model: sensitivity to orbital parameters. J. Geophys. Res., 95: 11443-11460.

[57] Webb, D.J. and A. Moore, 1986: Assimilation of altimeter data into ocean models. J. Phys. Oceanogr., 16: 1901-1913.

[58] White, W.B., C-K. Tai and W. Holland, 1990(a): Continuous assimilation of simulated Geosat altimetric sea level into an eddy-resolving numerical ocean model. Part 1. Sea level differences. J. Geophys. Res., 95: 3219-3234.

[59] White, W.B., C-K. Tai and W. Holland, 1990(b): Continuous assimilation of simulated Geosat altimetric sea level into an eddy-resolving numerical ocean model. Part 2. Referenced sea-level differences. J. Geophys. Res., 95: 3235-3251.